Karlsruher Institut für Technologie

Optimizing Multi-Color 3D-STED Fluorescence Nanoscopy to Unveil Transcriptional Cluster Nano-Architecture in Embryonic Cells

Zur Erlangung des akademischen Grades eines

DOKTORS DER NATURWISSENSCHAFTEN (Dr. rer. nat.)

von der KIT-Fakultät für Physik des
Karlsruher Instituts für Technologie (KIT)
angenommene

DISSERTATION

von

M. Sc. Amirhossein Barati Sedeh

Tag der mündlichen Prüfung: Juli 25, 2025

Referent: Prof. Dr. Gerd Ulrich Nienhaus

Korreferent: Prof. Dr. Lennart Hilbert

Erklärung:

Ich erkläre hiermit, dass alle in dieser Arbeit vorgestellten wissenschaftlichen und intellektuellen Leistungen eigenständig erbracht wurden. Dies umfasst die Konzeption und Planung von Experimenten in Übereinstimmung mit den Untersuchungszielen, die Durchführung der experimentellen Arbeiten, die Datenerhebung, -verarbeitung und -analyse, die Interpretation der Ergebnisse sowie der Entwurf aller wissenschaftlichen Inhalte.

Während des Schreibprozesses wurden große Sprachmodelle (Grammarly und ChatGPT) ausschließlich zur grammatikalischen und stilistischen Überarbeitung des Entwurfs gemäß den Richtlinien der KIT-Fakultät für Physik verwendet. Diese Tools dienten lediglich dazu, die Klarheit des ursprünglichen Entwurfs des Autors zu verbessern, und trugen nicht zur Erstellung von Material bei. Die endgültige Fassung wurde gründlich überprüft und redigiert, und die volle Verantwortung für ihren Inhalt liegt beim Doktoranden.

Ich bestätige ferner, dass ich alle verwendeten Quellen vollständig und korrekt zitiert habe, dass ich alles zitiert habe, was ich aus den Arbeiten anderer übernommen habe, unabhängig davon, ob es unverändert oder verändert wurde, und dass ich die KIT-Satzung zur Gewährleistung guter wissenschaftlicher Praxis in der Fassung vom 5. Oktober 2021 beachtet habe.

Karlsruhe, 01.08.2025 Amirhossein Barati Sedeh

Table of Contents

Chapter 1: Introduction

Over the past decades, quantitative far-field optical fluorescence microscopy techniques have contributed significantly to the investigation of biomolecular interactions in living systems at the highest possible spatial resolution. As one of these methods, Stimulated Emission Depletion (STED) fluorescence nanoscopy has become a cornerstone in cell research since it provides a unique window to directly observe complicated dynamics that underlie life. Among its benefits over conventional light microscopy, STED's ability to surpass the diffraction limit allows for visualization of nanoscale features crucial for knowledge of cellular architecture. By depleting excited fluorophores within the periphery region of excitation volume, STED nanoscopy performs excitation focal volume engineering to effectively decrease the volume of excitation so that the diffraction barrier can be broken. Also, with the extension to three-dimensional imaging, 3D-STED allows one to get high-resolution volumetric reconstructions of complex biological specimens, further extending its functionality in the study of complicated biological systems.

Despite the increased applications due to superior spatial resolution, there are challenges in improving data quality while conducting multi-color 3D imaging deep inside the cells. For instance, in densely labeled biological samples, the strong fluorescence background signal superimposed on the true signal impairs data quality significantly; hence, strategies to reduce background contribution effectively are required for correct data interpretation. Besides, the nature of optical imaging systems induces wavefront aberrations that could further degrade the achievable imaging resolution. The deterioration caused by aberrations might even be more severe for super-resolution techniques relying on focal volume engineering, like STED, which are extremely sensitive to deviations in focal volume from the ideal distribution of intensity. In such cases, effective deep super-resolution imaging in cells, for instance in zebrafish embryos, requires not only system but also sample aberration minimization, primarily due to refractive index mismatch between the sample and the medium, as well as structural heterogeneities in the specimen itself.

This PhD thesis studies different optimization strategies to improve the performance of multi-color 3D-STED fluorescence microscopy and its application to investigate the nano-architecture at transcriptional clusters in embryonic cells. Chapter 2 describes the theoretical background of this nanoscopy technique, introducing the basics of fluorescence and optical principles. In Chapter 3, the structure and functioning of the custom-built STED microscope setup enhanced in this work are described. Moreover, this chapter discusses one of the existing potent methods to address the fluorescence background while imaging sparsely labeled samples. Chapter 4 examines a novel method developed in this research project for correcting fluorescence background, not only in sparsely labeled specimens but, more importantly, in the highly challenging environment of densely labeled samples. Chapter 5 focuses on the application of background-free 3D multi-color super-resolution microscopy to study morphological characteristics and spatial organization of transcriptional clusters and DNA in zebrafish embryonic cells. Chapter 6 examines the impact of wavefront aberrations in STED microscopy and the implementation of a photon-efficient adaptive optics strategy as a solution. Lastly, Chapter 7 provides a summary of the findings and discusses potential future directions for this work.

Chapter 2: Theoretical Basics

This chapter includes an in-depth explanation of the fundamental concepts essential for understanding the subsequent material of this thesis. Here, the basic principles of the photophysical processes of fluorescent probes, optical imaging concepts and techniques, and the core principles of STED microscopy are discussed.

2.1 Contrast in Optical Microscopy: A Review

An image presents only a fraction of the reality of an object, whatever method of its acquisition is applied. As a result, proper image acquisition and interpretation are essential components of studies and significantly depend on an in-depth understanding of the imaging process. Over the past century, a number of advanced technologies of contrast enhancement in optical microscopy have been developed, which opened new perspectives for biology and chemistry and some industries as well.

One of the classical developments in this field was darkfield microscopy, which was invented by German chemist Richard Zsigmondy in 1903. The method uses the scattering of light by small particles with different refractive indices [1,2]. He applied this microscopy technique to observe colloidal particles; this pioneering work ultimately led to his Nobel Prize in Chemistry in 1925 [3]. Phase contrast microscopy, invented by Dutch physicist Frits Zernike, was another enhancement in this field. This technique uses variations in the polarization of a moving light beam across a sample to visualize the transparent structures without staining [3–5]. Indeed, the invention of differential interference contrast (DIC) by Jerzy Nomarski marked probably one of the most important leaps in optical microscopy. This technique achieves contrast enhancement through the splitting of an incident beam into two perpendicularly polarized parts that interfere after passage through a specimen, thereby providing high contrast and a sense of volume [3,6,7].

Despite the enormous gain in contrast-enhancing methods such as darkfield, phase contrast, and DIC microscopy, the imaging of most biological structures has intrinsic limitations [8]. Most of these methods depend on the interaction of light with the sample and are hence inherently dependent on the optical properties of the biological material. For example, low-

refractive-index materials or transparent objects in general, such as cellular organelles and very thin tissue layers, cannot scatter, phase-shift, or polarize light enough to provide sufficient contrast for observation and subsequent analysis. This purely native optical property reliance of the methods also generally makes them unable to differentiate structures with identical refractive indices or equal phase shifts. Such structures, therefore, require staining techniques. Classical staining, in which dyes are used to enhance absorption contrast, can in principle afford improved visibility but is typically nonspecific. Fluorescence microscopy introduced the concept of fluorochromes. These are molecules for specific labeling of structures of interest that absorb light in a certain wavelength range and then release photons with less energy [3]. In this manner, biological target structures can be labeled with high specificity, and an adequate image reconstruction can be obtained with appreciable precision; this allows for the interpretation of biological phenomena with greater clarity.

Fundamentally, all fluorescent-based imaging techniques depend on the unique characteristics of certain molecules that absorb and emit light in particular spectral ranges. In the next section, the physical bases for fluorescence will be detailed: the introduction of fluorescent molecules and their excitation and emission mechanisms, together with some factors affecting their effectiveness in biological imaging.

2.2 Physical Foundations of Fluorescence

2.2.1 Overview of Fluorescent Molecules

Fluorescent molecules have groupings of atoms whose electrons are delocalized over multiple atoms in their structure. In this system, the molecular orbitals adopt certain charge distributions. These delocalized electrons contribute to the overall negative charge distribution of the molecule, which is stabilized by the positive charges of the atomic nuclei. When a molecule proceeds from its ground state (S_0) to its excited state (S_1) by absorbing energy, electrons promptly move into higher-energy orbitals. However, the heavier atomic nuclei do not immediately readjust. This leads to structural relaxation and molecular vibrations [9]. These vibrations dissipate quickly as heat through interactions with surrounding solvent molecules, leading the system to settle into the lowest vibrational state of the S_1 (see Figure 2.1) [3,10]. The occupation of the S_1 state by electrons has a finite lifetime since the energy level of a molecule in this state is considerably higher compared to the electronic ground state. Noted alternatively, relative to the excitation wavelength, the energy difference can be reemitted as

a red-shifted photon. Briefly, this redshift, which is also known as the Stokes shift, results from the fractional energy conversion into phonons inside the absorbing molecule and the ambient solvent relaxation [11]. Excited state lifetime, τ, is the time spent in the S_1 state prior to fluorescence photon emission, which causes a transition of the molecules back to their ground state, which then affects the electronic configuration around the nuclei [9,12]. The molecule stays in a vibrationally excited state after it moves to the electronic ground state. It then rapidly lowers to the vibrational ground state of S_0 by means of non-radiative mechanisms, releasing the additional vibrational energy to the surroundings. The fluorescence cycle ends when the molecule in the S_0 state returns to its vibrational ground state [3]. It is important to acknowledge that nonradiative decay, which originates from additional impacts with solvent molecules and results in the dissipation of the electronic extra energy, can also cause the transition from S_1 to S_0 [13,14]. Additionally, relaxation via intersystem crossing represents the third decay pathway (see Figure 2.1). This is a process where an excited electron in a molecule undergoes a spin reversal. This action means its spin state changes from a singlet state (being paired) to a triplet state (being parallel) [3,12]. Once the electron's spin is turned around, it goes into the lowest triplet state (T_1). This state has slightly lower energy compared to the S_1 state. The intersystem crossing arrow (k_{isc}) is drawn horizontally since this process is an isoenergetic process. This means that the electron starts from the vibrational ground state of S_1 and ends up in a vibrationally excited state of T_1. Then, it relaxes inside T_1 to its vibrational ground state. To come back down from the triplet state to the electronic ground state, another spin flip is needed. This spin reversal, however, is an unlikely procedure due to the spin configuration mismatch. As a result, the transition is usually a slow event compared to other relaxation processes and occurs over much longer time scales. The return to the ground state from the triplet state may take up to microseconds to even hours to occur, reflecting its much slower nature [9]. The Jablonski diagram usually gives a simplified pictorial description of the different decays and excitations involved, as shown in Figure 2.1 below.

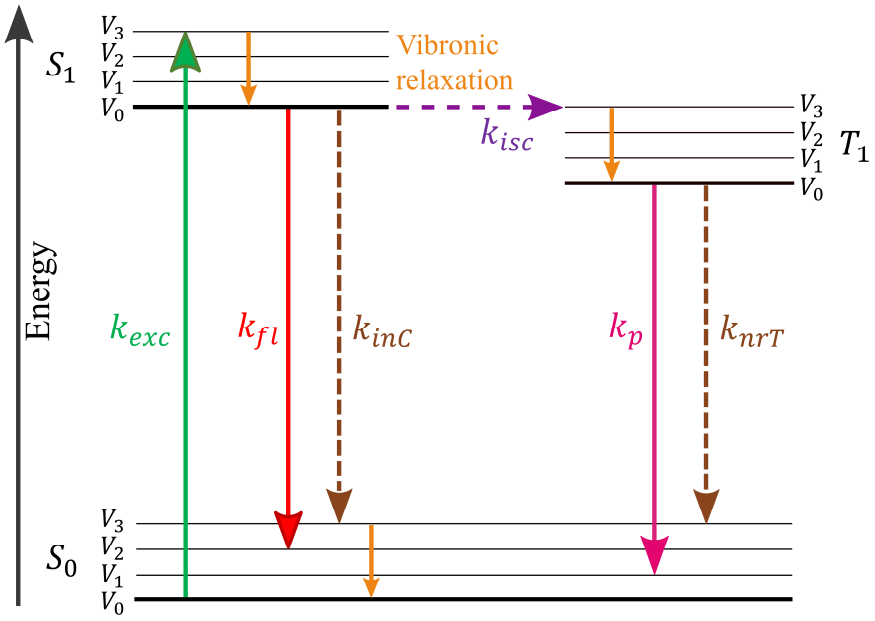

Figure 2.1: A schematic of Jablonski diagram illustrating the electronic and vibrational energy states. Solid arrows indicate radiative transitions, while dashed arrows represent non-radiative processes. The diagram includes ground singlet state (S_o), excited singlet states (S_1), and triplet states (T_1). Key transition rates are shown: rate constant for excitation upon absorption of photons (k_{exc}), fluorescence (k_{fl}) as a radiative decay, intersystem crossing (k_{isc}) as a non-radiative transition, phosphorescence (k_p) which is typically slower than fluorescence, non-radiative triplet decay (k_{nrT}), and internal conversion (k_{inC}) between different vibrational levels of the same electronic state, ultimately leading to a lower electronic state without photon emission.

Moreover, absorption and emission spectra are unique for every fluorophore. The Franck-Condon principle explains that electronic transitions happen faster than vibrations within those states. This makes the spectrum shape depend on how vibrational wavefunctions overlap [15,16]. Because both the ground and excited electronic states have similar vibrational structures and thus comparable transition probabilities, the fluorescence emission spectrum of a fluorophore usually resembles its absorption (or excitation) spectrum [13,17]. The emission spectrum mostly emerges at a longer wavelength than the absorption spectrum due to the Stokes shift, which includes static and dynamic components [18]. The static shift, which is typically larger, originates from energy loss through vibrational relaxation, while the dynamic shift results from environmental changes around the fluorophore during the time between excitation and emission via some sort of relaxation process [3,19]. The dynamic Stokes shift implies the time-dependent process of solvent relaxation that influences the energy levels and relocates the emission wavelength. Two relaxation mechanisms are mostly responsible for this redshift. When a molecule is stimulated, the solvent molecules realign to fit the changed geometry of the S_1 state. Similarly, energy is utilized as the solvent molecules reorganize to conform to the geometry of the S_0 state after the molecule yields fluorescence [11,17].

2.2.2 Dynamics and Equilibrium Characteristics of Fluorescent Emission

Applications in fluorescence imaging, spectroscopy, and energy transfer studies depend on the foundations of dynamics and equilibrium properties of fluorescent emission. More specifically, the dynamics of fluorescent emission are influenced by the temporal behavior of excited state populations and the subsequent relaxation processes that regulate photon emission. The dynamic populations of the S_0, S_1, and T_1 states can be explained in the following manner by using the rates for the transitions as denoted in Figure 2.1 [3]:

$$\frac{d[S_0]}{dt} = -k_{exc}[S_0] + \left(k_{fl} + k_{nr}\right)[S_1] + k_P[T_1] + k_{nrT}[T_1]; k_{exc} = I_{exc}\sigma_a, \tag{2.1}$$

$$\frac{d[S_1]}{dt} = k_{exc}[S_0] - \left(k_{fl} + k_{nr} + k_{isc}\right)[S_1], \tag{2.2}$$

$$\frac{d[T_1]}{dt} = k_{isc}[S_1] - k_P[T_1] - k_{nrT}[T_1]. \tag{2.3}$$

In equations (2.1) to (2.3), the populations of molecules in the ground electronic state, first excited singlet state, and first triplet state are described as $[S_0]$, $[S_1]$, and $[T_1]$ for an ensemble of molecules, respectively. The k_{nr} parameter indicates non-radiative decay rate. The analysis simplifies kinetics by focusing on electronic state transitions, ignoring vibrational states and higher-level excitations. Here, I_{exc} and σ_a are representative of the photon flux of excitation and the fluorophore absorption cross-section at the particular wavelength. By equalizing all derivatives to zeros, these two equations can be exploited to investigate the steady-state dispersion of the ensemble. By integration of the equation (2.2) over time, the dynamic decay of $[S_1]$ after a short excitation pulse is written as follows [3]:

$$[S_1(t)] = [S_1]_0 e^{-(k_{fl}+k_{nr}+k_{isc})t} = [S_1]_0 e^{-t/\tau}, \tag{2.4}$$

where, $[S_1]_0$ is a certain population of S_1after the excitation pulse. It can be interpreted that a mono-exponential function $e^{-t/\tau}$ describes the return to the ground state. τ accounts for the fluorescence lifetime, the average length of time that a molecule remains excited prior to dropping down to the ground state. This parameter can be described as [3]:

$$\tau = \frac{1}{k_{fl} + k_{nr} + k_{isc}}. \tag{2.5}$$

Furthermore, from the photophysical point of view, quantum yield (Φ) is defined as the ratio of the emitted photons to those absorbed by the fluorophore:

$$\Phi = \frac{k_{fl}}{k_{fl} + k_{nr} + k_{isc}}, \tag{2.6}$$

which means this parameter depends on the competition between radiative and non-radiative decay processes [3]. This value shows the efficiency of a given fluorophore ranging between 0 and 1. In applications where signal strength is critical, such as STED microscopy or single-molecule imaging, strong fluorescence signals with a relatively high Φ are preferred.

After examining the dynamics and properties of fluorescence, it is also important to consider photo-bleaching, a process that limits the longevity and effectiveness of fluorophores in practical applications such as microscopy and spectroscopy.

2.2.3 Understanding of Photobleaching

In fluorescence microscopy, photobleaching is the phenomenon whereby fluorescent molecules lose their capacity to emit light due to extended exposure to an excitation source. The photobleaching phenomenon may arise due to photochemical alterations, such as photolysis (cleavage of chemical bonds induced by light) or reactions involving radicals that disrupt the chromophore's conjugated double-bond system [20,21]. This is of particular concern in super-resolution imaging, as the loss of fluorophores directly compromises the ability to resolve fine details with high contrast. The same in STED microscopy, the irreversible photobleaching of fluorophores under light exposure is an important factor limiting the performance of this imaging technique. The extremely high depleting laser power (around 120 mW at the sample plane) in STED aggravates this already major problem by potentially reducing the fluorescence signal strength and limiting the number of imaged samples. Moreover, photobleaching challenges long-term imaging and live-cell experiments by shortening the observation window and impairing the viability of the sample. Understanding of this phenomenon helps with optimizing imaging parameters, such as laser power and choice of fluorophore, that are needed to balance resolution, photostability, and experimental goals.

Photobleaching can be modeled as a two-photon procedure, in which the initial photon stimulates the molecule to the first electronic state, after which it goes through intersystem crossing to reach T_1 [20]. The second absorption occurs at this state, resulting in a transition from $T_1$to T_n, yielding the reactive state T_n for the photobleaching reaction. The kinetics that regulate the steady-state populations of the ground (S_0) and excited (S_1) singlet state, and triplet excited state (T_1) can be expressed as denoted in equations (2.1) to (2.3), using the model of

the fluorophore as a three-level system [20,22]. Using this model, the intensity-dependent population in the triplet state can be determined from [20]:

$$T_1(I) = \frac{k_{isc}\sigma_a I_{exc}}{k_S k_T + \sigma_a I_{exc}(k_T + k_{isc})}, \tag{2.7}$$

where σ_a is the absorption cross section. k_{isc}, k_S and k_T denote the intersystem crossing rate, the rate of all depopulation routes from S_1 to S_0, and from T_1 to S_0, respectively. This equation suggests that the excitation intensity (I_{exc}) has a non-linear proportional effect on the triplet state population $T_1(I)$. This model shows that the triplet state population increases with excitation intensity but saturates at high I_{exc}, due to the balance of competing rate processes. In other words, the population growth in the triplet state is constrained by the rate constants in the denominator and cannot continue indefinitely. In particular, when the excitation light intensity is extremely high, the term $\sigma_a(k_T + k_{isc})$ becomes insignificant in comparison to $k_T k_S$, causing the triplet state population to be on the point of saturation ($\frac{k_{isc}\sigma_a I_{exc}}{k_T k_S}$). Nevertheless, this represents a simplification; the precise operation under extreme conditions depends on the relative magnitudes of the rate constants [20,23]. In other words, this relation highlights the linear transient increase in the triplet population with increasing excitation intensity, up to a point where saturation effects start to dominate. This behavior is regulated by the interplay of intersystem crossing and decay processes.

2.2.4 Fluorescent Dyes as Markers in Sample Preparation

Achieving ideal measurement time, contrast, and resolution with optical microscopy depends on the preparation of the samples. Organic dyes [24–26], quantum dots [27–29], and fluorescent proteins [30,31] are the three main fluorophore sources used extensively in biophysical research nowadays. The smart fluorophore selection has to consider its physicochemical properties, determining performance in biological samples, techniques of applicable labeling, and photophysical properties including excitation/emission ranges, brightness, efficiency, and stability. All fluorophores have their respective strengths and weaknesses; hence, a decision has to be made with respect to the particular requirements of the study. Here, a closer study was conducted on the use of organic dyes, as their excitation/emission ranges and high brightness allowed efficient multi-color imaging to be accomplished.

Organic dyes are considered a fundamental component of biophysical and biochemical research due to their fluorescent properties. A broad variety in all areas of the visible spectrum

and consistently excellent photophysical properties (molecular brightness, photostability) are the advantages of organic dyes. These dyes are small, planar molecules with extended conjugated π-electron systems, enabling broad electron delocalization that results in increased molecular brightness [32,33]. As the extent of this delocalization increases, the energy gap between electronic states decreases, leading to a redshift in their spectral properties that reflects the quantum mechanical nature of these systems [34]. Organic dyes are mostly used in the immunofluorescence-staining approach. In this case, the primary antibody forms a bridge between a specific protein and the secondary antigen, which is supplied with an organic dye, and allows for very specific labeling [35]. A major disadvantage of the technique, however, is that the cells must first be fixed. This is because the antibodies and dyes do not generally pass through the membrane of a cell, and the relatively large size of the antibodies may structurally change the samples being analyzed [36,37].

The fundamentals covered to this point prepare the ground for an improved understanding of the contrast extraction method as a characteristic of an image using modern imaging methods. The next section sheds light on the principles and methodologies that are employed to enhance the ability to accurately observe and analyze biological samples.

2.3 Optical Concepts and Techniques

The aim of cell biology is to gain a more comprehensive understanding of life. Since the naked eye is not capable of observing the cell components and their interactions, there has been a constant need to develop tools that can capture these informative objects. Geometric optics provides the most fundamental configuration for imaging theory. Geometric optics, or ray optics, is the study of the propagation of light in terms of rays. It assumes light travels in straight lines in a homogenous medium, elaborating phenomena such as reflection, refraction, and image formation mostly using Fermat's principle [38] and Snell's law [39]. In this, the light is simplified without considering wave properties and is thus practical for analyzing lenses, mirrors, and optical systems. Using the principle of geometrical optics, Figure 2.2 shows the ray path traveling through a converging lens. Here, the paths of three representative light rays are shown, illustrating how the lens focuses light to produce an inverted image.

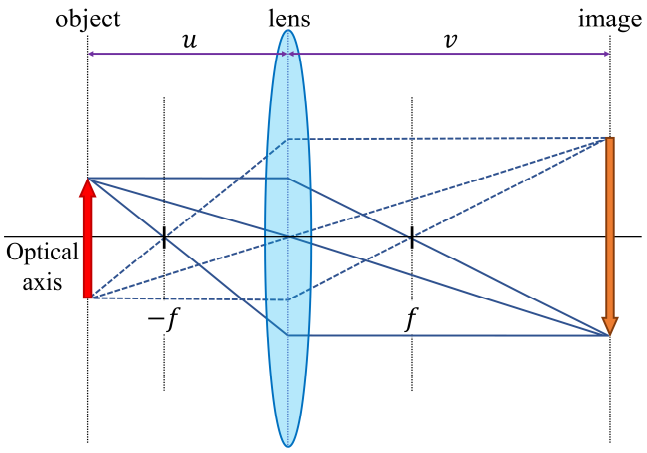

Figure 2.2: Schematic diagram of image formation by a single convex lens. The object is positioned at a distance *u* from the lens, and the resulting image is formed at a distance *v* on the other side. *f* shows the focal points of the lens.

By applying the ray theorems, the lens equation can be obtained from the observation of the ray path [40]:

$$\frac{1}{f} = \frac{1}{u} + \frac{1}{v}. \tag{2.8}$$

The variable f is the focal length of the lens, u is the object distance, and v is the image distance. This equation also describes the interdependence of object and image positions. If a focal length is fixed, a change in object distance u directly affects the image distance v and vice versa. Stated otherwise, a crisp picture will only be obtained in case the lens equation is met.

While geometrical optics gives much insight into the propagation and focusing of light, it is by construction inadequate to address the issue of resolution limits of far-field optical microscopy, since it is a theory that neglects the wave nature of the light. While sufficient for macroscopic imaging, geometrical optics do not account for diffraction, interference, and other wave phenomena that fundamentally determine the resolution of optical systems. Such wave effects impose a physical limit on the minimal resolvable details that Fourier optics can rigorously describe. Since a lens is not a perfect imaging system, the effects of its limiting aperture should be considered. In other words, Fraunhofer diffraction from a circular aperture with a diameter of *D* should be solved [40]. The aperture function in the spatial domain is obtained using:

$$p(x,y) = \begin{cases} 1 & \rho \leqslant D; \quad \frac{\rho}{D} = R \quad ; R \leqslant 1 \\ 0 & \rho > D \qquad\qquad\quad ; R > 1 \end{cases}, \tag{2.9}$$

where, $\rho = \sqrt{x^2 + y^2}$. By taking the Fourier transform of the aperture function at the spatial frequencies $\nu_x = {}^{x}/_{\lambda d}$ and $\nu_y = {}^{y}/_{\lambda d}$ [40],

$$P(\nu_\rho) = \int \rho p(\rho) J_0(2\pi\rho\nu_\rho) d\rho = \int D^2 R p(R) J_0(2\pi D R \nu_\rho) dR = \quad (2.10)$$
$$= D^2 \frac{J_1(2\pi D \nu_\rho)}{D\nu_\rho} .$$

Here, ν_ρ is equal to $\sqrt{\nu_x^2 + \nu_y^2}$. Parameters λ and d show the wavelength of the illumination and the distance between the aperture and observed diffraction pattern, respectively. J_0 and J_1 denote the Bessel functions of order 0 and 1, respectively. Consequently, the Fraunhofer diffraction pattern from a circular aperture of diameter D can be written as [40]:

$$I(x, y) = I_i \left(\frac{\pi D^2}{\lambda d}\right)^2 \frac{J_1^2(2\pi D\rho/\lambda d)}{(\pi D\rho/\lambda d)^2} . \quad (2.11)$$

The radius of the focused spot (ρ_s) can be calculated as $1.22\lambda \frac{f}{D}$ based on the position of the first zeros of the Bessel function of order 1. For a thin lens, the numerical aperture can also be approximated in terms of the lens diameter and the focal length as $NA \approx {}^{D}/_{2f}$. In other words, following the fundamentals of Fourier and wave optics, the diffraction limit, which is also known as the Ernst Abbe criterion, can be approximated by [40,41]:

$$d = \frac{1.22\lambda}{2n\sin\alpha} = \frac{0.61\lambda}{NA} . \quad (2.12)$$

The NA parameter is calculated as the product of the refractive index of the immersion medium (n) and the sine of half the angle (α) at which the lens can still collect light. Such circumstances imply that the smallest size of the focused light is reduced to roughly half the wavelength, even with perfect optics. This diffraction-limited resolution presents a fundamental limit to classic fluorescence microscopy, which cannot resolve structures separated by less than 200–300 nanometers. This limits the ability to distinguish important subcellular details like protein organization and nanoscopic DNA distribution. In other words, diffraction-limited microscopes will not be able to perform accurate qualitative and quantitative studies at the level of subcellular structures; they therefore pose enormous barriers to research in the life sciences.

2.3.1 An Introduction to Confocal Laser Scanning Microscopy (CLSM)

In the 20th century, conventional epifluorescence microscopy gained popularity in biological research for its specificity and strong contrast when using fluorescent markers [42]. Nevertheless, as much as the penetration depth of the excitation light allows, the fluorescent signal is collected, leading to the superimposition of light from different planes, by which the clarity of structures is reduced [43]. Marvin Minsky presented a solution to this problem in 1961 when he developed the confocal microscope [44]. This form of fluorescence microscopy involves focusing the excitation light onto the sample. The focus is then either rasterized over the sample with a scanner or the sample is transferred to the excitation focus. The fluorescent light collected by the objective is then focused again with a lens in a pinhole aperture before reaching the detector. In other words, the excitation focal volume is confocal with the pinhole diaphragm [3]. As a result, a great portion of out-of-focus light gets cut by the diaphragm. As the principle illustrated in Figure 2.3a indicates, this technique makes it possible to generate 3D volumetric images with a significantly higher contrast and resolution compared to a conventional epifluorescence microscope [42]. Actin filaments within HeLa cells, stained with Alexa Fluor 647-conjugated phalloidin, exemplify the sectional imaging capabilities inherent to confocal microscopy in Figure 2.3b. Compared to the wide-field microscope, confocal fluorescence imaging elucidates intricate structural details in a three-dimensional context [3].

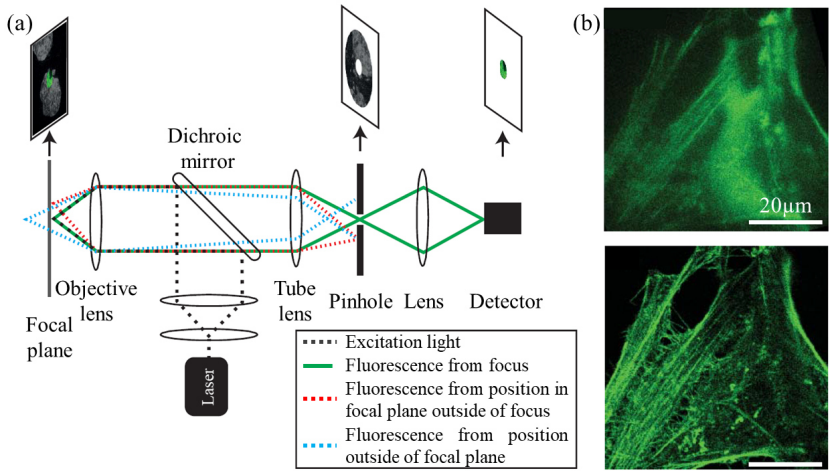

Figure 2.3: Principle and imaging advantage of confocal laser scanning microscopy. (a) Schematic of a confocal laser scanning microscope. Excitation photons (dotted black line) are focused onto a specimen using an objective lens. Fluorescence photons emitted from the focal plane (solid green line) pass through the dichroic mirror, tube lens, pinhole, and lens before reaching the detector. On the other hand, the aperture blocks fluorescence coming from out-of-focus areas (shown by dashed red and blue lines), which improves the image's optical resolution and contrast. **(b)** Qualitative comparison between widefield and confocal images of Hela cell actin filaments. Taken from [3].

2.3.1.1 The Resolution of the Confocal Microscope

Ernst Abbe (1837-1904) laid the foundations of modern optical microscopy that remained unchallenged until the late 20th century [45,46]. He showed that there is a limit to the resolving power of an optical imaging system, defined as its ability to distinguish between two closely adjacent illumination point sources. The clarity of the produced image depends upon the wavelength of light in vacuum condition (λ_0) and the numerical aperture of both the objective (NA_{obj}) and condenser (NA_{cond}) lenses. The following formula represents the relationship of image resolution with NA [47]:

$$d_{min} = \frac{1.22\lambda_0}{NA_{obj} + NA_{\text{cond}}}, \tag{2.13}$$

where d_{min} denotes the smallest lateral distance that the images of two adjacent points can be distinguished. In the simplified case, where both lenses have the same numerical aperture, the microscope resolution can be stated as the equation (2.12).

Building on this basic concept, the point spread function (PSF) provides a more detailed description of an imaging system's resolution. The PSF describes the response of the system to a point source or a point object, delineating the spatial distribution in the image plane of the illumination by an idealized point source. It considers phenomena such as diffraction, aberrations, and other imperfections; hence, it happens to be one of the most important system performance descriptors. In confocal microscopy, the total point spread function (PSF_{tot}) of the microscope results from the convolution of the illumination PSF (PSF_{ill}) and detection PSF (PSF_{det}). The CLSM system as a whole produces two point-like images: one by imaging a point light source onto the object plane, and the other by imaging point detail from the object into the image space on the detector. Mathematically, this relationship can be expressed as:

$$PSF_{\text{tot}}(x, y, z) = PSF_{\text{ill}}(x, y, z) \otimes PSF_{\text{det}}(x, y, z)\,. \tag{2.14}$$

PSF_{ill} indicates the light distribution of the laser spot scanning the object. Its size is mainly a function of the laser wavelength and the numerical aperture of the microscope objective, as well as the effect of diffraction in the pupil of the objective lens, as the main part of the pupil of the illumination section. PSF_{det} is also influenced by all these factors, and in addition, the size of the confocal aperture. The aperture is never truly a point of infinitesimal size, as this causes the intensity of the signal reaching the detector to drop sharply and eventually approach zero. Consequently, in practice, the PSF_{det} is never smaller than the PSF_{ill}. Obviously, the imaging characteristics of a CLSM are determined by the interaction between PSF_{ill} and

PSF_{det}. Although the intensity profile of the PSF resulting from diffraction from the lenses is a Bessel function, the total PSF involves the combined effect of the PSFs of the excitation and the emission beam paths, which essentially results in diminishing the effect of the side rings. It is common to employ the full width at half maximum of the total PSF as a resolution criterion [3]:

$$r_{lateral} = \frac{0.51\lambda_{\mathrm{exc}}}{NA_{obj}}. \tag{2.15}$$

Therefore, compared to conventional fluorescence microscopy, confocal fluorescence even with a large aperture diameter leads to an increase in resolution by a factor of $\lambda_{\mathrm{em}}/\lambda_{\mathrm{exc}}$ which is due to the Stokes shift [48]. Also, the depth resolution of the confocal microscope assuming that the aperture size is equal or greater than 1.0 A.U. is described as:

$$r_{\mathrm{axial}} = \frac{0.88\lambda_{\mathrm{exc}}}{n - \sqrt{n^2 - NA_{obj}^2}}. \tag{2.16}$$

Furthermore, it should be noted that in confocal microscopy, immersion objectives with numerical apertures greater than one are normally utilized. Consequently, the PSF information derived from scalar diffraction theory is only approximative [14,49]. Therefore, precise statements regarding the present PSFs are only possible with the assistance of vector diffraction theory, which Richards and Wolf devised in the 1950s [50]. The diffraction pattern of a laser beam that has undergone focusing through the utilization of a lens possessing a high numerical aperture is simulated in Figure 2.4 using the vectorial calculation [51,52].

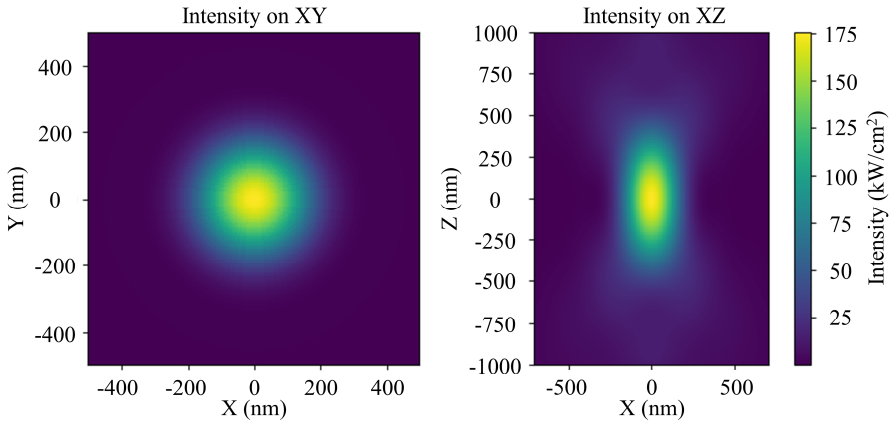

Figure 2.4: Simulation of the excitation PSF according to [51]**.** Parameters used in this simulation were as follows; NA = 1.4, objective aperture radius (mm) = 3.0, incident beam radius (mm) = 3.0, excitation wavelength at vacuum (nm) = 640.0, gamma, laser intensity (mw/cm^2) = 1.0, and immersion medium refractive index = 1.5. The simulation was carried out according to [51].

Following the discussion on the basics of confocal microscopy, an advanced fluorescence microscopy technique that extends the limits of optical resolution beyond the diffraction limit is presented in the next section. Stimulated emission depletion (STED) microscopy is based on the principles of confocal microscopy and enables a significantly higher spatial resolution by selective depletion of fluorescence in the periphery of the focal point. The functional principles and advantages of STED microscopy are discussed in this section.

2.4 Super-Resolution Microscopy: Overview and Fundamentals of STED Microscopy

Several innovative microscopy methods like atomic force microscopy (AFM) and scanning tunneling microscopy (STM) [53,54] came into realization in the first half of the 20th century. This was partly because conventional confocal microscopes and traditional epifluorescence microscopy resolution were still diffraction theory-limited. Although electron microscopy has great resolution, it is not best for cell research as it involves large sample preparation that kills cells, thereby prohibiting the study of live processes [55]. The rigorous preparation can provide artifacts that can cause a structural misunderstanding. Furthermore, its high cost and specialized requirements make it less accessible for routine research [56]. It was in the late part of this century that major discoveries followed the invention of super-resolution light microscopy methods, which break the diffraction limit. These fluorescent nanoscopy methods extended the field of biological and biomedical research and allowed high-resolution 3D volumetric imaging of live biological material.

Super-resolution microscopy techniques can be divided into two categories: stochastic and non-stochastic methods. Stochastic methods, in which photoactivated localization microscopy (PALM) and stochastic optical reconstruction microscopy (STORM) are included, rely on the random switching of fluorescent molecules [57–59]. By capturing many events of single-molecule fluorescence and then fitting the center of these events, it is possible to reconstruct the precise localization of fluorophores in a high-resolution image. On the other hand, non-stochastic techniques rely on PSF manipulation to enhance resolution [60]; among these is stimulated emission depletion microscopy [61].

In 1994, Stefan Hell and Jan Wichmann introduced the concept of STED microscopy [62]. This was a major step toward the objective of visualizing subcellular structures and their dynamic interactions with much improved lateral and axial resolution. The PSF-engineering

technique retained many of the merits of conventional fluorescence microscopy, such as multicolor imaging and relatively deep fields of view, while overcoming the diffraction barrier. In simple words, the working principle of STED relies on the use of the second laser in such a way that it causes controlled depletion of the excited fluorophores. STED microscopy improves spatial resolution by controlling the depletion process so that the diffraction-limited region is minimized to the extent that allows cellular and molecular details to be investigated at higher resolution both laterally and axially [3,63]. This microscopy uses a depletion laser that induces stimulated emission in the target region, forcing the fluorophores to the ground state before they can spontaneously emit photons. These advances have given a better knowledge of numerous disciplines, including biological and medical research, where molecular-level process analysis is vital.

Physically speaking, stimulated emission is a quantum mechanical process that forms the foundation of the functioning of LASER (light amplification by stimulated emission of radiation) [64]. Einstein first described this phenomenon in 1916, where a fluorophore in its excited electronic state interacts with a light photon of a specific wavelength. A fluorophore in an excited electronic state generates a photon with energy matching the difference between its excited and ground states when it interacts with a photon of a suitable wavelength (Figure 2.5). The photon emitted by stimulated emission is, in most cases, easily distinguishable from the broad spectrum of spontaneously emitted fluorescence light since the SE-emitted light is of the same phase and energy as the illuminating light. Such coherence is lacking in the spontaneously emitted fluorescence spanning over a wide range of wavelengths. In practice, this separation of the SE photon is done using a bandpass filter, which selects against the light at the SE wavelength, letting through the more general fluorescence signal [3].

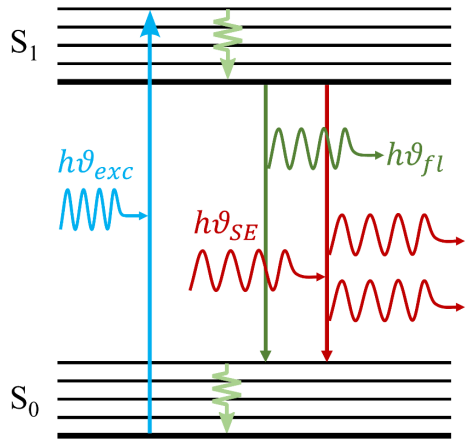

Figure 2.5: Simplified schematic of Jablonski diagram showing the effect of stimulated emission. Here, h is the Planck constant and ϑ_{exc}, ϑ_{SE}, and ϑ_{fl} show excitation, stimulated emission, and fluorescence light frequencies, respectively.

Quantitatively, the probabilities of finding a fluorescent molecule in the ground (P_0) and first electronic (P_1) states is determined using a differential equation as follows:

$$\frac{\mathrm{d}P_1}{\mathrm{d}t} = k_{01}P_0 - k_{10}P_1 = -\frac{\mathrm{d}P_0}{\mathrm{d}t}. \tag{2.17}$$

The transition rates from the ground state to the singlet excited state and vice versa are represented by k_{01} and $k_{10} = k_{fl} + \sigma I_{STED}$, respectively. In the given context, k_{fl} denotes the rate of spontaneous emission (which includes fluorescence), σ represents the cross section for stimulated emission, and I_{STED} signifies the photon flux per unit area of the STED laser. This effect, SE, has to be stronger than natural processes of spontaneous relaxation from an excited state, comprising both fluorescence and nonradiative decay for it to work effectively. Furthermore, the probability of finding a fluorophore that initially resides in S_0, in S_1 at $t \gg (k_{10} + k_{01})^{-1}$, is described as [3]:

$$P_1 = \frac{k_{01}}{k_{10} + k_{01}} = \frac{1}{1 + (k_{10}/k_{01})}. \tag{2.18}$$

Equation (2.18) which demonstrates the dependence of population P_1 on the ratio k_{10}/k_{01}, indicates that by increasing the intensity of the STED laser, it becomes possible to efficiently deplete the population of the excited state (see Figure 2.6b).

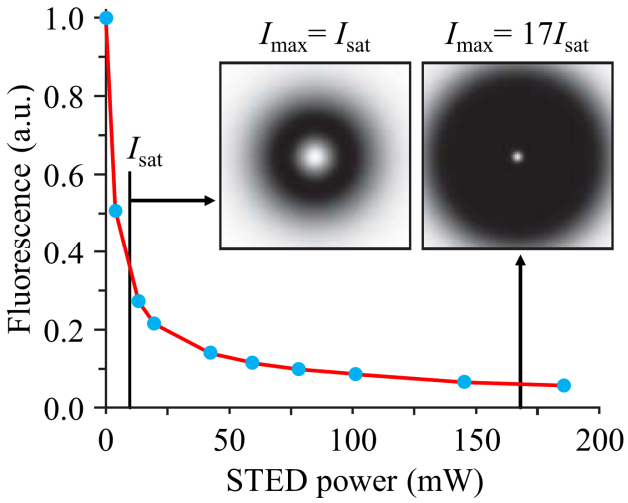

Figure 2.6: Fluorescence depletion of ATTO647N vs. STED laser power. The normalized fluorescence signal of the ATTO647N (organic dye) in aqueous solution which is plotted as a function of the STED laser power (λ_{STED} =770 nm). Taken from [3].

As was already noted, the objective of STED microscopy is to generate subdiffraction-sized effective focal volumes by restricting the region in which molecules can emit fluorescence. This goal is accomplished by using depletion beams which are clearly red-shifted compared to the emission maximum of the fluorophores with a donut and bottle profiles (featuring a local zero centered on the regular excitation focus) in conjunction with Gaussian excitation to decrease the spatial extent of PSF in lateral and axial direction, respectively [65].

A 0-2π vortex phase plate is a special optical element designed for the introduction of a specific phase adjustment across the beam to create a donut beam profile. In effect, the phase shift continuously varying azimuthally from 0 to 2π modifies the phase of the incoming depletion beam in a circular fashion [66,67]. This phase variation changes the phase front of the light wave rather than its amplitude, therefore turning a plane wave into a helical wavefront. The helical characteristic of the wavefront causes destructive interference in the middle part of the beam, ideally producing a zero-intensity region at the center and a donut-shaped intensity profile with a bright ring around a dark core (Figure 2.7) [68]. The size and sharpness of the central dark spot are crucial for the STED process as they determine the effective resolution of the microscopy.

In order to produce a bottle beam profile, a 0-π phase plate also divides the arriving beam into two sections: one passing with an unchanged phase and one with a π (180 degrees) phase shift. At the center of the beam, this phase shift generates destructive interference that results in a black core surrounded in three dimensions by higher-intensity areas (Figure 2.7). Destructive

interference along the optical axis and constructive interference around the beam arise from interference between the 0-phase and π-phase sections [69].

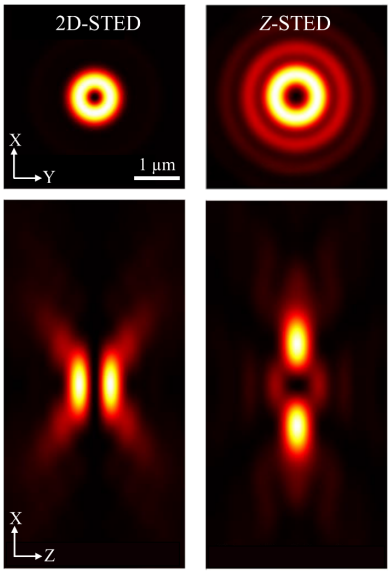

Figure 2.7: 2D and *Z*-STED PSFs. Simulation of the STED PSFs using with the Richards–Wolf vector diffraction theory [171,172]. Taken from [69].

2.4.1 The Resolution of STED Microscopy

To develop a quantitative understanding of the depletion mechanism, it is necessary to study the time evolution of the population N_1 in the first excited state S_1. The solution of the differential equation accounting for the population of the two-level system, with the given initial conditions of $N_1(0) = 1$ and $N_1(t \to \infty) = 0$, is expressed as [45,70]:

$$N_1(t) = N_1(0)\exp\left(-t\left(k_{fl} + k_{\mathrm{STED}}\right)\right). \tag{2.19}$$

Here, k_{STED}, the STED rate is obtained as $k_{\mathrm{STED}} = I_{\mathrm{STED}}\sigma$. The suppression factor of spontaneous emission by STED, defined as the ratio of fluorophores in the excited state to those in the ground state with and without the STED beam [11,14]:

$$\eta(I_{\mathrm{STED}}) = \frac{N_1(I_{\mathrm{STED}})}{N_1(0)} = \frac{e^{-\sigma\tau I_{\mathrm{STED}} + k_{fl}}}{e^{k_{fl}}} = e^{-\ln(2) I_{\mathrm{STED}}/I_{\mathrm{Sat}}}. \tag{2.20}$$

$I_{\mathrm{Sat}} = \frac{\ln 2}{\tau\sigma}$ refers to the saturation intensity at which exactly 50% of the population of the excited state is quenched to the ground state. It is crucial to consider the shape of the depletion pattern, to make a precise prediction of the resolution achieved by a STED microscope. At the central peak of the excitation focus, the depletion pattern can be represented as a parabolic function along a specific spatial direction, denoted as x. This pattern shows a particular

steepness, characterized by the parameter a. The intensity of the depletion PSF at any position x is given by $I_{\mathrm{STED}}(x) \approx 4I_{\mathrm{STED,max}}a^2x^2$ [70]. Here, $I_{\mathrm{STED,max}}$ signifies the maximum intensity within the focal distribution of the depletion beam. Following exposure to the STED beam, the resulting PSF in the x-direction is the confocal PSF ($\mathrm{PSF_{Conf}}$) weighted by the location-dependent suppression factor (η) [70]:

$$\begin{aligned}\mathrm{PSF_{STED}}\,(x) &= \eta(x)\,\mathrm{PSF_{Conf}}(x) = e^{-\frac{4\ln(2)a^2 I_{\mathrm{STED}}\,x^2}{I_{\mathrm{Sat}}}}\, e^{\frac{-4\ln(2)x^2}{d_c^2}} \\ &= e^{-4\ln(2)\left(d_c^{-2}+a^2 I_{\mathrm{STED}}/I_{\mathrm{Sat}}\right)x^2}.\end{aligned} \tag{2.21}$$

It is evident from Equation (2.21) that the resolution constraint of the STED microscope is no longer imposed by diffraction, but rather by the STED laser's intensity. Moreover, the effectiveness of the STED laser's limitation of the PSF is determined by the parameter a, which represents the precise shape of the intensity distribution of the STED laser. Notably, the de-excitation of the STED microscope results in an effective PSF that is, in fair approximation, a Gaussian distribution with the half-width d_c, if the PSF of excitation is described as such [3,63]:

$$d_{STED} = \frac{d_c}{\sqrt{1 + d_c^2 a^2 \frac{I_{STED}}{I_{\mathrm{Sat}}}}}. \tag{2.22}$$

2.5 Challenges in Three-Dimensional STED Imaging

Although STED microscopy has revolutionized optical imaging, the most significant technical challenges it faces are background noise and optical aberrations [71,72]. Realizing the full potential of STED in many applications, especially in the realm of biological imaging of thick and dense samples, requires an understanding of and the ability to overcome these limitations. This part explores the difficulties, their causes, and strategies for prevention.

2.5.1 Background Signal in STED Microscopy

Background in STED microscopy compromises the super-resolution capabilities of the technique. In STED microscopy, incomplete depletion of the excitation volume and re-excitation of fluorophores by the depletion beam are the main sources of background signals. A weak-intensity STED beam or deformation in the wavefronts of depletion beams due to aberrations may cause incomplete depletion of peripheral regions of the excitation volume. Re-excitation of fluorophores by the depletion beam could also contribute to the background signal level, especially when the depletion beam power is enormously high and the depletion

wavelength is set very closely to the maximum of the excitation spectrum. Among the various solutions, stimulated emission double depletion (STEDD) microscopy played a great role because of its reliability and straightforward estimation of the low-frequency background, which is subtracted from the signal plus background image. This method, discussed in detail in the third and fourth chapters, proved to be efficient in the selective elimination of the low-frequency background in STED nanoscopy, regardless of its source [65,71,73]. By means of a comparison between confocal, STED, and STEDD imaging modalities, Figure 2.8 shows the importance of background correction in STED microscopy. Even though the resolution of the STED image (panel (b)) is significantly higher than the resolution of the confocal image (panel (a)), STED imaging exhibits a rather intense background signal, which can give rise to a misleading interpretation of fine structure details. This is resolved in panel (c) by use of the STEDD method, which measures and removes the background contribution, therefore exposing the microtubule structures with enhanced clarity. Moreover, panel (d) measures this enhancement by presenting a narrower width of the intensity profile for STEDD as compared to STED and confocal microscopy, particularly at profile wings.

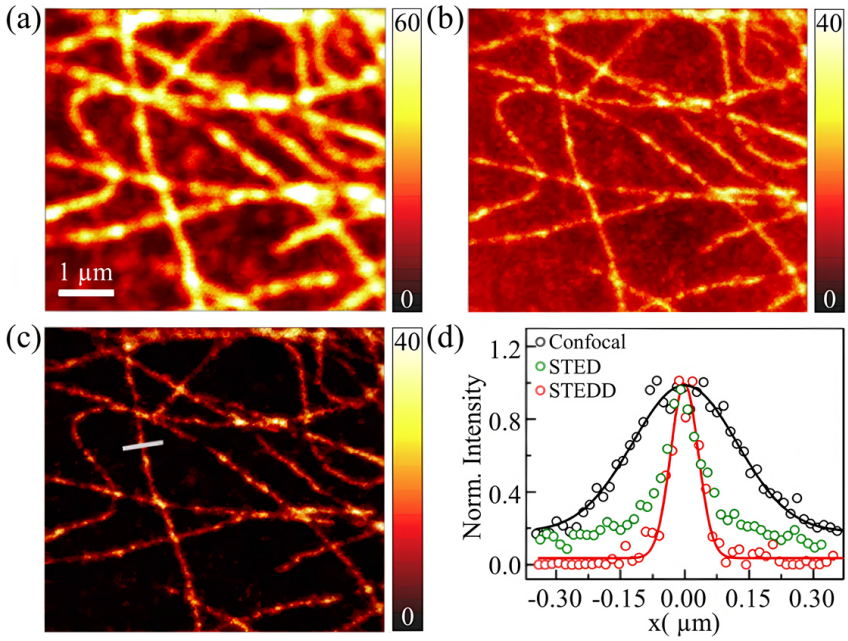

Figure 2.8: Microtubules imaging in a COS-7 cell using (a) confocal, (b) STED, and (c) STEDD modalities. cells were labeled with Atto 647N via immunofluorescence staining. Intensity cross-sections of a microtubule were averaged over three nearby pixels at the location marked by the white line in panel (c). Taken from [65].

Results of previous studies highlighted the importance of background correction techniques, such as STEDD, in STED microscopy to achieve high-contrast imaging [14,65,73,74]. The implementation of this approach is further discussed in the methods chapter. Although the

application of STEDD was investigated in different thin samples in previous studies, the evaluation of the differential STED approach in thick, densely labeled samples was missing. Chapter four of this thesis addresses this gap by presenting a refined version of the STEDD method, which enables precise background subtraction both in thin and thick samples with crowded fluorescent labeling [71].

2.5.2 Aberrations in 3D STED Microscopy

The resolution of the STED imaging approach is theoretically limitless and can be precisely calibrated by adjusting the intensity of the depletion beam. Nevertheless, the resolving power is significantly influenced by the quality of the intensity minimum of the depletion beam in practice [72]. The 2D- and *z*-STED beam profiles can be deteriorated substantially in the presence of system- and sample-induced aberrations [75]. In fact, the highly heterogeneous optical properties of biological tissues can result in severely distorted wavefronts, which makes it a difficult task to conduct STED measurements deeper into specimens (≥ 30 μm). Put simply, when the wavefront of depletion beams (in the shape of a donut and a bottle) in 3D-STED microscopy is distorted due to aberration as the measurement depth increases, the effectiveness of depleting the confocal observation volume is reduced significantly.

Adaptive optics (AO) provides a potent solution to achieve the highest resolution in STED microscopy. Using spatial light modulators (SLMs) and deformable mirrors makes it possible to correct for aberrations dynamically. Figure 2.9 motivates the importance of a photon-efficient AO correction approach in improving the performance of STED microscopy, particularly when imaging the cell nucleus of a zebrafish embryo 96 μm away from the microscope coverslip. The left column shows the confocal images with inherently diffraction-limited resolution. By comparing STED images with and without AO correction, the middle column highlights the challenges of optical aberrations in STED microscopy. Without AO (No AO), strong blurring and loss of signal level are observed, as apparent from the less-defined structures. In contrast, aberration-corrected STED imaging (top right) restores the clarity of structures with sharpness and detail exceeding that of both the confocal and uncorrected STED images. Furthermore, the comparison between AO-corrected and not-corrected background-compensated STED images (namely STEDD images) in the right-hand column emphasizes the importance of aberration correction. As can be seen, by implementing an aberration correction routine, one can easily restore the biological content of the cell nucleus in images. In addition, this figure highlights not only the significance of implementing adaptive optics but also the critical role of background correction in STED imaging. As can be seen, effective background

correction significantly enhances image clarity, which facilitates further qualitative and quantitative analysis.

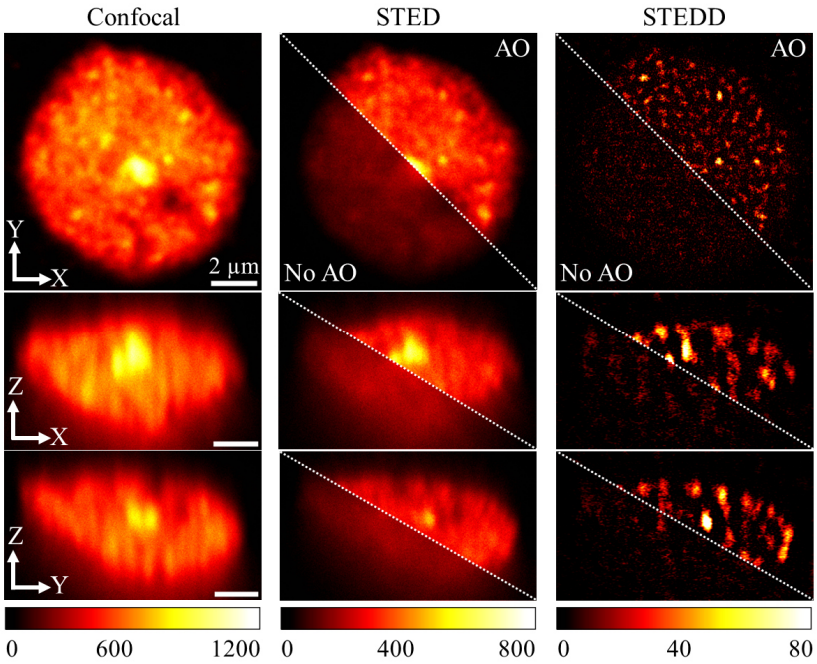

Figure 2.9: Lateral (*XY*) and axial (*XZ*, *YZ*) single-plane sections through the centers of the acquired 3D fluorescence images of RNA polymerase II within a zebrafish embryo cell nucleus positioned 96 µm from the coverslip. Images were obtained using confocal, STED, and STEDD techniques. Acquired images of the nucleus cover a volume of 12.6 × 12.6 × 9.8 µm^3 (250 × 250 pixels, 40 frames). "AO" and "No AO" terms stand for the STED and STEDD images acquired with and without aberration correction. Taken from [72].

This figure demonstrates that optical aberrations during deep cell imaging can significantly limit its potential, even if STED microscopy, by definition, breaks the confocal resolution. Although the sixth chapter of this thesis covers the application of the aberration correction technique, the following part aims to give a basic knowledge of the main aberrations in STED microscopy.

2.5.2.1 Understanding Aberrations in Optical Systems

The imaging system should ideally have a bijective correspondence between points located in the object and image planes [76]. However, in practice, due to the non-existence of an optical system that would fulfill the ideal criteria, this complete correspondence fails and is generally known as aberrations. Aberrations can be generated due to imperfections in optical elements, like lenses and mirrors, i.e., system aberrations, or from the inhomogeneities in the medium through which light travels, i.e., sample aberrations. Since Zernike modes ($Z_n^m(\rho, \theta)$) are orthogonal across a unit circle [76], they are preferred over power series expansion in wavefront aberration modeling and description. This feature makes wavefront decomposition

and reconstruction computationally simpler and usually requires less terms to effectively simulate typical optical distortions.

The Zernike polynomials can be described using three distinct components: N_n^mas a normalization factor, $R_n^m(\rho)$ as a radial polynomial, an azimuthal component which varies as the sine or cosine of integer multiples of θ [77]:

$$Z_n^m(\rho,\theta) = \begin{cases} N_n^m R_n^m(\rho)\cos m\theta, & m \geq 0 \\ -N_n^m R_n^m(\rho)\sin m\theta, & m < 0 \end{cases}, \tag{2.23}$$

where,

$$R_n^m(\rho) = \sum_{s=0}^{(n-|m|)/2} \frac{(-1)^s (n-s)!}{s!\left[\frac{n+|m|}{2}-s\right]!\left[\frac{n-|m|}{2}-s\right]!}\rho^{n-2s}. \tag{2.24}$$

It should be noted that n which is called as the radial order is a non-negative integer to describe the degree of the radial polynomial $R_n^m(\rho)$. The azimuthal frequency which describes the number of lobes that appear as the unit circle is circumnavigated and denoted with m, ranges between $m = -n, -n+2 \ldots n-2, n,$ for a given value of index n. By the help of aforementioned definition of the Zernike polynomial, primary aberrations which highly degrade the resolving power of a STED microscope is summarized in Table 2-1.

Table 2-1: Description of primary aberrations in STED microscopy using orthonormal Zernike polynomials [77].

Aberration type	Zernike polynomials	n	m
Tip	$Z_1^{-1}(\rho,\theta) = 2\rho\sin(\theta)$	1	-1
Tilt	$Z_1^1(\rho,\theta) = 2\rho\cos(\theta)$	1	1
Astigmatism	$Z_2^{-2}(\rho,\theta) = \sqrt{6}\,\rho^2\sin(2\theta)$	2	-2
Astigmatism	$Z_2^2(\rho,\theta) = \sqrt{6}\,\rho^2\cos(2\theta)$	2	2
Coma	$Z_3^{-1}(\rho,\theta) = \sqrt{8}\,(3\rho^3 - 2\rho)\sin(\theta)$	3	-1
Coma	$Z_3^1(\rho,\theta) = \sqrt{8}\,(3\rho^3 - 2\rho)\cos(\theta)$	3	1
Defocus	$Z_2^0(\rho,\theta) = \sqrt{3}\,(2\rho^2 - 1)$	2	0
Spherical	$Z_4^0(\rho,\theta) = \sqrt{5}\,(6\rho^4 - 6\rho^2 + 1)$	4	0

By using the mathematical definition of Zernike polynomials, wavefront aberrations, $\Psi(\rho,\theta)$, can be represented as a series of Zernike modes, $Z_n^m(\rho,\theta)$, on a unit circle with radial coordinate (ρ) and azimuthal coordinate (θ), having coefficients (C_n^m) [72]:

$$\Psi(\rho,\theta) = \sum_{n,m} C_n^m Z_n^m(\rho,\theta)\,. \tag{2.25}$$

Among them, the main optical aberrations that a 3D-STED depletion pattern suffers from are astigmatism, coma, and spherical aberrations [72,78]. Astigmatism aberration occurs mainly in an optical system that has different focal lengths in different meridians [3]. This non-circular focal spot can be generated because of misalignment or imperfections in optical components. Astigmatism mainly deteriorates the symmetry of the shape and intensity distribution of the donut profile, which results in an asymmetric resolution in 2D coordinates [72,75]. Furthermore, comet-shaped aberrated images are generated by the convergence of off-axis rays at various locations along the optical axis, which is known as coma aberration [3]. This aberration thus changes the intensity distribution of the donut beam, shifting it to one-half, again resulting in asymmetric resolution mainly in two dimensions [75,78]. Spherical aberration is also the result of the different breakage of light beams that run through the periphery rather than the center of a lens [3]. In 3D-STED microscopy, the donut and, in particular, the bottle beam pattern at various axial positions can be severely affected [75]. This deviation reduces the effective resolution of the microscope and can distort the reconstructed 3D image.

Chapter 3: Materials and Methods

3.1 System Setup and Instrumentation

This chapter comprehensively explains the structure and functions of the home-built 3D, 3-color STED microscope. Next, the production of appropriate intensity distributions for depletion beams is examined using phase masks generated by spatial light modulators. Following that, the lateral and axial resolution of the STED microscope was evaluated by calibration tests. This chapter also delves further into the developments in STED microscopy, which significantly reduces the background fluorescence signal. Likewise, this section explains the sample preparation methods employed.

3.1.1 Description of the STED Microscope Setup

Figure 3.1 provides an overview of the entire setup, including the excitation, depletion, and detection paths. Dr. Per Niklas Hedde [11] and Dr. Benedikt Josef Prunsche's [14] works served as the foundation for the original design of the fluorescence microscope, which underwent continuous development during this PhD thesis [71,72]. In this figure, only depletion paths are marked with color to maintain an acceptable level of complexity and understandability. The entire setup was built on an optical table with pneumatic leveling. The room temperature was kept constant by an air conditioning system, which decreased the overtime misalignment of the optics. As marked in the image with red, green, and blue dashed lines, three independent depletion beams (z-STED, 2DSTED, and Gaussian STED) were derived from a pulsed Ti:Sa laser (Mai Tai HP, Newport Spectra-Physics, Darmstadt, Germany) operating at 779 nm with either a 40 or 80 MHz repetition rate. It is worthwhile noting that the 100-fs pulses emitted by the Ti:Sa laser were elongated to 300 ps by passing through a 60-cm SF6 glass rod, and then further propagated by 100 m of polarization-maintaining single-mode fiber (PMJ-A3HPC, OZ Optics, Ottawa, Canada). In addition to efficiently suppressing spontaneous emission of the fluorophores, stretching ensured complete coverage of the excitation pulse and minimized excitation and photodamage through multi-photon processes [73]. Two liquid crystal phase-only spatial light modulators (SLM, LETO-3-VIS-009, HOLOEYE Photonics AG, Berlin,

Germany) were used to modulate the wavefront of donut and cylinder PSFs for lateral and axial depletion. As shown in the donut path, the reflected beam from the SLM passed through a vortex phase plate (VPP-1c, RPC Photonics, Rochester, NY) to provide a high-precision donut-shaped PSF at the focal plane. In other words, while cylinder SLM imposed both the cylindrical phase mask of the bottle beam and the phase modulation for aberration correction, SLM in the donut path was used only for the aberration correction task [72]. A small portion of the Ti:Sa laser power was kept unmodulated with the Gaussian profile for background estimation purposes, which is depicted by the blue dashed line in the image. Delayed by a STEDD-delay line for 4.5 ns from the 2D-STED and z-STED beams, the Gaussian STED beam depleted super-resolved images to produce a low-frequency background image in the STEDD technique and required just 10% of the power of the donut STED beam [65,71]. The Ti:Sa beam was split and rejoined by pairs of polarizing beam splitters (PBS) and nonpolarizing beam splitters (BS) and redirected to the galvanometric scanner (Yanus V, Till Photonics, Gräfelfing, Germany) and then towards the body microscope [71,72]. In the home-built microscope, a piezo stage (Nano-F100, Mad City Laboratories, Madison, WI) and galvanometric scanners facilitated the accurate axial and lateral placement of the observation volume inside the specimen. The home-built STED microscope could be utilized in either confocal or STED modes. Samples were imaged with a high-NA objective lens, HC PL Apo 100×/1.40 oil CS2 (Leica, Wetzlar, Germany), integrated into the system, which was constructed around a Leica DMi8 inverted body microscope.

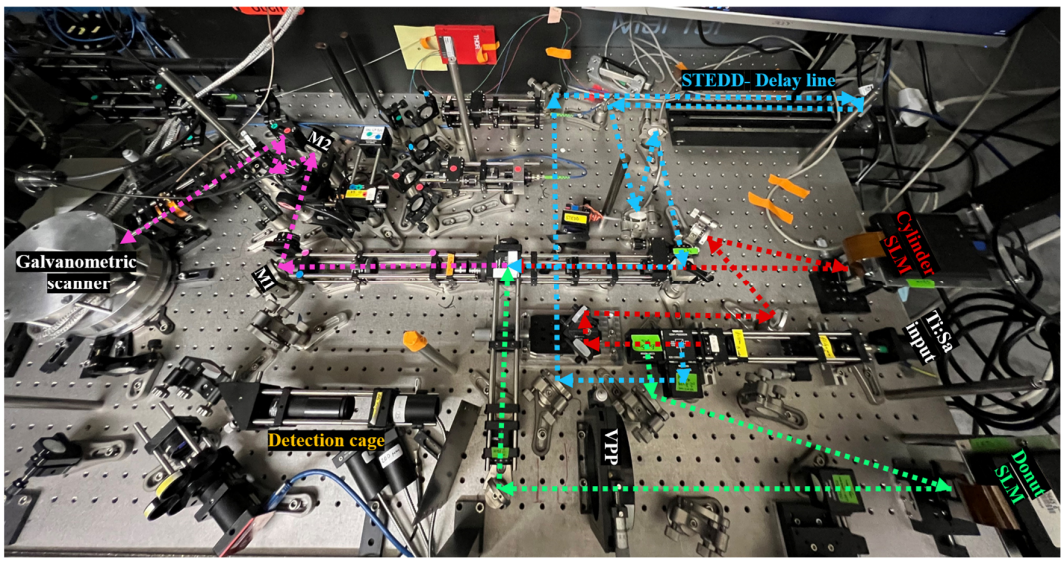

Figure 3.1: An overview of the home-built multi-color 3D STED microscopy setup. To keep the image simple and informative at the same time, only depletion beam paths, including donut, cylinder, and STEDD beams, are shown using green, red, and blue dashed lines, respectively. A PBS combines these three beams and directs them towards the galvanometer scanner. Here, the magenta-dash line displays the shared depletion beam path.

Figure 3.2 shows a schematic diagram of the microscope with all its components marked for excitation, depletion, and detection paths. As can be seen below, all excitation lasers, 640 nm, 560 nm, and 470 nm beams generated from picosecond-pulsed lasers (LDH-P-C-640B, LDH-D-TA-560B, and LDH-P-C-470B, respectively; all PicoQuant, Berlin, Germany) were directed towards a galvanometric scanner and body microscope using a quad-band dichroic mirror (ZT405/488/561/640rpc-3 mm, Chroma, Bellows Falls, VT). The sync signal of the Ti:Sa laser triggered the excitation lasers, and a home-built delay box temporally aligned them with respect to the Ti:Sa laser. Note that the dichroic mirror and the following mirror shared the same excitation path, which allowed them to compensate for alignment if all the excitation beams had the same type of misalignment with the body microscope's central entrance and objective nosepiece. Appendix B.1 describes in more detail the spatial alignment of the home-built microscope. The Ti:Sa laser beam was also divided into two portions with vertical and horizontal polarizations. The Gaussian depletion beam was created by the low-power vertical fraction. A 50:50 beam splitter separated the horizontal fraction into two beam paths of equal power. The horizontally polarized beams were coupled into the donut and bottle beam paths, respectively. To reduce unmodulated reflections, the SLMs were calibrated to reflect the first diffraction order of a blazed grating overlaid on a desired phase pattern. Pinholes were used afterward for blocking other diffraction orders. Then, all depletion beams were combined by a PBS and sent toward the common excitation path through a pair of mirrors. These two common mirrors were used in case all depletion beams shared the same misalignment and needed the same compensation to have a perfect overlap with the excitation beams. A short-pass dichroic mirror (Z730sprdc, Chroma) merged the STED and excitation beams into a single path. Note that generating the most efficient donut profile with a central intensity close to zero requires matching the helicity of the vortex phase mask and the focused light into the focal plane [14,79]. To achieve this, the orientation of the donut beam was changed to right-handed circular polarization using a combination of half- and quarter-wave plates. Furthermore, to achieve high-resolution imaging using STED microscopy with effective fluorescence depletion, temporal alignment between excitation and depletion beams was required. A home-built sync/delay electronic device was employed to establish a 200-ps delay between the excitation and the 2D-STED and z-STED beams to ensure that the depletion beams effectively suppress fluorescence emission at the periphery region of the focal volume, thus enhancing resolution beyond the diffraction limit [72].

In this optical setup, the fluorescence or scattered signal is returned along the same optical path (purple line in Figure 3.2). It passed through the quad-band mirror and was guided towards a multi-mode fiber having a core diameter of 50 µm. The system comprised two avalanche photodiodes (APDs, COUNT-T100, Laser Components, Berlin) for imaging with multiple colors of fluorescence, as shown in the detection path. Avalanche photodiodes are devices that convert light into an electrical signal and amplify it by a process called avalanche multiplication, whereby one photon can produce many pairs of electrons and holes. Fluorescence imaging: A short-pass filter (FF01/715/SP-25; Semrock, Rochester, NY) was used to block the scattered signal coming from depletion beams. A band-pass filter in front of each APD picks up only the light within a selected range, which allows one to take pictures in multiple colors without mixing signals from different dyes. A time-correlated single photon counting (TCSPC) device (MultiHarp 150P, PicoQuant) recorded the fluorescence light detected by the APDs. Custom software written in MATLAB (MathWorks, Natick, MA) was employed for hardware control throughout image acquisition and data analysis.

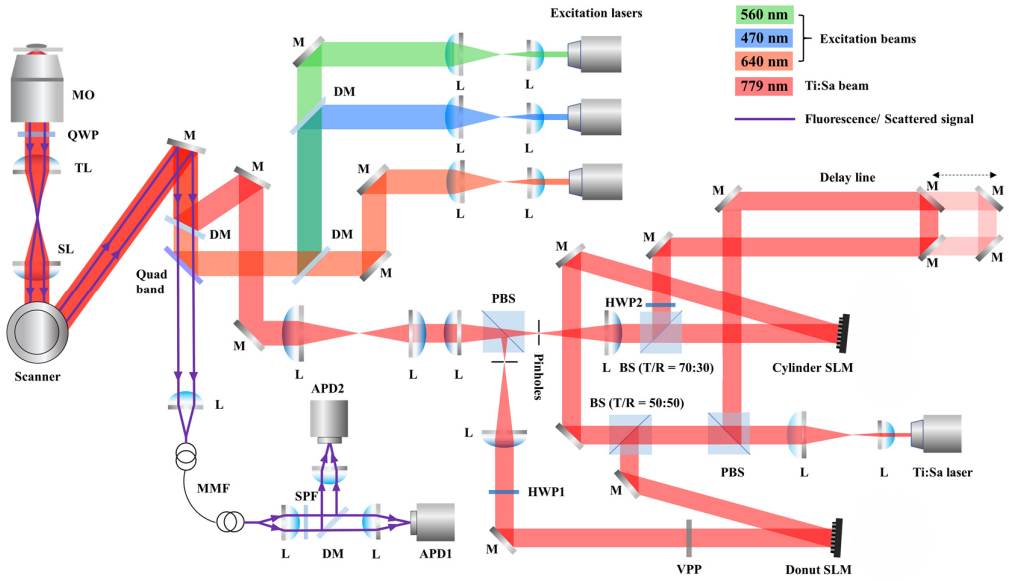

Figure 3.2: Schematic diagram of the STEDD microscope. BS: beam splitter; PBS: polarizing beam splitter; DM: dichroic mirror; M: mirror; L: Lens; SL: scanning lens; TL: tube lens; SLM: spatial light modulator; VPP: vortex phase plate; QWP: quarter-wave plate; HWP: half-wave plate; MMF: multi-mode fiber; APD: avalanche photodiode; SPF: short-pass filter.

3.1.1.1 Implementation of 3-Color Fluorescence STED Microscopy

Multicolor fluorescence imaging is essential for visualizing and quantifying different cellular components within one image, thus helping the researcher to pursue studies on complicated interactions within biological systems. In this way, it raises the degree of accuracy concerning identifying and differentiating various biomolecules within one sample. Figure 3.3 illustrates

the implementation of simultaneous 3-channel imaging in the custom-built STED microscope. For an effective multi-color imaging, Ti:Sa laser was run on 80 MHz repetition rate (two pulses within 25 ns), and excitation lasers were operated on 40 MHz rate (one pulse within 25 ns). Based on this detection schematic in Figure 3.3a, emission fluorescence photons resulting from the 640, 560, and 470 nm excitation lasers were first passed through a 715 nm short-pass filter to exclude the scattering signal from depletion beams. Afterward, a long-pass dichroic mirror was used to direct the emitted photons from the 640 nm excitation toward the first detector and to reflect the emission from two other lasers toward the second detector. Note that to exclude fluorescence signal crosstalk between these two APDs, a band-pass filter was placed in front of each. This means that the same APD received fluorescence emission signals from both the 560 and 470 nm lasers. To realize multi-color imaging using two APDs without cross-talk between different channels, not only spectral but also temporal separation between fluorescence signals from different fluorophores was needed. Figure 3.3a describes the spectral separation, while Figure 3.3b illustrates the temporal distinction between the fluorescence signal from 560 and 470 nm excitation laser beams. The 560 nm and 470 nm laser beams were sequentially triggered by a temporal difference of 12.5 ns using a delay box. In this manner, the specific fluorophores for these two channels were not triggered at the same time. Instead, the fluorescence signals from these two channels were separated temporally and collected sequentially, one after the other.

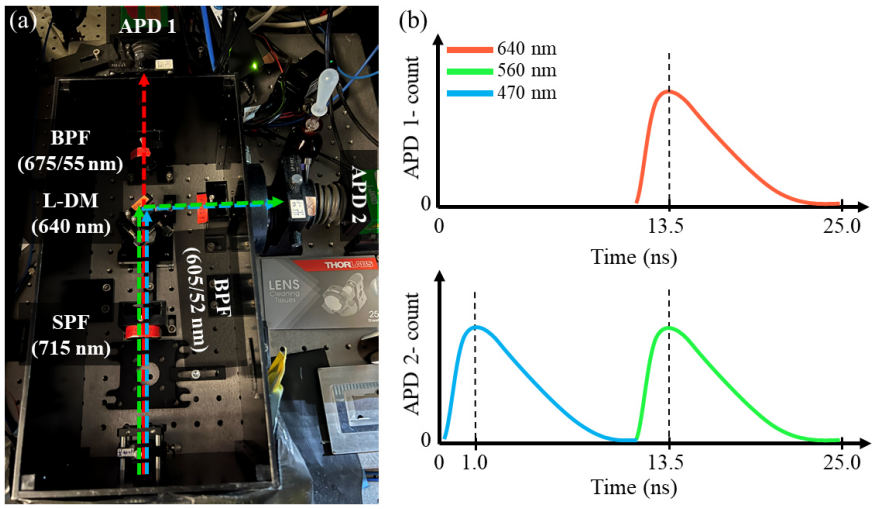

Figure 3.3: Principle of 3-color confocal/STEDD microscopy using two APDs. (a) Layout of the microscope detection path for 3-color measurements. L-DM, BPF, and SPF stand for long-pass dichroic mirror, band-pass, and short-pass filters. **(b)** Schematic of photon counts on APD 1 and 2, which collect fluorescence emissions resulting from 640 nm, 560 nm, and 473 nm excitation lasers, respectively.

3.1.2 Laser Wavefront Modulation Through SLMs

In beam phase modulation, SLMs are more flexible than conventional phase plates. Apart from producing suitable intensity distributions for donut and cylinder PSFs, as has already been discussed, the integration of SLMs with the STED microscopy setup greatly facilitates the achievement of efficient STED microscopy in thick samples by means of aberration correction. In this section, the working principle of SLM and the required considerations during the calibration procedure are explained.

To generate the desired phase, spatial light modulators use an 8-bit image to modulate the phase and intensity of light beams. They basically consist of an array of individually controllable elements that manipulate the properties of incident light. Each pixel in this array is independently capable of changing the phase, amplitude, or polarization state of the light that passes through or reflects from the element. Through synchronized modulation in the array, SLMs apply complex spatial patterns to the light wavefront [80,81]. Based on their modulation method, SLMs are categorized into three types: liquid crystal SLMs (LCSLMs), micro-electro-mechanical systems (MEMS)-based SLMs, and acousto-optic modulators (AOMs). In this work, the microscope was combined with reflective LCSLMs for their capabilities of high-resolution phase modulation. LCSLMs rely on an applied electric field to change the optical properties of liquid crystal materials. As shown in Figure 3.4, liquid crystals are anisotropic molecules that undergo reorientation in response to an electric field. This reorientation modulates the refractive index of the liquid crystal layer, therefore influencing the phase of the reflected light as well. In other words, the degree of the phase change depends on the supplied voltage to every pixel. Transparent electrodes etched on the SLM's substrate control the phase modulation at every pixel, thereby regulating the alignment of liquid crystal molecules. a diagram of an LCS-SLM structure. The LC layer is sandwiched between two alignment layers, one of which is bonded to an optically flat glass substrate with a transparent electrode, while the other one is bonded to a silicon backplane with a metal electrode array [82]. This, combined with a CMOS chip and aluminum pixel electrodes, enables voltage-driven reorientation of the LC molecules that modulate the phase of light reflected by the device. The size of the pixel directly affects resolution and diffraction efficiency, while small pixels increase crosstalk between adjacent pixels. It should be noted that a portion of the light remains always unmodulated, even through the anti-reflection layer on the SLM, caused by reflection from the glass substrate. Furthermore, imperfect polarization separation by the PBS and polarization direction exchange by the front layers in front of the LC result in a case where a small

proportion of the light passes through the SLM without appropriate phase modulation. To counter this, the SLMs were aligned to reflect the first diffraction order of a blazed grating overlaid on a desired phase pattern to minimize reflections [72,83]. Two apertures in the middle Fourier planes of the telescope system, positioned after the SLMs, selected the +1st order, which carries a high efficiency of 75% after gamma response calibration (85).

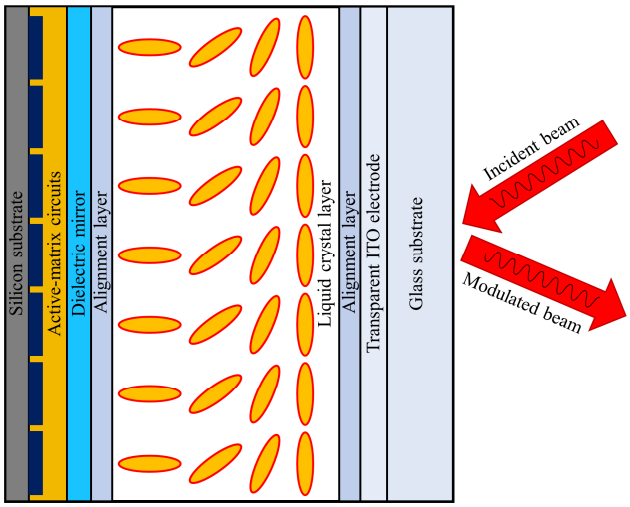

Figure 3.4: Scheme of an LCS-SLM device structure. This includes of a glass substrate with transparent indium tin oxide (ITO) electrode, liquid crystal (LC) layer sandwiched between two alignment layers, a dielectric mirror to maximize reflectivity, and a silicon substrate with active-matrix circuits.

3.1.2.1 Measurement of the SLM Calibration Curve

Accurate phase modulation using SLMs calls for calibration. Each pixel in an SLM modulates the phase of the light that passes or reflects from a given grey-scale value assigned to it. Since these gray values directly relate to phase shifts, the calibration procedure ensures that the phase modulation or signaling adheres to what was intended. Therefore, a separate calibration is required for every wavelength of light, as the phase shift in SLM is attained by a change in the effective refractive index upon passing through it. An interferometric approach was implemented for SLM calibration and recorded images using a camera, as schematically illustrated in Figure 3.5. As it is shown below, half of the SLM is always zero; however, the other half ranges between 0 and 255 in the grayscale range [84,85]. In other words, to employ this calibration approach, 256 distinct grayscale images were generated. Interference patterns were generated as a result of the lens on the camera superimposing the light that descends uniformly on both halves of the SLM.

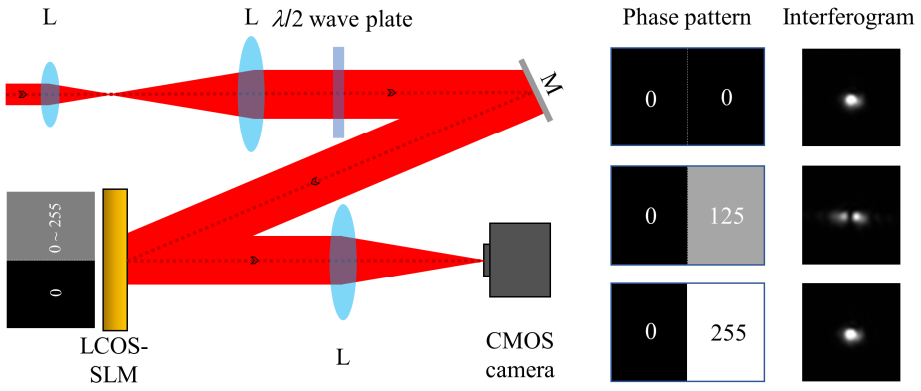

Figure 3.5: A simplified schematic of the experimental setup that was used to characterize the phase modulation of SLMs. The plots on the right illustrate the exemplary interferograms when the variable half of SLM pixels were set to 0, 125, and 255 at the calibration wavelength of 779 nm.

A small region of 16×16 pixels was set around the point of maximum intensity in the first recorded image. This was a site where constructive interference was present for optimum alignment. The intensity curve, determined by averaging the pixel values of each interferogram over this small region, was used to determine the relative phase shift for each gray value (see Figure 3.6a). As can be seen, at a gray value of approximately 125, the most destructive interference occurs, and to achieve a 2π modulation, a gray level of 255 is needed at a wavelength of 779 nm.

In addition, the phase between two beams was calculated for each interferogram based on the measured intensity level using:

$$I = \underbrace{I_1}_{|E_1|^2} + \underbrace{I_2}_{|E_2|^2} + 2E_1E_2\cos(\varphi)\,. \tag{3.1}$$

Here, I_1 and I_2 are the intensity of two beams. E_1, E_2, and φ are the amplitude of the E-field of beam two beams, and the phase difference between these two. It is clear that the maximum (I_{max}) and minimum (I_{min}) intensity happens when φ is equal to 0 and π. When these two measurable variables are incorporated into equation (3.1), the phase expression is obtained as [84,86]:

$$\varphi = \arccos\left(\frac{2I - I_{max} - I_{min}}{I_{max} - I_{min}}\right). \tag{3.2}$$

By considering the case that ideal phase modulation follows a linear regression with regards to the gray value exchange on the SLM [86], a linear fit was applied to the measured data (see Figure 3.6b). Therefore, the mapping relationship of phase response from 0 to 2π with corresponding gray levels can be defined. Using these mapping relationships, the generation of phase patterns, such as donut and 0-π, was then performed for the depletion laser wavelength. More importantly, considering the laser at 779 nm itself, the phase modulation has already reached 2π, which could lead one to assume that, in practical realization, lasers of a longer wavelength are impossible to drive on a full 2π modulation. This is not a correct assumption because SLM allows for redefining the voltage range applied to the LCOS pixels to remap the gray levels. However, this setting needs to be recalibrated each time the range of voltage is changed [84].

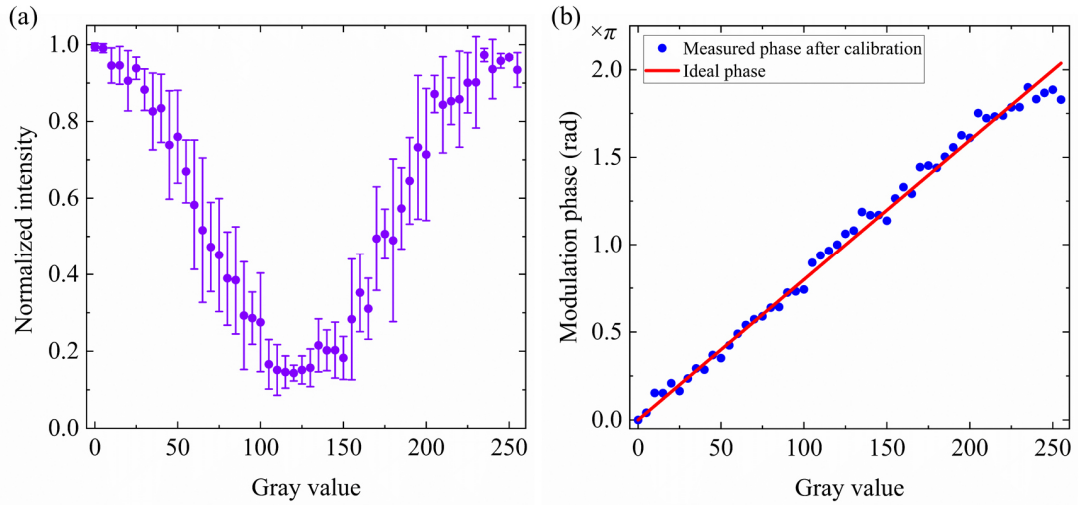

Figure 3.6: LCOS display calibration: intensity and phase modulation. (a) Mean ± standard deviation representation of normalized intensity recorded via a CMOS camera versus a gray level applied to one half of the LCOS display at a wavelength of 779 nm. This experiment was conducted three times to improve the calibration's accuracy. **(b)** A plot of phase modulation versus gray level, along with the linear fit applied to the experimentally measured data after calibration.

3.1.2.2 Formation of Optimal Intensity Distributions for STED Beams Using SLMs

After examining the operating principles and calibration method of SLMs, it is necessary to investigate the process of generating suitable intensity distributions for depletion beams using these devices. Indeed, one of the most critical factors in STED microscopy is the generation of the correct intensity distributions of the depletion beam in the focal plane of the objective lens and thus in the sample being studied. The STED beam's spatial intensity distribution determines the specific spatial axis and degree of resolution enhancement. Key parameters include the steepness and depth of the intensity minimum. Equation (2.22) reveals that the steepness of the

minimum's edges affects most the relation between the achievable resolution and the required depletion beam power since it is the amplitude of the central minimum that essentially defines the quality of the final STED images. Since the peak intensity used with STED is several times higher than the saturation intensity, even a rather low intensity at the central minimum is sufficient to quench the signal considerably, making it impossible to get high-quality STED images with a good signal-to-noise ratio. In this work, wavefront interference modulation is utilized for generating the aimed distributions of beam intensity at focus. This was achieved for 2D-STED by a transparent phase plate, which locally retarded the beam and deformed the wavefront. The second method was to use a spatial light modulator using birefringent liquid crystals to allow modulation of the phase. The main advantage of using SLMs is the unlimited capability of wavefront modulation just by exchanging the phase pattern on the display. In other words, SLMs not only generate donut and cylinder beam profiles for 2D- and *z*-STED, but they can also be used to simultaneously implement wavefront correction for aberration compensation. To this end, as shown in Figure 3.1 and Figure 3.2, a physical vortex phase plate and an SLM were used to generate donut and cylindrical beam profiles, respectively. Figure 3.7 shows an example of donut and cylinder beam PSFs in three orthogonal planes, namely *XY*, *YZ*, and *XZ*, using reflection imaging of immobilized gold beads (80 nm) on a microscope coverslip. As can be observed, the donut beam efficiently depletes in the lateral domain, while the cylinder beam achieves the most effective depletion in the axial direction. Namely, 3D STED microscopy employed these beams in conjunction to achieve effective depletion in both the lateral and axial directions.

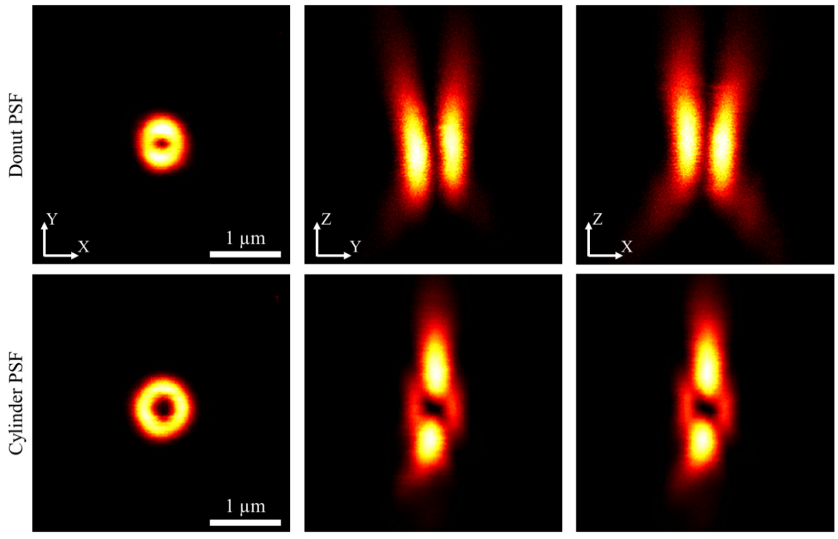

Figure 3.7: PSFs of donut and cylinder beams. An illustrative example of the experimental PSFs of donut and cylinder beams in the *XY*, *YZ*, and *XZ* views, which were respectively used for 2D and *z*-STED measurements.

3.2 Calibration of Lateral and Axial Resolution in the Custom-Built STED Microscope

Further to the discussion on how STED microscopy works and the need to calibrate the SLMs for high-quality depletion beams, resolution calibration tests were performed in both the axial and lateral domains to demonstrate the efficiency of the home-made setup in depleting the periphery regions of the confocal volume and precisely enhancing resolution. This section explains the sample preparation and imaging protocols and procedures used for resolution calibration. Proper calibration enables optimization of the system, thereby validating its performance and increasing the accuracy of high-resolution imaging capability.

3.2.1 Sample Preparation for STED Microscopy Resolution Calibration

The following materials were needed to immobilize fluorescence nanospheres on the microscope coverslip: poly-L-lysine (PLL), double-distilled water (ddH_2O), LoBind microcentrifuge tubes, fluorescent bead solution, glycerol (mounting medium), a microscope coverslip (equivalently an eight-well chamber), pipettes and pipette tips. PLL is a homopolymer with a repeating lysine unit, and as such, the high density of positive charge emanates from the lysine amino groups. PLL anchors the beads to the coverslip or well surface through the creation of a positively charged coating into which the negatively charged beads interact to help them stay fixed in place during imaging.

Sample preparation was started with a dilution of 0.1 mg/ml PLL with 1:10 ddH_2O in a LoBind protein microcentrifuge tube. This step was followed by several times of pipetting the solution up and down to make sure PLL was uniformly mixed inside the solution. After 1 hour of applying 200 µl of the diluted PLL on a microscope coverslip, the unbound PLL was removed carefully by draining the coverslip using fine pipette tips without scratching the functionalized surface and washed consequently three times using ddH_2O, each time for 5 minutes. Sonicated fluorescence beads solution (Ø 40 nm, FluoSpheres, dark red fluorescent (660/680 nm), ThermoFisher Scientific) for 40 minutes was diluted with a $1:10^5$ ratio. 200 µl of the diluted fluorescent beads were applied to the coated surface and incubated for 1 hour at room temperature. Then the excess solution was removed and washed three times with ddH_2O; each washing lasted five minutes. In the end, glycerol was added as the mounting medium, and the coverslip was mounted on a coverslide.

3.2.2 Lateral and Axial Resolution Calibration Curves

The calibration sample, as previously explained, was used to measure the lateral and axial STED microscope resolution. Figure 3.8 presents a comprehensive quantitative and qualitative study of the resolution calibration for 2D and *z*-STED at various depletion powers, using immobilized 40 nm polystyrene beads filled with fluorescent dye (dark red beads) on the coverslip. The excitation was carried out with 7.0 µW at 640 nm, and the depletion wavelength was set at 780 nm. Furthermore, at each donut depletion beam power, four regions of interest with the size of 15×15 µm^2 and a grid size of 650×650 pixels were measured. Also, at each cylinder depletion power, 20 ROIs, each containing at least one bead, with a size of 1.9×3.0 µm^2 and a grid size of 200×200 pixels in the *XZ* plane were measured. The resolution was quantitatively determined by analyzing the fitted line profiles using a Gaussian function. The resolution metric was subsequently determined to be the full width at half maximum (FWHM) of these Gaussian profiles. It should be noted that the size of the DRB (d_{DRB}) was excluded from the measured resolution ($d_{measured}$) using [87]:

$$d_{Corr} = \sqrt{d^2_{measured-}d^2_{DRB}}\,. \tag{3.3}$$

The measured lateral and axial resolutions of STED microscopy, at the highest available beam power for each beam, were 65 nm and 170 nm, respectively, as shown in Figure 3.8. These values are obviously enhanced compared to the diffraction-limited resolving power achieved by conventional microscopy techniques, such as confocal microscopy. Furthermore, qualitative investigations based on the exemplary ROIs in this figure show a significant shrinkage of the confocal PSF extension in both the lateral and axial directions as the depletion beam power increases. This substantial improvement in resolution proves that the custom-built STED microscopy is running ideally and can resolve much finer structural details than diffraction-limited imaging methods. This fine resolution enables it to become an important tool for tasks that need nanoscale accuracy.

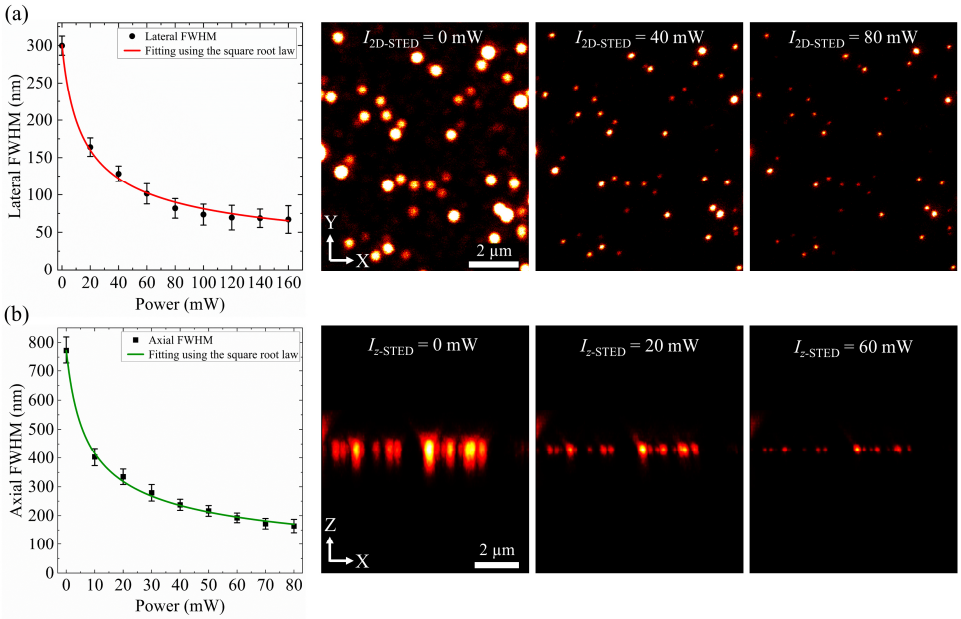

Figure 3.8: Quantitative and qualitative investigation of the lateral and axial resolution of the custom-built STED microscope. (a) The profile of at least 150 spheres per each depletion power was fitted using a normal distribution. The diagram plotted the resulting average half-width and the standard deviation of the mean value. The red curve is a fit to the measured data using equation (2.22) and shows excellent agreement between the measured values and the theory. On the right side, three exemplary DRB images for various donut STED powers are illustrated within the same contrast range. **(b)** Similarly, to calibrate the *z*-STED resolution, the profile of at least 20 spheres in the *XZ* plane per each depletion power was fitted using a normal distribution. The measured values and the theory based on equation (2.22) (solid green line) exhibit significant agreement. Additionally, three representative images of the DRB for varying cylinder STED powers are displayed in the same contrast range on the right side.

3.3 Development of Stimulated Emission Double Depletion (STEDD) Microscopy

Although STED microscopy has revolutionized optical imaging, one of the most significant technical challenges it faces is fluorescence background signal [65,71,73]. During the past few years, one of the most significant developments in STED microscopy is background subtraction, which greatly enhances image contrast by surpassing undesired fluorescence originating from out-of-focus areas, autofluorescence, and re-excitation by the depletion beams, often veiling fine details. Precise background removal offers a better signal-to-noise ratio, therefore offering accuracy in both qualitative and quantitative research of the nanostructures. This section describes a breakthrough in STED microscopy known as STEDD microscopy (stimulated emission double depletion). The first experimental realization of this approach was introduced in 2017 [65,73]. This section provides a description of the importance and physical working principles of this approach.

3.3.1.1 Motivation and Experimental Realization of the STEDD Microscopy

In STED microscopy, background signals primarily arise from two effects: (i) incomplete depletion of fluorescence in the periphery of the excitation PSF due to insufficient STED intensity, and (ii) unintended re-excitation of fluorophores by the depletion beam itself, especially when it overlaps with the excitation spectrum of the fluorophore [65]. The low STED beam intensity, aberrations in the wavefronts of depletion beams, and ineffective spatial or temporal alignment between the excitation and the depletion PSFs may generate out-of-focus light due to the incomplete depletion of peripheral regions of the confocal excitation volume, appearing as a low-frequency image background. This issue, which becomes more evident during three-dimensional imaging of densely labeled structures can be partially mitigated by increasing the overall power of the depletion beam. At the same time, increasing the STED beam power raises the possibility of excessive photobleaching in high-power regions and re-excitation of fluorophores via anti-Stokes Raman and other light-induced processes, which results in low-resolution backgrounds. The re-excitation background can be reduced by decreasing the absorption cross section for the depletion wavelength. This can be accomplished by red-shifting the depletion beam as much as possible from the excitation band of the fluorophore. The method has some limitations, especially for emitters with large excitation and emission bands and small Stokes shifts, for example, core-shell quantum dots [65,88]. These challenges have made the problem of how to eliminate background signals without compromising image quality even more difficult [88]. To compensate for the background arising from the re-excitation in CW-STED, where the pulsed fluorescence excitation is combined with the asynchronous depletion by a continuous-wave laser, several strategies like phasor analysis and elaborate schemes for the deconvolution of multiple images have been devised [89–92]. A broad class of methods called STED-only subtraction or sub-STED for short, compensates for the background arising from the direct excitation. In sub-STED, the acquired conventional STED image is subtracted by a background image acquired using only the STED beam. Consequently, this method does not consider the incomplete depletion and does take into consideration the re-excitation problem [88,93]. Another possibility for background suppression was presented by gating the fluorescence detection time with TCSPC cards [90,91,94].

To address the problem with the STED background, stimulated emission double depletion (STEDD) nanoscopy was introduced in 2017 [65,73]. In STEDD microscopy, each scan

position is first illuminated by a Gaussian-shaped excitation pulse, which is then followed by conventional depletion pulses featuring zero intensity at the center (see Figure 3.9). The photons detected during the first few nanoseconds are used for what is referred to as the STED1 image, which contains signal (I_{sig}) and background (I_{bg1}) photons [71,73]. A subsequent, much weaker depletion pulse formed in the Gaussian profile, about tenfold weaker and peaking at the center, later removes the high-frequency, super-resolved signal, leaving behind only the low-frequency background (I_{bg2}) recorded in the STED2 image [71]. As was shown in Figure 3.1 and Figure 3.2, using a delay line, the time gap between the modulated depletion pulses (donut and cylinder) and the unmodulated depletion pulse (Gaussian) is carefully adjusted to the fluorescence lifetime of the dye marker so that most of the photons detected reinforce the high-frequency STED1 image [71,73]. In other words, STEDD technique measures the STED and background intensities in the 25-ns period between two 40-MHz excitation pulses. This method of collecting STED and background images at the same time is superior to methods that collect them one after the other [74] because it allows for real-time imaging and is less likely to drift. The final STEDD image is generated by subtracting the STED2 image from the STED1 image on a pixel-by-pixel basis using a single global weighting factor. The physical principle of the STEDD approach can be summarized as:

$$\begin{cases} I_{STED1} = I_{sig} + I_{bg1}\,, \\ I_{STED2} = I_{bg2}\,, \\ I_{sig} = I_{STED1} - \gamma I_{STED2} = I_{STEDD}\,. \end{cases} \tag{3.4}$$

Here, the coefficient γ shows the ratio of background intensities $\frac{I_{bg1}}{I_{bg2}}$ [65]. Since the weight factor is constant across the entire ROI, this approach is also called global STEDD. The probability of photon emission within the two intervals during which photons contributing to I_{STED1} and I_{STED2} are acquired determines the weight parameter [65,71].

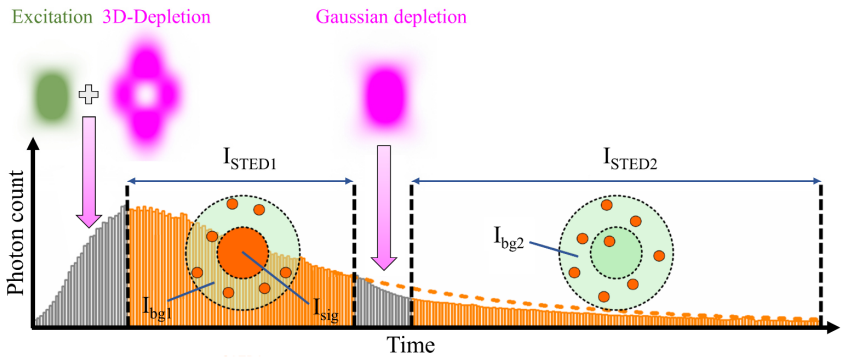

Figure 3.9: Illustration of the STEDD technique. The method utilizes a Gaussian excitation pulse in conjunction with two modulated depletion pulses (donut and cylinder beams) to measure signal plus background (I_{STED1}) and then with a gaussian depletion pulse to collect background photons (I_{STED2}). The image intensity is denoted as I_{sig}, while I_{bg1} and I_{bg2} correspond to the background signals included in I_{STED1} and I_{STED2}, respectively. Modified according to [73].

It should be noted that, the up-sampled, low-frequency STED2 image is smoothed using a Gaussian low-pass filter to diminish the effects of high-frequency random noise. The effectiveness of background correction is highly dependent on selecting the appropriate background weights. Various criteria can be considered to determine the optimal weighting factor, γ. Previously, a method was proposed that relies on maximizing the high-frequency components in the spatial frequency spectrum of the optimally corrected STEDD image as a criterion for choosing this factor [65]. Another, more time-efficient method is using least-squares minimization to estimate the optimal weight factor [71,95]:

$$\gamma = \arg min \parallel I_{\mathrm{STED1}} - \gamma' I_{\mathrm{STED2}} \parallel^2 . \qquad (3.5)$$

Applying a single global value of γ for background correction across the region of interest yielded consistently satisfactory STEDD imaging in thinly labeled samples, with the results being identical when using either calculation method [71]. Figure 3.10 compares standard confocal, conventional STED, and STEDD imaging of immobilized 40 nm polystyrene DRBs on a coverslip, demonstrating a significant improvement in resolution with STED. Closer inspection of the latter images reveals diffuse halos around the sharp features in the STED images. These are attributed to re-excitation by the STED beam and incomplete fluorophore depletion at the edges of the focal region. As a remedy, STEDD efficiently suppresses this undesired background signal (see Figure 3.10 a). This improvement is also obvious in the intensity profiles shown in this figure. STED profile needs to be fitted with two Gaussian components, one for the signal and one to account for the background. In contrast, single Gaussian functions precisely model the intensity profiles for confocal and STEDD images (see Figure 3.10 b).

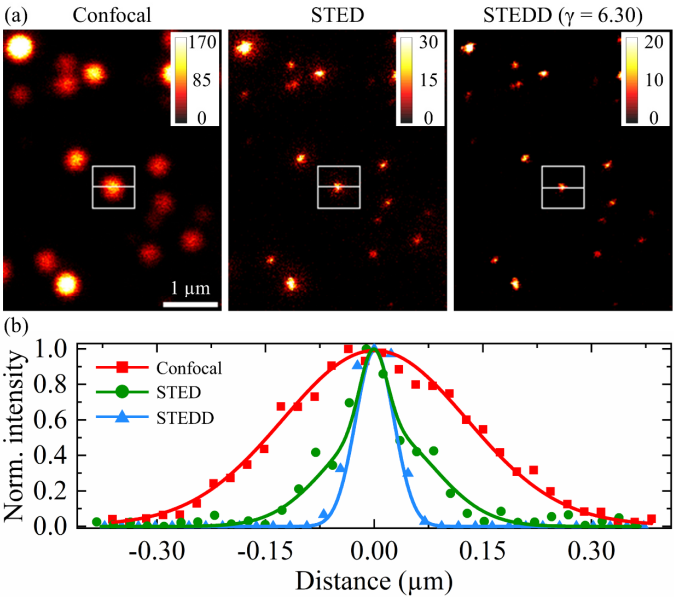

Figure 3.10: Confocal, STED, and STEDD imaging of 40 nm beads. **(a)** Confocal, STED, and STEDD imaging of 40 nm polystyrene dark red beads acquired by applying the excitation pulse only, adding the donut conventional STED pulse and adding both donut and gaussian STED pulses, respectively. The donut and Gaussian depletion beams delivered 120 mW and 12 mW of power, respectively, at the sample plane. Scale bar is 1 µm. **(b)** Intensity profiles (symbols) along the lines in (a). Here, solid lines are Gaussian fits.

In this section, the necessity of using a powerful background subtraction technique in conjunction with STED as a super-resolution microscope was focused on, and the working principle and experimental implementation of this approach were further investigated. In Chapter 4, the performance of this approach on densely biologically labeled samples was deeply explored, the strengths and weaknesses of this approach were identified, and a robust technique was proposed to further optimize this background correction for accurate qualitative and quantitative study of subcellular biological processes. Development and application of the proposed method form a significant part of the thesis in free-background super-resolution imaging.

Chapter 4: Pixel-Level Background Correction in STEDD Nanoscopy Using Local Weight Factor Calculations

4.1 Introduction

Background intensity contributions degrade fluorescence microscopy images. As was discussed in previous chapters, researchers have developed several strategies to eliminate background in STED images, some of which involve capturing a separate background image and subtracting it from the STED image using a global weighting factor, a method known as stimulated emission double depletion (STEDD) [65,73]. However, it turns out that in the densely labeled samples imaged with STEDD nanoscopy, the weighting factor varies locally. The corollary of this would be that a single, global weighting factor used for background subtraction results in local artifacts due to incorrect correction. In this chapter, an improved method will be presented that corrects the improper subtraction problem found in ROI-wise (traditional) STEDD and other related techniques. This method defines the local subtraction weight factor within small windows centered on each pixel; this delivers a precise level of background subtraction for pixels. This conceptually simple algorithm, which is already published in a specialized journal [71], works remarkably well and can be extended to other imaging methods where background image subtraction is required.

4.2 Motivation and Significance of the Study

Previous studies have demonstrated that background correction using a single, global value is effective for sparsely labeled samples such as polystyrene beads or Hela cell microtubules, producing satisfactory STEDD images [65,73] since these samples do not include structures with widely varying pixel intensities. However, densely labeled samples, such as those in thick and tightly packed biological tissues, pose a much more complex challenge in this regard. Such samples, like the embryonic cells of zebrafish, are of particular interest in microscopy and biological research because they give a more holistic view of cellular interactions and also

depict fine structural and process details that may go unnoticed in the case of sparsely labeled or thinner samples. In this chapter, STEDD imaging was applied to cell nuclei from zebrafish embryos fixed at the spherical stage to investigate the highly challenging issue of improper background correction in tightly labeled samples and introduce a solution, enabling a rigorous evaluation of the proposed approach [71]. In this study, the compactly labeled samples were prepared using a standardized immunofluorescence staining procedure (see Appendix B.2). RNA polymerase II (Pol II) proteins were targeted with a primary antibody (Rat IgG, 3E8, Active Motif) and subsequently stained with the STAR RED dye conjugated to a secondary antibody (anti-rat IgG, Abberior). This labeling strategy highlights the spatial distribution of Pol II proteins carrying the serine 5 phosphorylation mark, which are known to aggregate into clusters near transcriptionally active genes.

Figure 4.1 shows the distribution of Pol II Ser5P structures within a cell nucleus in the STED1 (signal plus background) and STED2 (mainly background) images, as well as the background-corrected image (STEDD). To acquire images using the home-built microscope, STAR RED fluorescent molecules were excited by a pulsed diode laser at 640 nm with a power of 3.2 μW and a repetition rate of 40 MHz. The depletion beam at 779 nm with a power of 66 mW running at a 40 MHz repetition rate was split by a polarization-maintaining beam splitter such that 90% of the power was devoted to the vortex phase-modulated STED1 pulse, whereas 10% passed into the delayed Gaussian STED2 pulse [71]. Image acquisition was performed on 15×15 μm² ROIs using a pixel dwell time of 20 μs, a step size of 30 nm, and a five-line repetition rate.

As can be seen in Figure 4.1, the STED1 image presents an intense background signal superimposing the true fluorescence signal from Pol II Ser5P clusters in the nucleus. By using traditional STEDD microscopy with the calculated global weighting of 6.40 across the entire ROI, one can easily observe the presence of artifacts in the background-corrected image, such as over-subtraction in the middle and under-subtraction in the periphery region of the nucleus. Since this weight factor represents a trade-off based on the entire ROI, this approach suffers from under-subtraction in the regions of high pixel intensities where gamma is not enough to raise the background to be excluded from the STED1 image. On the other hand, in regions of low pixel intensity values, the weight factor becomes so high that it leads to over-subtraction. This observation suggests that in images of densely labeled biological samples with highly variable pixel intensities across a given ROI, the specific characteristics of each region in the image influence the factor.

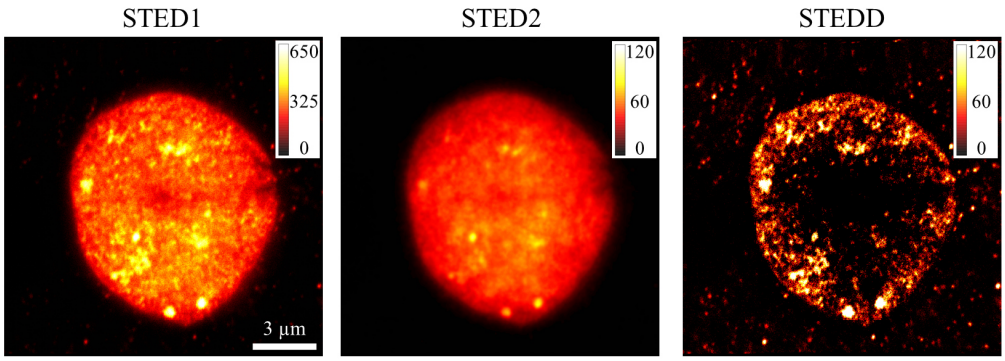

Figure 4.1: Improper background subtraction in tightly labeled samples. STED image of Pol II Ser5P structures in zebrafish embryonic cells after background correction using global weighting based on equation (3.5). Scale bar: 3 µm.

One of the advantages of the double depletion technique over the pure computational background subtraction that can be understood from Figure 4.1 is that this technique measures directly the high- and low-frequency components, namely signal and background, respectively, during acquisition, while pure computational methods [96–100] mostly estimate a cut-off in the frequency domain to guess what the background might be. This may easily introduce some artifacts in the cleared background images because of the less accurate estimation, especially for these complex samples whose structures with different sizes have a wide and rather smooth transition between high- and low-frequency components.

Note that to reduce noise before calculating the STEDD image, a low-pass filter should smooth the STED1 and STED2 images [65]. Herein, the STED1 image was filtered using a low-pass Gaussian filter with a standard deviation, σ, of 0.5 pixels that yielded an FWHM of 35 nm, approximately half of the PSF's width at STED resolution at 60 mW donut depletion beam power. This consideration is needed to make sure that the super-resolution characteristics of the image are not compromised. Furthermore, a low-pass Gaussian filter of standard deviation σ = 2 pixels (corresponding to a FWHM of 141 nm), which is considerably smaller than the FWHM of confocal imaging measured to be 322 ± 21 nm according to the immobilized fluorescent nanobeads (Ø 40 nm, dark red fluorescent (660/680 nm), ThermoFisher Scientific), was used for smoothing the low-frequency STED2 image [71]. As a result, the background does not undergo substantial flattening. It should be clarified that the STED2 image's filter size has some order of dependency on the natural frequency distribution of the sample structures. The Gaussian filter width applied to this image should be smaller than the confocal PSF if the frequency spectra of the signal and the background do not overlap appreciably, a condition typically met in super-resolution microscopy. However, if the sample itself contains extensive clusters such that their convolution with the microscope PSF results in image features

comparable or wider than the confocal PSF, then the STED2 image should be smoothed with a greater filter width than usual in order to preserve the true fluorescence signal.

4.3 Algorithm for Calculating Local Weight Factors

The local γ assignment process is schematically shown in Figure 4.2. This calculation begins with the input STED1 and STED2 images, which are first extended using symmetric padding. This padding mirrors the edge pixel intensities to ensure that a full analysis window can be centered on every pixel in the image, including those at the borders. Next, for each pixel, a square window of fixed odd size is defined, centered on that pixel. Within each window, the γ value is computed using equation (3.5), which incorporates the local intensity information from both STED images. The resulting γ value is then assigned to the central pixel of that window. By repeating this step across the entire image, a complete γ map is generated, providing spatially resolved γ values across the field of view [71].

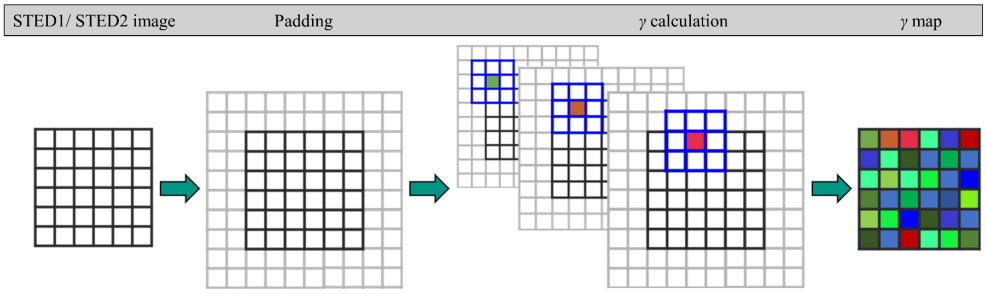

Figure 4.2: An illustration of the working principle of the local gamma calculation approach. The starting point is the input images, STED1 and STED2, which are then extended by symmetrical padding with gray pixels around the black ones. Next, the value of γ is calculated in a tiny square surrounding each pixel. This value is subsequently assigned to the pixel in the middle of the area. Modified according to [71].

As expected, the accuracy of this technique depends on the size of the local windows. The minimum size of these windows is limited by the confocal PSF at the excitation wavelength, which defines the spatial variations of the STED background due to incomplete depletion. Background noise that arises from out-of-focus fluorescence can introduce wider characteristics into the image. Furthermore, re-excitation background results in broader intensity features due to the less tightly focused depletion beam, which arises from a far red-shifted wavelength. In other words, the window size should be sufficiently large to capture slow, gradual background intensity variations; otherwise, the optimization of equation (3.5) will not make much sense. Taking these considerations into account, a window size slightly larger than the width of the confocal point spread function (11×11 pixels) suffices to achieve an appropriate background correction that results in an optimally sharp image [71].

4.4 Results and Discussions

4.4.1.1 Comparison Between Global and Local Weighting Methods

As an initial attempt to evaluate the performance of this approach compared to global STED calculation, a window size of 1.5 times the confocal PSF (17×17 pixels) was considered. Figure 4.3 qualitatively compares the performance of global and local background subtraction approaches in STEDD nanoscopy. The STEDD image was obtained by subtracting the signal plus the background (STED1) image from the background (STED2) image using either a global weighting factor (upper right) or a local weighting factor (lower left). The two calculating approaches lead to significant differences. Background correction using a global γ value of 7.9 across the whole image causes excessive background removal, producing significant vacant regions close to the center, indicating an over-subtraction of the background combined with an under-subtraction at the edges of the cell nucleus and regions that cluster were closely packed. On the other hand, local background subtraction results in a precise and homogeneous fluorescence distribution of the Pol II clusters compared to the reference (STED1) image [71].

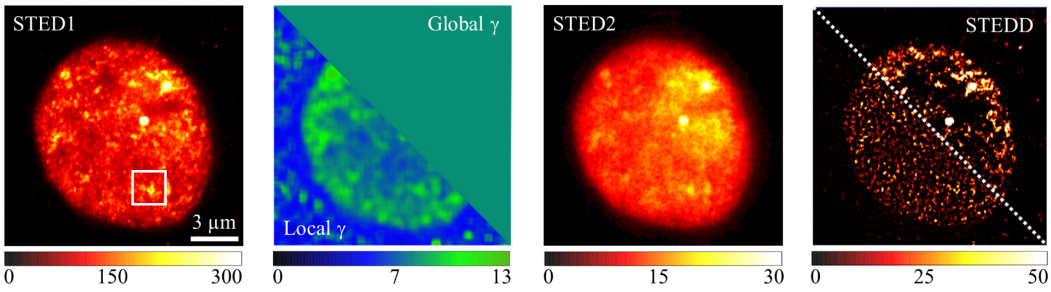

Figure 4.3: Background correction using different weighting methods. Background correction using both local and global weighting approaches of a STED image acquired from Pol II Ser5P structures in zebrafish embryonic cells. Scale bar is 3 µm. The white box indicates the close-up region for Figure 4.4. Taken from [71].

4.4.1.2 Refinement of the Local Weighting Calculation Procedure

While the method here proposed reveals a potent remedy to spurious background correction with a single weighting factor, further detailed quantitation is required in order to identify and implement any necessary refinements. To this end, it is instructive to focus on a challenging region within a compact area featuring a few clusters of Pol II Ser5P. Figure 4.4 shows the zoomed area of some clusters in proximity, as represented in STED1, STED2, and STEDD images respectively, and the relative gamma map. As qualitatively demonstrated in Figure 4.4a, local background subtraction efficiently removed the overwhelming, superimposed low-frequency background of the STED1 image, leading to a meaningful correction. This procedure preserved all clusters, regardless of their signal intensity, transforming the STED1

image into a super-resolution, background-free representation. However, looking at Figure 4.4b, showing the intensity profiles of the STEDD image along the dashed line, it appears that this method, although very powerful, suffers from the fact that some areas of the STED1 image, where only noise-level pixels are surrounded by high-intensity pixels in the local window, undergo too much background subtraction.

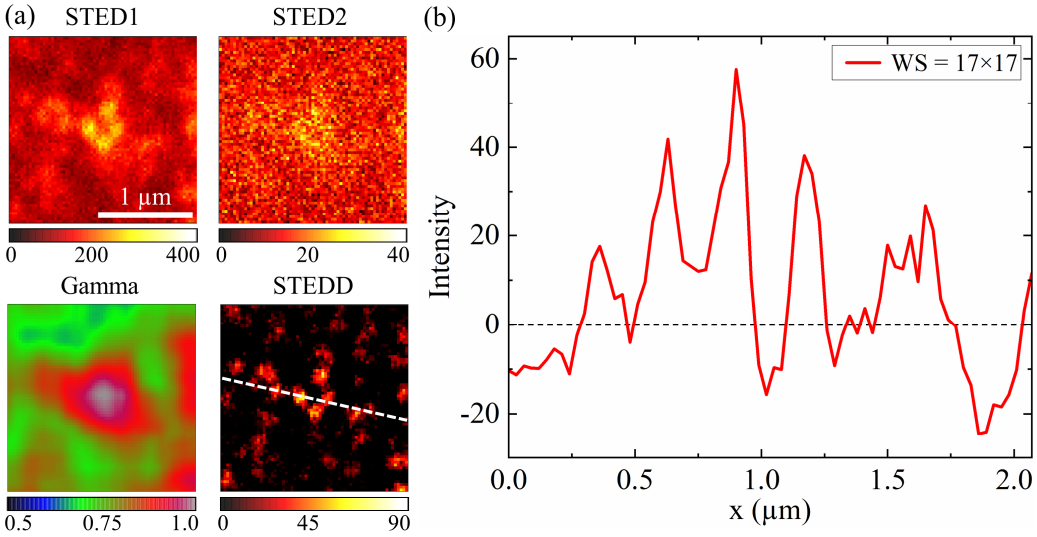

Figure 4.4: Examination of local STEDD approach for Pol II Ser5P clusters. (a) Evaluation of the local STEDD approach effectiveness, featuring close-up views (2×2 µm^2) of Pol II Ser5P clusters in STED1, STED2, the γ map (scaled within [0,1]), and STEDD images. **(b)** Intensity line profile across the STEDD image, represented by the dashed line.

One might intuitively consider a possible solution to this problem, which could be to decrease the size of the window below the dimensions of the confocal PSF, 11×11 pixels; however, as considered previously from a physical point of view, this is not meaningful. Nonetheless, it may still be informative to investigate how regions of the STED1 image that are solely included in noise are impacted by background subtraction when the window size is reduced. As observed qualitatively in Figure 4.5a, reducing the window size below 11×11 pixels for calculating the gamma map and performing background correction significantly distorts the cluster morphology. In the extreme case of a 3×3-pixel window, clusters are almost entirely eliminated, leaving behind a predominantly noisy image. Furthermore, Figure 4.5b compares the intensity profiles of STEDD images obtained using local calculations with different window sizes along the dashed line. In line with panel (a), it is evident that decreasing the window size progressively eliminates clusters. This is reflected in the gradual reduction of the intensity distribution width for each cluster, eventually capturing only noise levels at smaller window sizes. As previously discussed, the window size needs to be large enough to

accommodate moderate, steady changes in the background intensity. Otherwise, the optimization of equation (3.5) becomes less meaningful.

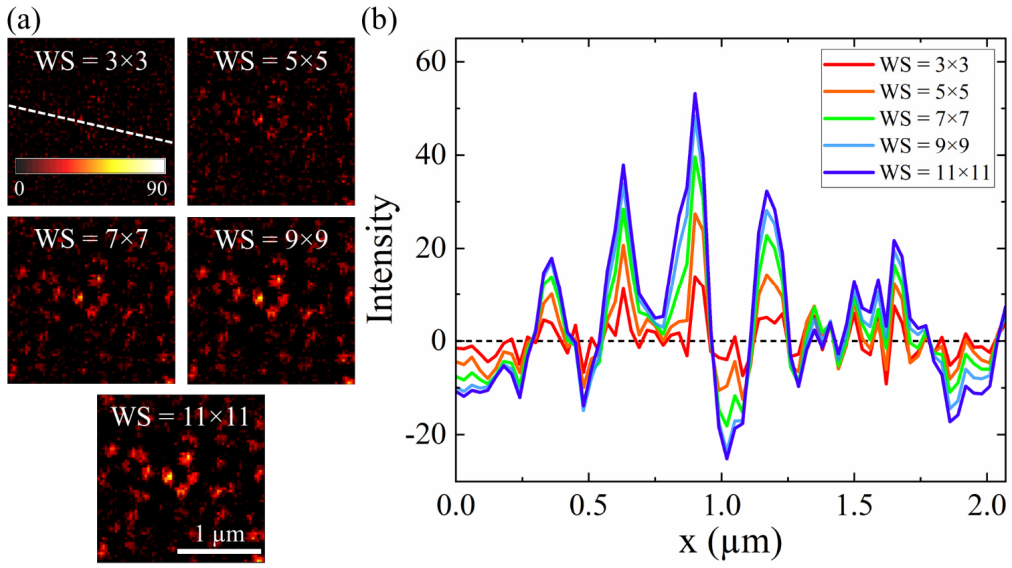

Figure 4.5: Effect of window sizes on over-subtraction in STEDD images. (a) Qualitative and **(b)** quantitaive investigation of the effect of window sizes smaller than the confocal PSF on the over-subtraction issue in regions containing only noise pixels. All STEDD images are shown on the same contrast range.

As shown in Figure 4.5, it is clearly not possible to simply shrink the window size for calculating the weight factor for the entire ROI. However, this exercise did lead to an important observation: in order to correct for over-subtraction in areas dominated by pixel-level noise, the calculation procedure may be improved by re-estimating the weight factor in a small 3×3-pixel window just for pixels whose intensities are determined to be negligible. This window size was observed to be the smallest possible for gamma factor calculation, effectively limiting its use to capturing noise pixels. More specifically, the γ value is computed likewise for each very low-intensity pixel, identified by the condition $I_{STED1} \leq \gamma(I_{STED2} + \delta)$, where δ represents the standard deviation of I_{STED2} within the window, within a small 3×3-pixel window [71]. In the final step, all negative pixel intensities caused by this operation are set to zero to prevent nonphysical gray values on STEDD images.

Figure 4.6 shows a qualitative and quantitative comparison between the initial local-based calculation approach and the refined version. Figure 4.6a illustrates how the refined approach can significantly improve the accuracy of gamma factor calculation for each single pixel, while sudden changes in image intensity naturally could be reflected. On the other hand, the initially proposed approach appears to be less sensitive to these changes resulting in a smoother gamma map and over-subtraction when very low-intensity pixels are present. Figure 4.6b illustrates

the effects of refining the locally based calculations. Especially, cluster-containing regions are unchanged and the amplitude of negative pixels is reduced significantly, which further shows the effectiveness of such refinement in solving this issue.

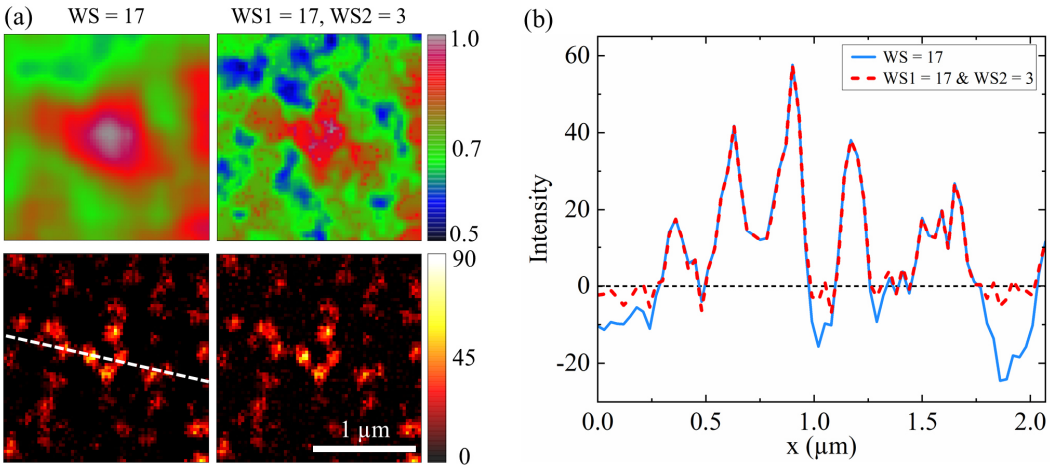

Figure 4.6: Comparison of the initially proposed and refined local-based weight factor calculation approaches: (a) close-up views of selected regions, and **(b)** corresponding intensity line profiles across the dashed line. In the refined approach, the main window size (WS1) was set to 17×17 pixels, while WS2 for the gamma estimation for noise-level pixels was set to 3×3 pixels.

4.4.1.3 Investigation of the Optimal Window Size for Local Weighting Calculation

As first shown in Figure 4.3 and further demonstrated in Figure 4.6 after refining the calculation approach, the localized analysis of the weight factor (γ) significantly enhances the accuracy of background subtraction compared to the global estimation. Whereas the gamma estimation window for noise-level pixels should be fixed to the smallest possible computation size (3×3 pixels), the local feature variations in the images were examined by adjusting the main window size (initially set to 17×17 pixels). This analysis aimed to evaluate the influence of the main local window size on the quality of the STEDD images and to identify the optimal window size for gamma estimation around each pixel. In Figure 4.7, using window sizes of 11×11, 17×17, and 33×33 pixels, the γ distributions and the corresponding STEDD images are assessed [71]. For a more straightforward labeling in this figure, the aforementioned window sizes are referred to as WS 1.0, WS 1.5, and WS 3.0, respectively, with a pixel number adjusted to the FWHM of the confocal PSF. According to this study, as the window size grows, the maps progressively blur. As expected, this leads to a significant increase in the black regions within the STEDD images (Figure 4.7a). This effect is due to the fact that when the window size increases, too much background information can be subtracted from pixels with low intensity,

especially those next to the areas with high intensity in the narrow window. The effect of over-subtraction increases the regions of low intensity, thus reducing the contrast or precision in distinguishing between the signal and background in regions where there is significant variation in pixel intensity across the image [71]. Hence, an appropriate selection of the window size is necessary to preserve the accuracy of background subtraction and sustain the integrity of the subtle details in the image. From the analysis of the line profiles, as represented in Figure 4.7b, it is obvious that the peaks underwent broadening and lost sharpness with the increase in the window size (WS). This would imply that a local background correction with a window size in the range WS 1.0–WS 1.5 should work optimally, as it preserves sharper peaks and better separation between features [71].

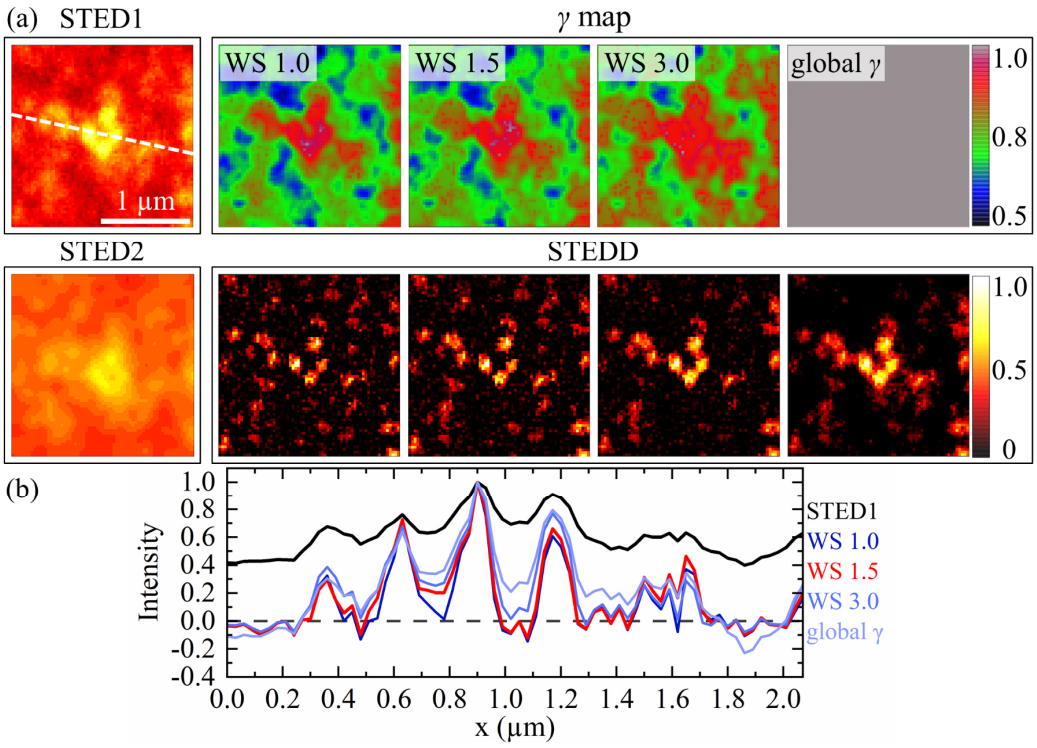

Figure 4.7: Variation of the STEDD image based on the window size of the background calculation. (a) The STED1 and STED2 close-up images of a region inside a cell nucleus of a zebrafish embryonic cell are shown on the left, with corresponding γ maps and resulting STEDD images for different window sizes (WS 1.0, WS 1.5, WS 3.0) and a global γ value. These images are normalized in intensity within the range of 0 to 1. **(b)** Both global and local background corrections were carried out with varying window sizes to produce the normalized STEDD intensity profiles corresponding to the dashed line. The profile from the original STED1 image is also included to highlight the variations resulting from different correction methods. Taken from [71].

Figure 4.8 clearly shows a difference between the global and local background removal techniques by fully representing a cell nucleus. A locally determined weighting factor results in a balanced distribution of Pol II enzyme clusters throughout the image, as shown in Figure 4.8a. While using a global weighting factor, high intensities are observed in the periphery of the STEDD image, while extended regions of zero-intensity pixels arise in the center as a result of overly intensive background subtraction. The advantage of the local-based calculation approach becomes even more visible in the close-up views, where the local background correction preserves the fine details better no matter how weak the input signal is [71].

Further insight is obtained by analyzing the line profile shown in Figure 4.8b. The raw STED1 image exhibits high-resolution features that are superimposed on a large background level. Applying a global γ correction leads to overshooting, creating regions of negative intensity, which must be set to zero and can obscure critical information. By use of locally computed γ values, on the other hand, this overshoot is avoided, ensuring accurate subtraction [71]. Moreover, the subtle features in the STED1 image are retained accurately after the local correction, as supported by the line profile. This emphasizes how significantly better local background weighting preserves minute structural elements. The figure therefore brings out the importance of developing local background subtraction methods, as a global approach heavily distorts fluorescence data in the image. Any quantitative analysis like intensity, count, and morphological features such as cluster solidity, based on such global methods, will be totally off the mark. It can also be comprehended from this figure that, whether the STED2 image is acquired by either Gaussian double depletion [65,73] or polarization switching of the donut beam [74], the use of one weighting factor for subtraction leads to severe errors in background subtraction at high labeling densities.

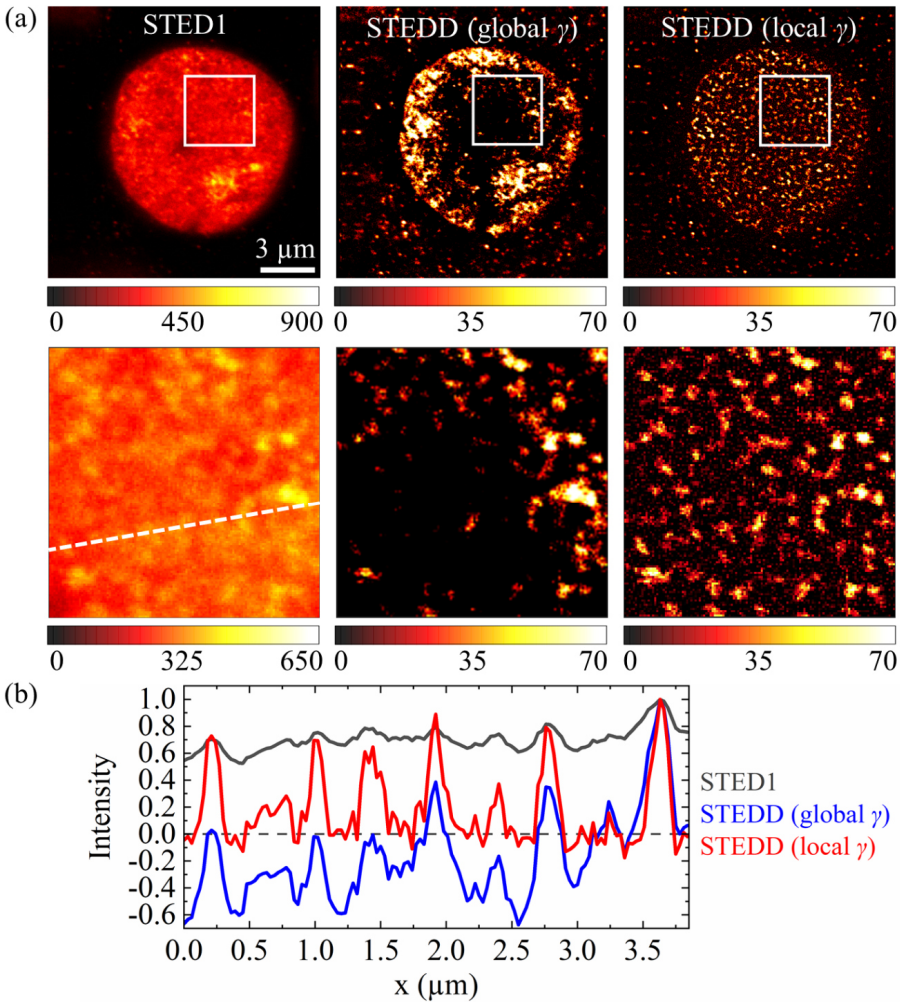

Figure 4.8: Comparison of STED1 and STEDD images with global and local gamma calculation methods. Qualitative comparison between **(a)** STED1, and resulting STEDD images based on global, and local (at WS 1.5) gamma calculation methods. Scale bar is equal to 3 µm. The second rows of every column display a magnified view of the white rectangular box. **(b)** Normalized intensity profile comparison across the white dashed line between different approaches. Modified according to [71].

4.5 Conclusions

In this chapter, a method to achieve proper background subtraction in super-resolution microscopy was introduced. The weighting factor (γ) for each pixel in the STEDD nanoscopy was precisely determined by the local analysis of STED1 and STED2 images. To ensure equitable background correction in regions with varying background levels and intensities, it was concluded that the window size should be slightly larger (~1.5 times) than the FWHM of the confocal PSF. This study proved that the local analysis technique solves the under- and over-subtraction difficulties inherent in classic STEDD. This accomplishment has wide implications in biological imaging and quantitative analyses by improving the resolution and contrast of the STED image through the effective reduction of the low-frequency background

noise required for the visualization of complex cellular structures and dynamic processes at high spatial resolution. Moreover, by enhancing the signal-to-noise ratio, the algorithm allows for quantitative analysis with high precision, which leads to correct segmentation and measurement of the morphological properties of the structure under consideration. This becomes important in applications concerned with the quantification of the spatial organization of different proteins within a cell, the number of clusters, the compactness level of polymerase clusters, genomic material density, and such about molecular interaction.

It is important to underline that the suggested local background subtraction technique is relevant for several image-subtraction-based scanning microscopy systems covering a spectrum of STED technologies [88,101,102]. Also, it can be integrated into techniques like fluorescence emission difference (FED) [103], differential-aberration two-photon excited fluorescence (DA-TPEF) [104], and switching laser mode (SLAM) [105] microscopy.

Additionally, as was mentioned, the work presented in this chapter has already been published in a scientific journal [71]. The contributions of the co-authors were as follows: Andrei Kobitski and Siqing Dai participated in the scientific discussions. Süheyla Eroğlu-Kayıkçı was responsible for collecting and fixing zebrafish embryos. Lennart Hilbert supervised me through the immunofluorescence staining procedure. Karin Nienhaus assisted with the refinement of figures for the manuscript. G. Ulrich Nienhaus supervised the project and contributed to the conception, discussion, and interpretation of the results, as well as to the writing of the final manuscript.

Chapter 5: Multi-Color 3D STEDD Nanoscopy of Transcriptional Cluster Architectures and Inhibitor-Induced Chromatin Access Modulation in Zebrafish Embryonic Cells

5.1 Introduction

The regulation of gene expression by RNA polymerase II (Pol II) is critical for cellular function, differentiation, and development. The engagement and activation of Pol II are key in transcription, which involves a unique spatial and temporal organization of machinery, especially at super-enhancers in pluripotent and developing cells. In this chapter, the custom-built 3-channel, 3D-stimulated emission double depletion microscopy is employed to reveal the nanoscale structure and dynamics of these transcriptional clusters, which diverge from canonical enhancer-promoter models to form stable, large, and spatially constrained clusters that drive robust gene expression. The response of transcriptional clusters and their chromatin environments to chemical perturbations, including JQ1, hexanediol (Hex), triptolide (TL), and flavopiridol (FP), which affect Pol II-mediated transcription, is investigated using STEDD microscopy in zebrafish embryos. This technique enables high-resolution imaging of Pol II with two different phosphorylation marks, as well as associated chromatin structures, providing new insights into the molecular architecture underlying transcriptional regulation during early development. Moreover, in this work, robust techniques for cluster segmentation and characterisation are presented, therefore enabling a thorough investigation of transcriptional structure.

5.2 Motivation and Significance of the Study

The operating processes in a cell generally include a network of transcriptional regulations that drive complex patterns of gene expression underlying the generation of cellular phenotypes

and, eventually, tissue morphology in embryonic development [106]. One important process in normal cell development involves proper regulation of active transcription for some genes [107,108]. Active transcription of particular genes requires engagement and activation of Pol II through various signaling pathways or molecular interactions. It is, therefore, of essence to understand the modes of regulation of Pol II activity if the complexity of gene regulation in cellular differentiation, development, and disease is ever to be unraveled [109]. These molecular processes that control transcription in stem cells can be effectively studied using super-resolution microscopy techniques.

Imaging sub-nuclear structures poses an enormous experimental challenge. This is due to the fact that highly compacted chromatin and related factors will tend to produce an overwhelming background that might obscure the signal of interest. As was shown in the previous chapter, a particularly effective solution is STEDD microscopy using local weight factor calculations [73]. This method precisely measures the image background at low frequency and subtracts it, pixel by pixel, from the super-resolved image [71], thereby bringing the subdiffraction cellular landscape into sharper focus. Furthermore, advanced fluorescence-labeling methods, in combination with multi-channel detection layouts, have provided spatial mapping of interactions between various components of the transcription machinery and chromatin [110]. These developments, combined with super-resolution fluorescence imaging techniques, have allowed us to investigate complex, three-dimensional nanoscale organizations within cellular structures [63,111]. This includes examining the dynamic configuration of transcriptional complexes in the cell nucleus during gene activation and elongation processes [35,112–115].

Recent developments in super-resolution imaging have underlined the intricate interaction between molecular transitions, spatial organization of genomic areas, and biophysical processes in transcription regulation in stem cells [116,117]. However, the precise interaction of these regulatory steps, the driving biophysical mechanisms, and the spatial organization of transcriptional clusters and their chromatin environment remain incompletely understood. This work investigates the nanoscale distribution of recruited Pol II, transcriptionally active Pol II, and chromatin in pluripotent zebrafish embryos using a custom-built 3-color 3D-STEDD nanoscopy with single-pixel background correction. This approach helps to visualize the intertwined organization of key components within transcriptional hubs and to probe how transcriptional inhibitors, such as JQ1, Hex, TL, and FP, affect nuclear architecture.

5.3 Materials and Methods

5.3.1 Biological Sample Preparation for 3-Color, 3D-STED Microcopy

This section aims to discuss the sample preparation procedure that was implemented to investigate the spatial distribution of DNA, recruited Pol II, and elongating Pol II within intact, pluripotent zebrafish embryos.

The full embryo immunofluorescence staining process is described in this section; a more detailed version can be found in Appendix B.2. At the fish facility of the Institute of Biological and Chemical Systems, embryos were produced through natural mating. After collection, embryos were dechorionated using Pronase enzyme and maintained at 28.5°C in agarose-coated dishes [35]. Furthermore, in cases where treatment with transcription inhibitors (JQ1, Hex, TL, and FP) was needed, the inhibitors were resuspended in DMSO to achieve the recommended effective concentrations. All of these steps which were taken as a follow-up to earlier publications [35,118,119], ensured that the preparation of the embryos of zebrafish would be healthy and uniform for further experimental studies. Sphere-stage embryos were fixed overnight at 4°C using a solution of 2% formaldehyde and 0.2% Tween-20 in 0.3× Danieau's embryo media. After the animal cap regions were permeabilized at room temperature for 15 minutes with 0.5% Triton X-100 in PBS, they were washed three times in PBST for 10 minutes each and then blocked with 4% BSA in PBST for at least 30 minutes [35]. Primary antibodies: rat anti-Pol II Ser5P (3E8, 1:300, Active motif), rabbit anti-Pol II Ser2P (EPR18855, 1:300, Abcam) were incubated overnight at 4°C in 4% BSA in PBST solution [35]. The following day, secondary antibodies were applied under the same conditions: goat anti-rat IgG conjugated with STAR RED (1:300, Abberior Instruments, Göttingen, Germany) and goat anti-rabbit IgG conjugated with STAR 460L (1:300, Abberior Instruments, Göttingen, Germany). To remove unbound antibodies, primary and secondary antibodies were washed off extensively using three 5-minute washes in PBST. Following this step, to ensure long-term preservation of antibody staining, samples were refixed with 4% formaldehyde for 15 minutes. Lastly, to add the third channel, the DNA stain (5-TMR-Hoechst) was diluted in glycerol, and the deyolked animal caps were mounted on #1.5 coverslips using this solution [35].

5.3.2 Parameter Settings for Multi-Color 3D STEDD Image Acquisition

The advanced custom-made STEDD microscope, as described in the third chapter, was used to acquire 3-color 3D microscopy images from the animal caps of whole, fixed embryos (5). In the merged dataset from two completely independent experiments, approximately 24 nuclei were measured for both the control and each treatment, using consistent acquisition settings. Regions of interest measuring 14 µm × 14 µm × 3 µm were imaged with lateral and axial pixel sizes of 31 nm and 120 nm, respectively. Furthermore, three times line averaging was used for data acquisition, while the pixel dwell time was set at 20 µs. 470 nm, 560 nm, and 640 nm laser excitation powers for STAR 460L, 5-TMR-Hoechst, and STAR RED were set to 3.70 µW, 1.30 µW, and 2.30 µW, respectively. In addition, $P_{\text{Donut-779}}$, $P_{\text{Cylinder-779}}$, and $P_{\text{Gaussian-779}}$ were configured to 60 mW, 30 mW, and 6 mW at the sample plane, respectively.

5.3.3 General Overview of Image Analysis

In this study, MATLAB (Version R2023a) [120], FIJI [121], and 3D Slicer [122] softwares were utilized for 3D image analysis and reconstruction.

5.3.4 Bleaching Correction and Cluster Segmentation

The intensities recorded in the image stacks for the Pol II Ser2P, Pol II Ser5P, and DNA channels are expressed as follows:

$$
\begin{aligned}
I_{S2P}(i,j,k) &= \alpha_{S2P}(k).I^0_{S2P}(i,j,k) + \beta \cdot \alpha_{DNA}(k) \cdot I^0_{DNA}(i,j,k) + I^B_{S2P}\,, \\
I_{S5P}(i,j,k) &= \alpha_{S5P}(k).I^0_{S5P}(i,j,k) + I^B_{S5P}\,, \\
I_{DNA}(i,j,k) &= \alpha_{DNA}(k).I^0_{DNA}(i,j,k) + I^B_{DNA}\,.
\end{aligned}
\tag{5.1}
$$

The measured intensities offer statistical information on the genomic material content in the obtained images and the distribution of the Pol II phosphorylation states, like Ser2P and Ser5P. The voxel coordinates in the lateral (x, y) and axial (z) dimensions are shown here by the indices i, j, and k, respectively. The subscripts S2P, S5P, and DNA designate the three channels, while $I(i,j,k)$ denotes the intensity of pixels i, j of image frame k. In this regard, I^0 represents the real fluorescence signal, unaffected by bleaching. The background signal, which contains no fluorescence information, is given by I^B. The parameter α corresponds to the bleaching coefficient, capturing the extent of signal reduction due to photobleaching. Moreover, included is β to account for any cross-talk between the DNA and the Pol II Ser2P channels, ensuring an exact evaluation of the intensities.

The images obtained in the Ser2P channel were first adjusted to account for the emission intensity produced by the direct excitation of the DNA stain, 5-TMR-Hoechst, which was detected within the Ser2P channel using:

$$I'_{S2P}(i,j,k) = I_{S2P}(i,j,k) - \beta I_{DNA}(i,j,k)\,. \tag{5.2}$$

This is a correction in order to ensure that any fluorescence signal stemming from the DNA label does not obscure or contribute to the actual fluorescence of interest corresponding to Pol II Ser2P with the intent of refining the data output from this channel. The value $\beta = 0.15$ reflects the slight absorption cross-section of 5-TMR-Hoechst at 470 nm, along with the fact that the power of the 470-nm excitation laser was three times greater than that of the 560-nm laser. By applying this correction, the (5.1) equations can be expressed in an identical way for each detection channel:

$$I'(i,j,k) = \alpha I^0(i,j,k) + I^B\,. \tag{5.3}$$

The background-corrected fluorescence signal I'', which compensates for unwanted free-fluorescent background interference, can be formulated as:

$$I''(i,j,k) = \alpha I^0(i,j,k) = I'(i,j,k) - I^B\,. \tag{5.4}$$

Low-frequency fluorescence signal at the individual pixel level was already removed in the STEDD microscope images. However, to further eliminate high-frequency noise, a fitting procedure was employed. Specifically, intensity histograms were created for each frame, representing each single nucleus recorded in the Ser5P and DNA channels. These histograms were globally fitted using a Gaussian distribution:

$$I^B = A_0 e^{-\frac{I^2}{2\sigma^2}}\,. \tag{5.5}$$

The fitting process was constrained to the first four intensity counts, which ensures that the primary signal contributions remain within an appropriate dynamic range. The mean background intensity $\langle I^B \rangle$ was then computed as 0.8σ based on the Gaussian fit. In the case of the Ser2P channel, a slightly different approach was taken. Since the fluorescence signal was fully bleached at the ending frames, the mean intensity I' was extracted from the last five frames in the 25-frame image stack, and this average value was used as $\langle I^B \rangle$ for background correction in the final analysis.

It is essential to consider only fluorescence photons to achieve accurate correction for photobleaching. To mitigate the impact of noise on the photobleaching correction and prevent it from biasing the bleaching factor, an intensity threshold was introduced that retains only

pixels clearly above the background level. Without this threshold, noise in later frames would inflate the calculated bleaching factor, leading to a spurious increase in measured cluster mean intensities over frame number. To identify an appropriate threshold, various levels (from 1.0σ to 3.0σ) were tested, and it was found that setting the threshold at 2.5σ effectively eliminated noise contributions while preserving genuine signal. The stability of the computed bleaching factor and the observed cluster mean intensities as a function of frame number verified this choice: a 2.5σ threshold sufficiently separates true signal from noise for the photobleaching adjustment. As a result, only fluorescence intensities I' greater than 2.5 standard deviations (or equivalently $I'' > 1.83\sigma$) were considered.

For a 3D image stack, photobleaching was corrected on a per-frame basis. It was assumed that, in the absence of photobleaching, the average fluorescence intensity across all frames k for a given nucleus, denoted $\langle I_k^0 \rangle$, remains constant and is equivalent to the mean fluorescence intensity of the first frame, $\langle I_1^0 \rangle$. For the first frame, $k = 1$, the scaling factor α_1 is considered to be unity, implying $\langle I_1'' \rangle = 1 \times \langle I_1^0 \rangle$. For any other frame k, the scaling factor α_k is calculated as:

$$\alpha_k = \frac{< I_k'' >}{< I_1'' >} . \tag{5.6}$$

The bleaching coefficient may be reliably computed just for frames when the fluorescence signal significantly exceeds the background noise, specifically in instances where the signal-to-noise ratio is determined using:

$$SNR = \frac{var(I'_k)}{var(I^B)} = \frac{var(I'_k)}{\sigma^2}. \tag{5.7}$$

is higher than 1.2 as a cut-off.

By including all aforementioned steps, the I^0 at each frame, as the "true" fluorescence signal can be expressed according to:

$$I_k^0 = \frac{1}{\alpha_k}(I'_k - \langle I^B \rangle) = I_k'' \frac{\langle I_1'' \rangle}{\langle I_k'' \rangle}. \tag{5.8}$$

To assess the intensity threshold for identifying voxels associated with Pol II Ser2P, Pol II Ser5P, or DNA structures, the previously applied image correction steps were followed. Initially, the intensity threshold $I^{c\prime}$ was defined as two standard deviations (2σ) of the Gaussian fit. Nevertheless, the cut-off intensity for I'' must be recalculated for each frame accordingly due to adjustments for bleaching correction applied to I'. This revised threshold is given by:

$$I_k^{c\prime\prime} = \frac{1}{\alpha_k}(2\sigma - I^B)\,. \tag{5.9}$$

where $I_k^{c\prime\prime}$ is the updated intensity cut-off for frame k.

5.3.5 Cluster Segmentation

Intensity-corrected images of the corresponding detection channel were used for cluster property extraction and segmentation. To extract nuclear segmentation masks in the Pol II Ser5P channel, the Otsu threshold was applied on extremely blurred (σ = 1.2 µm) images. Afterward, the bwconncomp MATLAB function was used to identify separated 3D objects of connected pixels within the respective nucleus mask and above the cut-off intensity.

As an input for this function, the connectivity criterion of 6 pixels, i.e., one neighboring pixel in all three dimensions from the central pixel, was selected to include as many voxels as possible at the edges of objects. Additionally, to prevent over-segmentation, the density-based spatial clustering of applications with noise (DBSCAN) algorithm [123] was used. DBSCAN helps fragmented and irregular aggregates to be represented as a low-solidity cluster. This method combines single detected objects that belong to the same structure, within a search radius of 0.2 µm, a distance that approximately fits the average radius of individual objects. Using the regionprop3 function in MATLAB, for every segmented object, the mean intensity, intensity-weighted center of mass, volume, and solidity were extracted. The mean intensity of a given cluster refers to the average intensity level of the pixels segmented within that cluster. Furthermore, it should be clarified that the solidity parameter establishes the ratio between the volume of the cluster and the volume of the convex hull that surrounds it. Based on the early Ser2P and Ser5P cluster size evaluation, periphery clusters, which identify those with centers inside the first one and three frames for the Ser2P and Ser5P channels, respectively, are categorized with distorted shapes. They were thus not included in the dataset for further investigation.

5.4 Investigation of RNA Pol II-mediated Transcription in Zebrafish Embryonic Cells

5.4.1 Zebrafish Embryos as an Excellent Model Organism

Since this study focuses on the relationship between animal physiology and transcription inhibitors as chemical compounds, zebrafish embryos serve as an excellent model system [124]. Because of the fact that it is not possible to conduct experiments on human patients due

to ethical and physical limitations, model organisms are used to investigate biological mechanisms that are shared by both humans and vertebrates [124]. Further, a number of advantages of this model are its small size, the ability to easily absorb chemicals, ease in observing it, and analogy in physiology to other vertebrates, including humans [124,125]. More than 80% of identified human disease genes are shared with zebrafish, and the actual number is more than 70% of the human genome that is shared with the same species [126]. Despite the great dissimilarities in physiology and metabolism, fish and mammals have, thus far, elicited similar responses to many of the chemical treatments examined [124].

5.4.2 Embedding of Control Steps in Different Cluster Architectures

As shown in Figure 5.1a, steps in the classic model of transcription regulation are arranged according to two crucial control points that are mediated by the cyclin-dependent kinases CDK7 and CDK9 [127–131]. Counted as the initial control point, the recruitment of Pol II via the promoter region of a gene phosphorylates the C-terminal domain (CTD) of Pol II at Serine 5 and Serine 7, immediately followed by transition into early elongation [132]. Pol II enters the promoter-proximal stop after transcription spans 20–60 nucleotides [131]. The concentration of transcription factors and coactivators at a gene's promoter region leads to phosphorylation of the negative elongation factors (NELF and DSIF) as well as Pol II CTD at Serine 2 [133]. This process serves as the second regulatory point [134,135]. By the phosphorylation of the negative elongation factors, productive elongation is allowed by the release of the paused Pol II. Notably, as illustrated in this figure, the great majority of promoter-associated and Ser5-phosphorylated Pol II is liberated from DNA even for genes undergoing high levels of transcriptional activity [136–138].

The regulation of gene expression in stem cells and embryonic cells reveals unique mechanisms that set them apart from the canonical control of transcription. Figure 5.1b indicates that, unlike the small, transient clusters of transcriptional machinery observed at gene promoters in typical cells (Type I), stem cells exhibit large, stable clusters primarily associated with super-enhancers, which are extensive genomic regions rich in transcription factor and coactivator binding sites [139–141]. These clusters are largely devoid of the elongation mark, serine 2 phosphorylation [139]. This distinct architecture enables robust transcriptional bursts that drive high expression levels of cell identity genes [142].

As found in this study, in line with previous publication [35], three distinct nano-architectures of Pol II Ser5P clusters can be distinguished: type I, the small and transient clusters typical in

canonical transcription (Figure 5.1c); type II, large, round, and droplet-like clusters that do not have proximal transcriptional activity (Figure 5.1c); and finally, type III, representing dispersed or unfolded clusters bearing actively expressed genes, commonly with genes located next to the edge of the cluster (Figure 5.1c). Underlying a complex regulatory framework necessary for pluripotency maintenance and cell fate decisions, this interaction between super enhancers, target genes, and liquid-like condensates of transcription machinery manifests these unique morphologies [143,144].

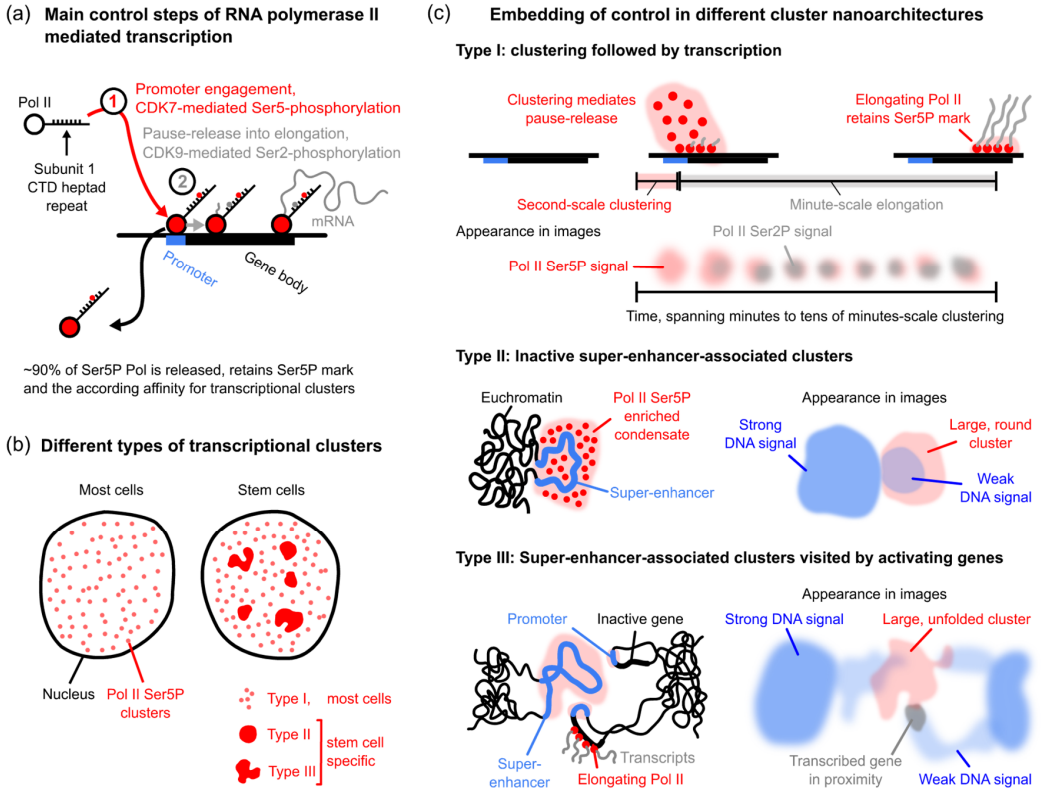

Figure 5.1: Schematic representation of RNA Pol II recruitment, pause release, and elongation in the context of macromolecular clusters. (a) Key regulatory stages in the transcription process initiated by RNA Pol II. **(b)** Depiction of Pol II Ser5P cluster patterns in both standard somatic cells and pluripotent stem cells, highlighting three morphologically distinct cluster forms. **(c)** Conceptual representations of nanoscale Pol II Ser5P cluster structures:
Type I: Rapidly forming, short-lived Pol II Ser5P clusters that facilitate transition from promoter pausing to elongation; subsequent transcription proceeds over several minutes and involves Ser2P-modified Pol II.
Type II: Spherical and stable Ser5P-enriched condensates linked to not fully active super-enhancers within relaxed chromatin, often visualized as bright DNA regions near dimmer DNA zones.
Type III: Clusters linked to active super-enhancers, serving as interaction hubs for elongating Pol II during active transcription. These clusters mostly appear dispersed and extended in structural imaging and are closely associated with ongoing gene activity. Taken from [173].

As can be seen in Figure 5.1c, Pol II Ser5P (red circles) accumulates into discrete clusters at the promoter, mediating the release of paused Pol II. As Pol II transitions into productive elongation, it retains the Ser5P modification but begins to acquire the Ser2P mark (gray). These elongating complexes spread along the gene body over minutes, indicating transcription in progress. As elongation proceeds, successive snapshots in fluorescence microscopy would show punctate red signals (Pol II Ser5P) forming at the promoter and gradually dispersing along the gene, accompanied by emerging gray signals (Pol II Ser2P).

In type II clusters (Figure 5.1c), Pol II Ser5P assembles into an enriched condensate (red) that colocalizes with the super-enhancer region (blue), yet it shows little evidence of productive transcription based on the literature [35]. Although these clusters arise within relatively open (euchromatic) chromatin, they appear to initiate transcription only weakly [35]. In fluorescence microscopy, Pol II Ser5P clusters present as relatively large, spherical foci enriched for initiating polymerase, while signals associated with elongating complexes are minimal.

In type III, the super-enhancer (blue) forms a larger, unfolded cluster in which nearby genes become mostly transcriptionally active (Figure 5.1c). In this scenario, reflecting active transcriptional processes, Pol II Ser5P (red) and transcripts (gray) are found next to the super-enhancer. During super-resolution imaging, these clusters appear large and less compact, with genes mostly sitting close to the cluster peripheries, showing a strong DNA signal from the enhancer region and a weaker DNA signal where chromatin is more open.

5.5 Results and Discussion

5.5.1 Multi-Color STEDD Imaging of Chromatin–Transcription Architecture

In this study, 3-color 3D-STEDD allowed visualization and quantification of the spatial distribution and morphological properties of chromatin, recruited Pol II, and transcribing Pol II at the nanoscale within prominent transcriptional clusters that typically occur in stem cells. Figure 5.2 shows the spatial organization of Pol II Ser5P, Pol II Ser2P, and DNA materials in a representative wild-type nucleus using single-channel and merged-channel representations in lateral (*XY*) and axial (*YZ*) directions. In addition to a widespread presence of smaller clusters, as can be seen in the Pol II Ser5P channel, recruited Pol II is observed to form numerous prominent clusters, which is consistent with previous studies [35,110,129,145]. Based on the single channel of Pol II Ser2P in Figure 5.2, it can be observed that they appear in smaller spots

with almost equal spatial extent. Furthermore, the merged channel between Pol II Ser5P and Ser2P shows that elongating Pol II aggregates are mostly placed at the margins or completely outside the recruited Pol II clusters, in line with previous observations [35]. As can be seen in the single channel, DNA material is almost uniformly distributed within the entire nucleus. Consistent with common models of the internal architecture of cell nuclei [35], it was observed that Pol II Ser5P and Ser2P clusters are not directly located in regions containing high local chromatin accumulation (Figure 5.2).

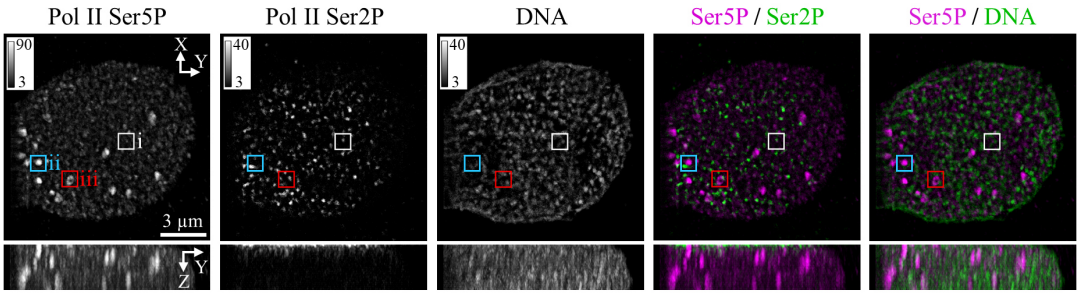

Figure 5.2: The nanoscale architecture of chromatin and RNA Pol II inside transcriptional clusters is revealed using 3D-STEDD fluorescence imaging of cell nuclei of wild-type zebrafish embryos (sphere stage). Maximum-intensity projections (MIPs) of *XY*- and *YZ*-plane images computed from volumetric (13.5 × 13.5 × 3.0 µm^3) image stacks are provided for a typical nucleus. Data were acquired in three different channels, Pol II Ser5P, Pol II Ser2P, and DNA (greyscale images); two-channel merges are shown in magenta and green. Colored squares indicate different Ser5P cluster types (white for type I, blue for type II, and red for type III). The same regions appear in the Pol II Ser2P and DNA channels for side-by-side comparison. Before interpolation for 3D rendering, we applied a small Gaussian filter (sigma = 0.5 pixels) in all three dimensions to smooth the raw image stack. Taken from [173].

In addition, Figure 5.3 shows a close-up view of the three separate areas marked in Figure 5.2 with squares that represent the Pol II Ser5P clusters of the apparent morphology types I–III. As was already described, type I clusters are more like small, well-confined spots that generally exhibit very low Pol II Ser2P signal. Larger with quite high compactness and mean intensity level in the Pol II Ser5P channel, type II clusters expose a low Pol II Ser2P signal. Type III clusters are also larger, less intense, and appear to be more unfolded in the Pol II Ser5P channel (Figure 5.3). Particularly complicated forms with a great morphological variation are shown by the unfolded type III clusters. This type of cluster shows a relatively high Pol II Ser2P signal in terms of intensity level and number of nearby aggregates. As shown in close-ups of the merged DNA and Pol II Ser5P channels for all cluster types, the recruited Pol II signal overlaps primarily with very low-intensity DNA areas (Figure 5.3).

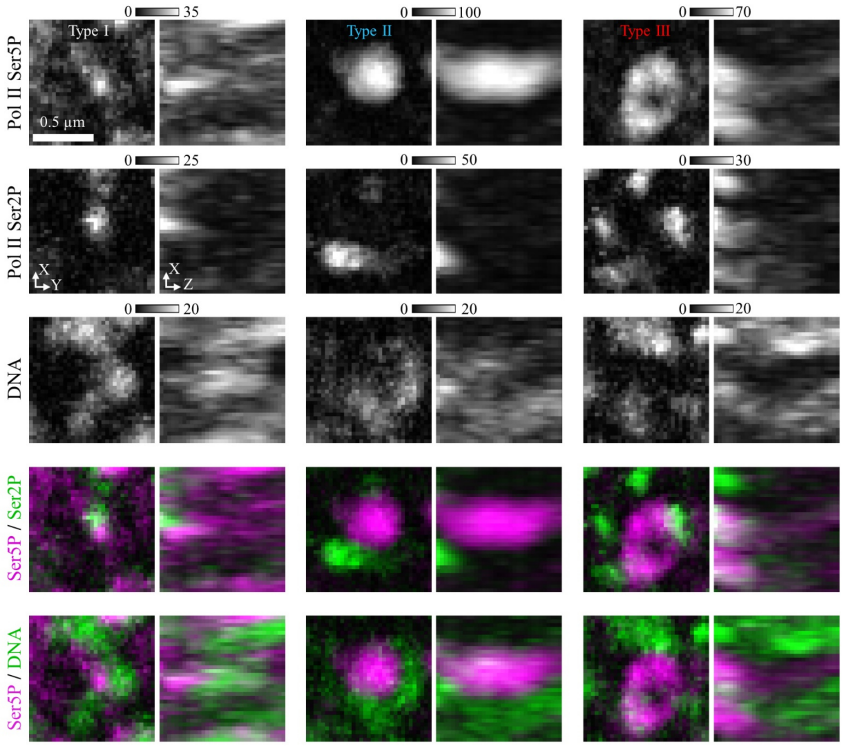

Figure 5.3: Close-up views of Pol II Ser5P clusters displaying morphology types I-III, along with corresponding regions in the Pol II Ser2P and DNA channels. Each zoomed-in panel represents a 1.0 × 1.0 × 1.0 µm³ volume, highlighting type I, type II, and type III Ser5P clusters in the left, middle, and right columns, respectively, as shown in Figure 5.2. Taken from [173].

As illustrated in Figure 5.1c, accompanying the development of Pol II Ser2P signals, repeated super-resolution imaging of the elongation process reveals punctate Pol II Ser5P signals that appear near the promoter and subsequently spread along the gene. This model was successfully observed using custom-built STEDD imaging to study RNA Pol II within transcriptional clusters at the nanoscale. Figure 5.4a provides an overview of the spatial organization of recruited Pol II, elongating Pol II, and DNA in another representative nucleus, with a volume of 13.50 × 13.50 × 1.0 µm^3. Consistent with the discussion presented in Figure 5.2, the observed characteristics in Figure 5.4a align well with established models describing the relationship between transcriptional clusters, chromatin domains, and nuclear organization in stem cells. A zoomed-in view of the white squares in this figure, highlighting four representative type I clusters that exhibit developing Pol II Ser2P signals along with the gradual spreading of Pol II Ser5P signals along the gene, is presented in Figure 5.4b. Close-up views in lateral and axial directions, labeled 1 through 4, are arranged to show a progressive increase in Pol II Ser2P signal levels. In the first close-up, the small, punctate type I Pol II Ser5P cluster at the center shows almost no detectable Ser2P signal, which is more apparent in the merged channel. In the second close-up, the Pol II Ser5P cluster begins to exhibit some Ser2P signal, appearing mostly

at the edge of the Ser5P cluster. By the third close-up, as clearly visible in the merged channel, the Ser2P signal level increases and is localized at the periphery of the Ser5P cluster. Finally, in the fourth close-up, the Ser2P signal level further increases and is located nearly, but entirely outside, the Ser5P cluster. These four representative type I Ser5P clusters illustrate how the Ser2P signal level changes during different stages of Ser5P activity along the gene body.

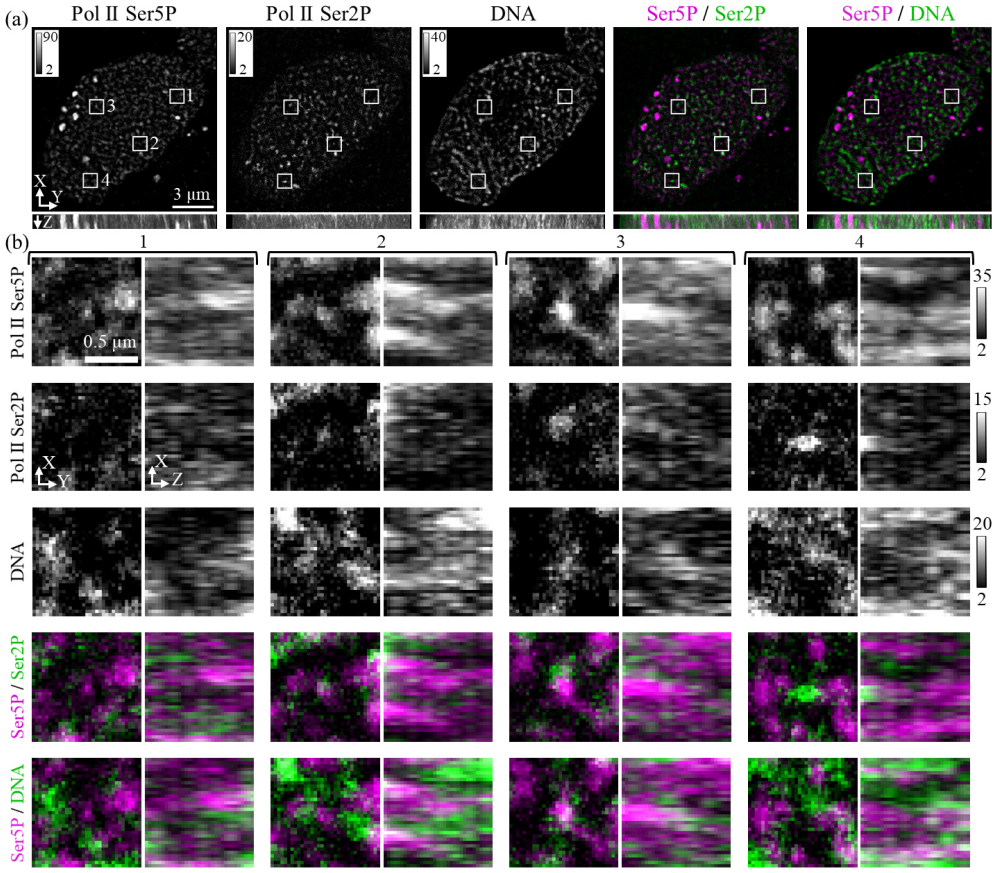

Figure 5.4: 3D-STEDD fluorescence images of a cell nucleus from wild-type zebrafish embryos at the sphere stage, providing nanoscale detail on how chromatin and RNA Pol II organize into transcriptional clusters. (a) A representative nucleus is depicted with maximum-intensity projections in both the *XY* and *yz* planes, derived from a volumetric stack measuring 13.5 × 13.5 × 1.0 µm³. Type I Ser5P clusters measured at four different time points are indicated by white boxes, with accompanying Pol II Ser2P and DNA views provided for comparison. **(b)** Four chosen volumes (1.0 × 1.0 × 1.0 µm³) are depicted in the enlarged form to show the structure of Ser5P clusters in greater detail. The choice of these four points is intended to highlight the changes in cluster structure that are emerging over time (as noted in Figure 5.1c). Point 1 features a relatively weak Ser5P cluster without evidence of transcription. Point 2 shows a complete overlap of Ser5P and Ser2P signals. At Point 3, Ser2P appears at the periphery of the Ser5P domain, and Point 4 illustrates Ser2P moving progressively outward from the cluster center. Taken from [173].

Furthermore, Figure 5.5 shows how type II (high solidity) and type III (low solidity) Pol II Ser5P clusters handle both chromatin (DNA) and Ser2P-labeled transcribed genes close to the cluster center of mass. In these maximum-intensity projections (1.5 × 1.5 × 0.5 µm³), Pol II Ser5P is shown in red, Pol II Ser2P in green, and DNA in blue. The type II cluster (top row) displays a more compact shape, which keeps much of the surrounding DNA and Ser2P foci at

the periphery regions. In contrast, the type III cluster (bottom row) exhibits a more unfolded shape with notable crevices. This less tightly packed arrangement lets transcribed genes and chromatin reach deeper into the weighted centroid of the cluster. These components, therefore, find the cores of the type III clusters more accessible, implying a structural foundation for how active transcription sites and surrounding chromatin can invade into and interact with large Pol II Ser5P clusters.

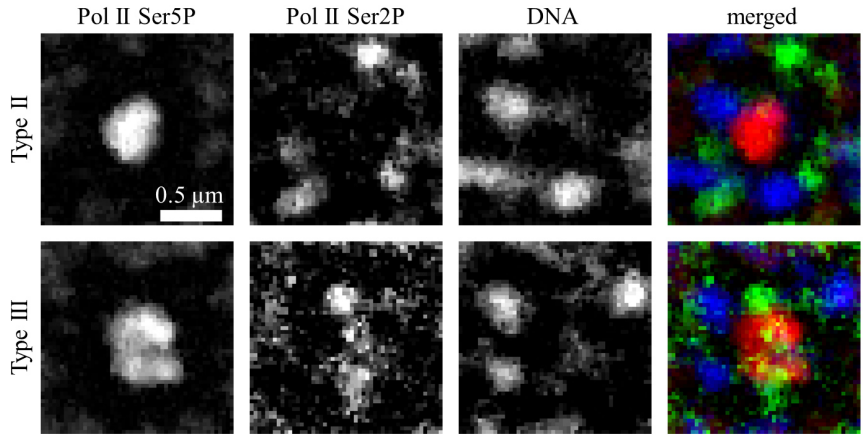

Figure 5.5: Demonstrated here is how chromatin and Ser2P-labeled transcribed genes are positioned relative to the center of mass within type II and type III Pol II Ser5P clusters. Close-up views of 1.5 × 1.5 × 0.5 µm³ regions are visualized through maximum intensity projections. The merged images represent Ser5P in red, Ser2P in green, and DNA in blue. Taken from [173].

5.5.2 Classification of Pol II Ser5P Clusters

As was observed in Figure 5.2 to Figure 5.4, Pol II Ser5P clusters in zebrafish embryonic cells display a broad distribution in a nucleus across various characteristics, including volume, mean intensity, and compactness level (solidity). After the feature extraction of the segmented clusters, as described in the materials and methods section, for detailed examination of the effects of different transcription inhibitors on the nano-architecture of the transcriptional clusters, they should be categorized into sub-groups (type I, II, and III) based on their features. In a previous study, only based on a single morphological characteristic, solidity, these clusters were categorized into type II (rounded) and type III (unfolded) [35]. Given the complex nature and strong variation of the cluster characteristics, classification into subgroups can only be precisely accomplished by plotting the inherent relationships between cluster characteristics such as volume, solidity, and mean intensity (Figure 5.6). In this context, classification is similar to solving a multi-dimensional puzzle. Figure 5.6a plots the logarithm of solidity (S) vs. the normalized volume (V/V_0) of segmented clusters. Here, V_0 stands for the STED microscopy PSF volume, which was equal to 0.003 µm^3. This relationship was fitted using the

power-law function ($y = ax^k$), which catches the main mode of this distribution. Fitting this 2D plot with a power-law function suggests that as cluster size increases, the structural organization and compactness follow predictable, self-similar patterns, indicating complex molecular interactions and spatial constraints within the clusters. Furthermore, power law fitting assumes that both molecular interactions and spatial constraints may affect how the solidity of a cluster changes as the volume varies, which represents the inherent complexity of the system. As shown using vertical dashed lines in Figure 5.6a, it should be noted that to exclude tiny clusters (V_{low} < 0.06 µm^3) and agglomerations of several clusters (V_{up} > 0.6 µm^3), a lower and upper limit was set. As can be comprehended based on the fit parameter added to the panel, this panel reveals a negative slope in the relation, indicating a decrease in the solidity of most clusters as the cluster volume increases. However, a fraction of clusters, despite having a large volume, also display a high solidity level. Furthermore, Figure 5.6b plots the association between the logarithm of the clusters' mean intensity ($\tilde{\imath}$) and their relative volume. This figure indicates a positive slope, specifying that the mean intensity increases with cluster size. The data also suggests the presence of a number of large clusters with exceptionally high mean intensity values. Moreover, panels (a) and (b) in this figure demonstrate the extremely smooth transition between different cluster types, making it only possible to classify clusters into subgroups by examining the aforementioned relationships simultaneously.

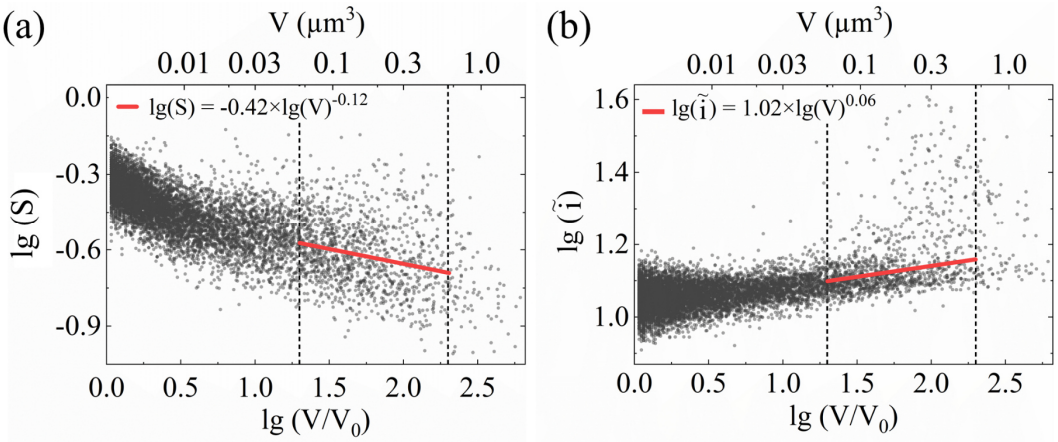

Figure 5.6: 2D plots showing the relationships between volume, solidity, and mean intensity of Pol II Ser5P clusters. (a) This panel presents a scatter plot of cluster solidity (S) versus the ratio of cluster volume to a STED point-spread-function volume (V/V_0), both plotted on a log-log scale. The reference volume, V_0, corresponds to 0.003 µm³. Dashed lines indicate the lower (V_{low}< 0.06 µm³) and upper (V_{up} > 0.6 µm³) volume thresholds applied to exclude both very tiny clusters and agglomeration of multiple aggregates. The solid orange line shows a power-law fit to the median solidity values within the selected volume range, analyzed in log-log form. Gray dots represent all observed Pol II Ser5P clusters. **(b)** Similarly, this scatter plot illustrates the mean intensity ($\tilde{\imath}$) of clusters as a function of normalized volume. Taken from [173].

The next step in solving this puzzle and categorizing clusters into subgroups is presented in Figure 5.7. This 2D plot illustrates the relationship between the rescaled solidity ($\frac{S}{a_1 \times V^{b_1}}$) and mean intensity ($\frac{\tilde{\imath}}{a_2 \times V^{b_2}}$) of the clusters. Rescaling was performed using the fit parameters extracted from the plots in Figure 5.7(a) and (b). To distinguish large clusters as type II or type III based on this scatter plot, a threshold must be defined. To determine this boundary, the histogram count distributions of the rescaled solidity ($\frac{S}{a_1 \times V^{b_1}}$) and mean intensity ($\frac{\tilde{\imath}}{a_2 \times V^{b_2}}$) were overlaid and fitted using Gaussian functions. Using a conservative boundary (mean ± 3σ of Gaussian distributions), an ellipsoid was defined as a criterion to distinguish different subpopulations (Figure 5.7). Type II clusters, in simpler terms, are super clusters with extensive volume, high solidity, and mean intensity values that fall outside of the ellipsoid determined with blue squares. However, type III clusters include large volumetric clusters that are more unfolded (less compact) and exhibit a moderate mean intensity level determined with red triangles. As observed in the control sample, the fraction of type II clusters relative to the total of type II and III clusters is 0.10. In summary, this classification procedure accurately assigns large Pol II clusters into two categories: compact morphology with a high Ser5P signal level (type II) or unfolded morphology with a moderate Ser5P signal level (type III). These allocations are made based on the connection between the major cluster features and are unaffected by the artifact-driven impact of solidity scaling on cluster volume.

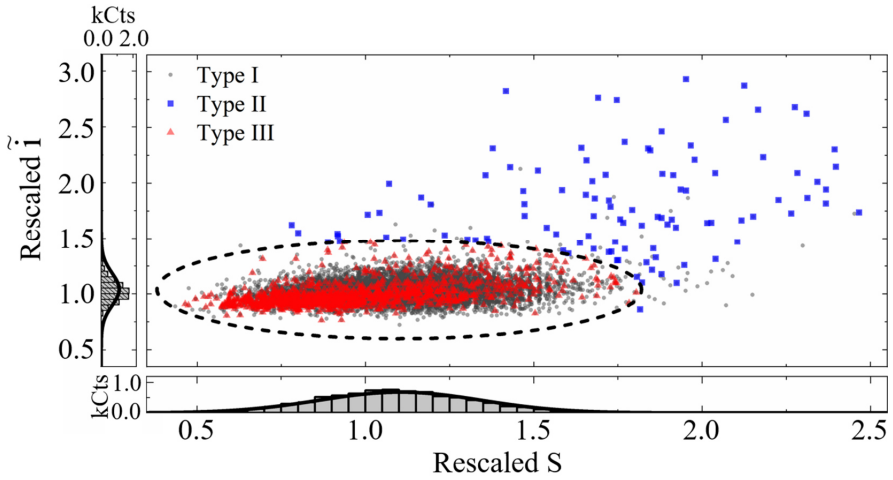

Figure 5.7: Relationship between the rescaled mean intensity ($\frac{\tilde{\imath}}{a_2 \times V^{b_2}}$) and solidity ($\frac{S}{a_1 \times V^{b_1}}$) as a metric for classification of Pol II Ser5P clusters. The central scatter plot highlights how these adjusted metrics of cluster shape and brightness correlate with each other, while histograms displayed along the left and bottom edges illustrate the individual distributions of the two parameters. Each histogram is fitted with a Gaussian function (solid lines), and the resulting fit parameters define an ellipse on the scatter plot, using the respective means plus three standard deviations. Blue data points represent type II Ser5P clusters, and red data points denote type III Ser5P clusters. Taken from [173].

5.5.3 Influence of Control Steps on the Occurrence, Morphology, and Intensity of Condensates

Considering the improved resolution and 3D-imaging capabilities of the home-built STEDD nanoscopy approach, this study aimed to assess how the nano-architecture of large transcriptional clusters changes upon perturbation of different steps in the control of transcription. To acutely and selectively perturb specific steps of transcriptional control, we employed different chemical perturbations and assessed their effect on the nucleus-wide organization of chromatin and Pol II. It should be noted that to prevent alterations to transcription control via gene regulatory responses, perturbation treatment duration was limited to 30 minutes or less, and directly followed by fixation. As shown in Figure 5.1, the transcription site serves as the control for studying the mechanisms of various transcription inhibitors. These inhibitors, JQ1, Hexanediol (Hex), Triptolide (TL), and Flavopiridol (FP), affect transcriptional activity at different stages of RNA Pol II activity, altering the phosphorylation states of Pol II Ser5P and Pol II Ser2P. Figure 5.8a highlights the distinct pathways through which each inhibitor disrupts transcriptional cluster nano-architecture in zebrafish embryonic cells.

As can be seen in the schematic of the control case in Figure 5.8a, the super-enhancers have been earlier described as platforms that enable the condensation of Pol II as a transcription factor [146]. BET proteins, namely the bromodomain and extra-terminal domain, have emerged as potential therapeutic targets for cancer and immune disorders [147,148]. In most active enhancers and promoters, the simultaneous presence of H4K5acK8ac (di-acetylation at K5 and K8 of histone H4), H3K27ac, and BRD2 was observed [147,149,150]. In other words, JQ1 impairs the proper function of super-enhancers as condensation surfaces, a process that is essential for the recruitment of both transcription factors and other machinery to chromatin. In line with reducing the stickiness of the enhancer regions via inhibition of BRD2 and BRD4, Pol II Ser5P clusters are less intense, as shown qualitatively in Figure 5.8b and quantitatively in Figure 5.9. The lower occurrence of large clusters can also be seen based on the quantitative analysis presented in Figure 5.8c, which plots the relationship between solidity and normalized volume. In this panel, the classification of clusters was performed as detailed in the previous section. Based on this analysis, the fractions of type II and type III combined, relative to the all cluster, are 0.12 after JQ1 treatment and 0.14 for the control. Furthermore, this panel examines the proportion of type II clusters, f_{II}, relative to the total number of type II and type III clusters. Upon JQ1 treatment, the fraction of type II clusters in the cells increased to 0.16, compared to

0.10 in the control sample. This finding is consistent with the observed disruption of transcriptional activation: global elongation levels decreased, and Pol II clusters adopted a more rounded shape, suggestive of reduced transcription activity near the Pol II clusters (Figure 5.8c).

In phase separation experiments in a variety of domains, the alcohol 1,6-hexanediol is frequently used as a control to dissolve liquid-liquid phase separation (LLPS) assemblies [151]. As illustrated in Figure 5.8a, in this study, cells were treated with low concentrations of hexanediol for 3 min. The aliphatic alcohol 1,6-hexanediol interferes with weak hydrophobic interactions and is often used to dissolve protein condensates in vitro and in cells, illustrating the reversible character of phase separations [151–153]. Pol II clusters appeared more rounded and less intense than the control condition, as expected due to the loss of liquid-phase properties and the desolvation of the peripheral fuzzy component (Figure 5.8b and Figure 5.9). Based on the further quantitative analysis provided in panel (c), the proportion of combined type II and type III, relative to all clusters, is 0.10 after Hex treatment, which originates from the desolvation of LLPS assemblies. In addition, similar to the JQ1 treatment, upon Hex treatment, a shift towards more solid clusters is observed, which is in line with a loss of interaction with transcribed genes (Figure 5.8c).

A heterodimeric protein complex called transcription factor IIH (TFIIH) is essential for nucleotide excision DNA repair and transcription initiation by RNA Pol II [154]. To block transcription initiation, the small molecule triptolide, a helicase activity inhibitor of XPB/TFIIH, can be used [155]. As presented in Figure 5.8a, since the initiation is hindered using TL, this inhibitor results in reduced transcriptional elongation, besides reduced amounts of dispersible Pol II Ser5P. As shown in Figure 5.8b, a qualitative comparison between the control and TL-treated samples, based on representative nuclei, reveals a reduction in cluster intensity levels (Figure 5.9) and a more unfolded appearance, consistent with the inhibition of transcription initiation. Moreover, as the percentage of type II clusters (f_{II}) is lowered to 0.07, categorization analysis of clusters guarantees a significant Pol II clusters shift towards a less compact shape. This finding shows a decrease in the factors that drive compaction of Pol II Ser5P clusters (Figure 5.8c).

Competing with adenosine triphosphate (ATP) for the active site of each kinase, Flavopiridol effectively inhibits cyclin-dependent kinases (CDKs) [156]. Recent discoveries have revealed that FP plays a crucial role in reducing transcription by targeting CDK9 [157,158] and CDK7

[159]. These two kinases, CDK7 and CDK9, are directly responsible for the phosphorylation of the C-terminal domain (CTD) of RNA Pol II's largest subunit in the initiation and pause-release stages of transcription, respectively [35,156]. In other words, by blocking CDK7, FP reduces the phosphorylation of Ser5 in the CTD, a hallmark of early elongation. Similarly, inhibiting CDK9 prevents the subsequent transition from Ser5P to Ser2P, thereby further hindering productive elongation. As schematically drawn in Figure 5.8a, treatment upon FP leads to polymerases that remain in the Ser5-phosphorylated (initiation/early-elongation) state and accumulate near the promoter. Over time, the global pool of Ser5-phosphorylated polymerases diminishes because fewer Pol II molecules are recruited into (and maintained in) the Ser5P state (Figure 5.8b and Figure 5.9). In line with previous observation [35], quantitative investigation in panel (c) of this figure shows a reduction in the occurrence of large Pol II clusters. Additionally, f_{II} reached 0.13 upon FP treatment, which indicates that the large Pol II clusters exhibit a more solid morphology (Figure 5.8b and c).

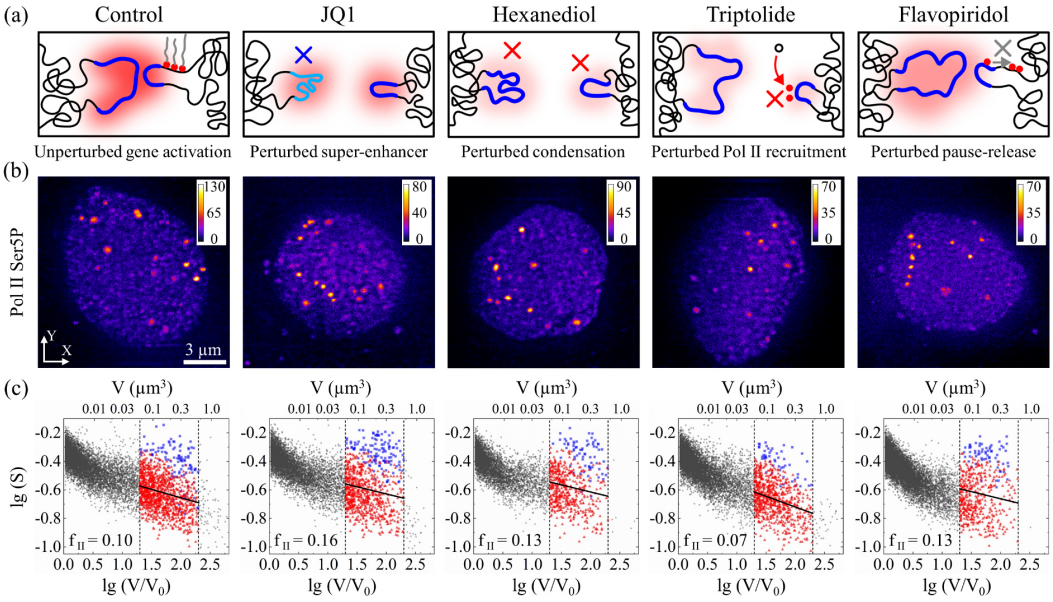

Figure 5.8: Impact of inhibitor treatment on the structure of RNA Pol II Ser5P clusters. (a) Schematic representations showing how clusters of RNA Pol II Ser5P and their associated condensates act under control conditions and when further treated with a range of inhibitors (JQ1, hexanediol, triptolide, and flavopiridol). Recruited and non-recruited Pol II are denoted by red closed and grey open circles, respectively. Grey tails represent RNA, while crosses represent the inhibitors' areas of action. (b) Maximum-intensity projection images from volumetric image stacks (13.5 × 13.5 × 3.0 µm³) of untreated (control) cells or cells exposed to four inhibitors. All images share the same contrast scale; the 3 µm scale bar applies to every panel. (c) Double-log scatter plots show the relationship between cluster solidity (S) and normalized volume V/V_0, following the approach used in Figure 5.5a. Within the vertical dashed lines, blue and red points mark type II and type III Pol II Ser5P clusters, respectively. The fraction of type II clusters (f_{II}) within this volume range is indicated on each plot. Grey symbols represent clusters that fall outside this range, encompassing both smaller type I clusters and larger merged clusters. The combined proportion of types II and III among all clusters is 0.14 for the control, 0.12 under JQ1 treatment, 0.10 with hexanediol, 0.09 with triptolide, and 0.05 with flavopiridol. Taken from [173].

Furthermore, treatment of embryos with the specified inhibitors resulted in a significant decrease in the normalized mean intensity of RNA Pol II Ser5P clusters, as shown in Figure 5.9, compared to the untreated controls. Each adjusted against the median intensity value in control embryos (dashed line at 1.0), the box plots provide an insight into the effects of different transcription inhibitors on three distinct categories of transcriptional clusters: type II, type III, and a combination of both types. Based on two-tailed permutation testing, treatments upon JQ1, Hex, TL, and FP caused a statistically significant reduction in Pol II Ser5P signal level across the three cluster categories. As was already discussed, JQ1 is a BET bromodomain inhibitor, which prevents BET-family proteins from binding to acetylated histones. This block can impair essential transcription cofactor assembly at promoters, resulting in reduced Pol II recruitment and Ser5 phosphorylation. Hex may generally interfere with the development of the pre-initiation complex, therefore impairing Pol II's capacity for effective transition into active transcription. By disrupting early transcriptional checkpoints, it lowers the production of Ser5P. TL is known to inhibit the XPB helicase activity within the TFIIH complex. TFIIH not only unwinds DNA at the promoter but also houses the CDK7 kinase responsible for phosphorylating Pol II at Ser5. Inhibiting TFIIH function thus directly curtails Pol II Ser5 phosphorylation and cluster formation. FP inhibits CDK7 and specifically CDK9, a component of positive transcription elongation factor b (P-TEFb). Besides the effect of CDK7 inhibition on the mean intensity of Pol II Ser5P clusters, CDK9 inhibition also disrupts the overall stability of transcription complexes and can feed back on early phosphorylation events (including Ser5) by creating a less permissive environment for Pol II progression from initiation into elongation. Briefly, these observations show that suppression of transcription-related pathways notably reduces the generation or maintenance of Pol II Ser5P clusters in developing embryos. Since Ser5 phosphorylation usually corresponds with the transition of Pol II from pre-initiation to promoter-proximal pausing and the early stages of elongation, the uniform reduction in Pol II Ser5P intensity across these three categories of clusters suggests that the inhibitors above may act through overlapping mechanisms that generally disrupt transcription initiation or early elongation.

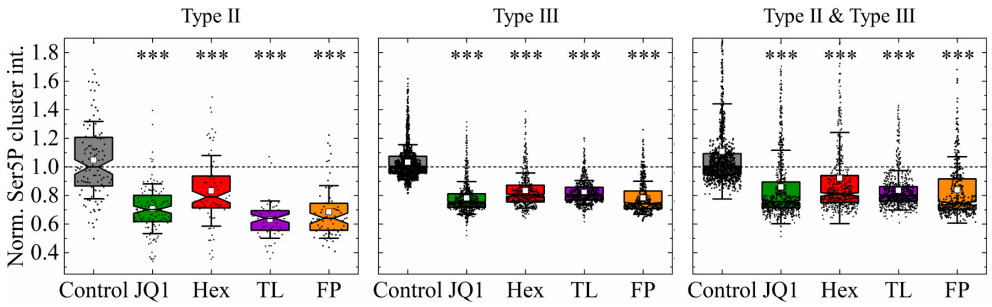

Figure 5.9: Normalized mean intensity of Pol II Ser5P clusters in Type II, Type III, and combined categories following inhibitor treatments. Each box plot is normalized to the median intensity in untreated controls (dashed line), and asterisk mark statistically significant reductions (*** for P-values < 0.001) based on two-tailed permutation tests compared to control. Taken from [173].

The structural integrity and stability of Pol II Ser5P aggregates are assessed by measuring and comparing the solidity levels of clusters in treated samples with transcription inhibitors to those in control samples. To pinpoint the effects of chemical perturbations on cluster shape, the solidity levels of treated cells were compared to control samples for each subgroup, namely type II and type III.

With JQ1, some additional Ser5P polymerases (stuck in early elongation or pausing) may accumulate in promoter-proximal regions and can increase local Ser5P density. As shown in Figure 5.10a, type II clusters within treated cells upon this inhibitor exhibit higher solidity levels, while clusters within the type III subgroup do not show any significant morphological alteration compared to the control sample. Furthermore, changes in the clusters' morphology upon chemical perturbations are shown in Figure 5.10b. For this qualitative comparison, a cluster from each subgroup (type II or type III) under different conditions (wild-type or treated) was selected, with a solidity close to the mean of the distribution shown in panel (a), which serves as a fair representative of that distribution. In this panel, blue points indicate the cluster pixels, and the convex hull is shown as a cyan area bounded by a black outline. Greater solidity is observed when these blue points more densely occupy the convex hull, while a thinner distribution within the hull indicates lower solidity. Qualitatively, it can be observed that the representative type II cluster in the JQ1 condition has a denser concentration of cluster pixels within the hull (less free cyan space), compared to the control sample. This suggests higher solidity in the JQ1 condition compared to the control cluster.

Based on this study, inhibition of LLPS assemblies upon Hex treatment led to type II and III clusters with higher solidity levels. As was discussed, this originates from the desolvation of the peripheral fuzzy component, which leaves an even more core cluster (Figure 5.10).

Hindering initiation upon TL as an activity inhibitor of XPB/TFIIH resulted in a more pronounced unfolding specifically of the type III clusters (Figure 5.10). The morphological alteration via using TL is more pronounced in type III since these clusters are large, dynamic assemblies that depend on continuous initiation, factor cycling, and chromatin reorganization. When this cycle is interrupted by Triptolide, incomplete transcription complexes or improperly reset chromatin states accumulate and are thereby even more unfolded.

Furthermore, blocking pause-release leads to opposing effects, where rounded (type II) clusters became more rounded, and unfolded (type III) clusters became more unfolded (Figure 5.10). This observation happens because both types are collecting more Ser5P polymerases (since FP blocks their transition to Ser2P). Type II clusters have a smaller, more rigid core architecture. Accumulating more stalled Pol II essentially adds mass to a relatively compact, anchored scaffold, making it appear more solid. Type III clusters rely on larger, more multi-factor complexes or looping architectures. Accumulating more Pol II and cofactors (e.g., pausing factors, splicing factors, additional regulatory proteins) can make these clusters expand, fan out, or become even more unfolded.

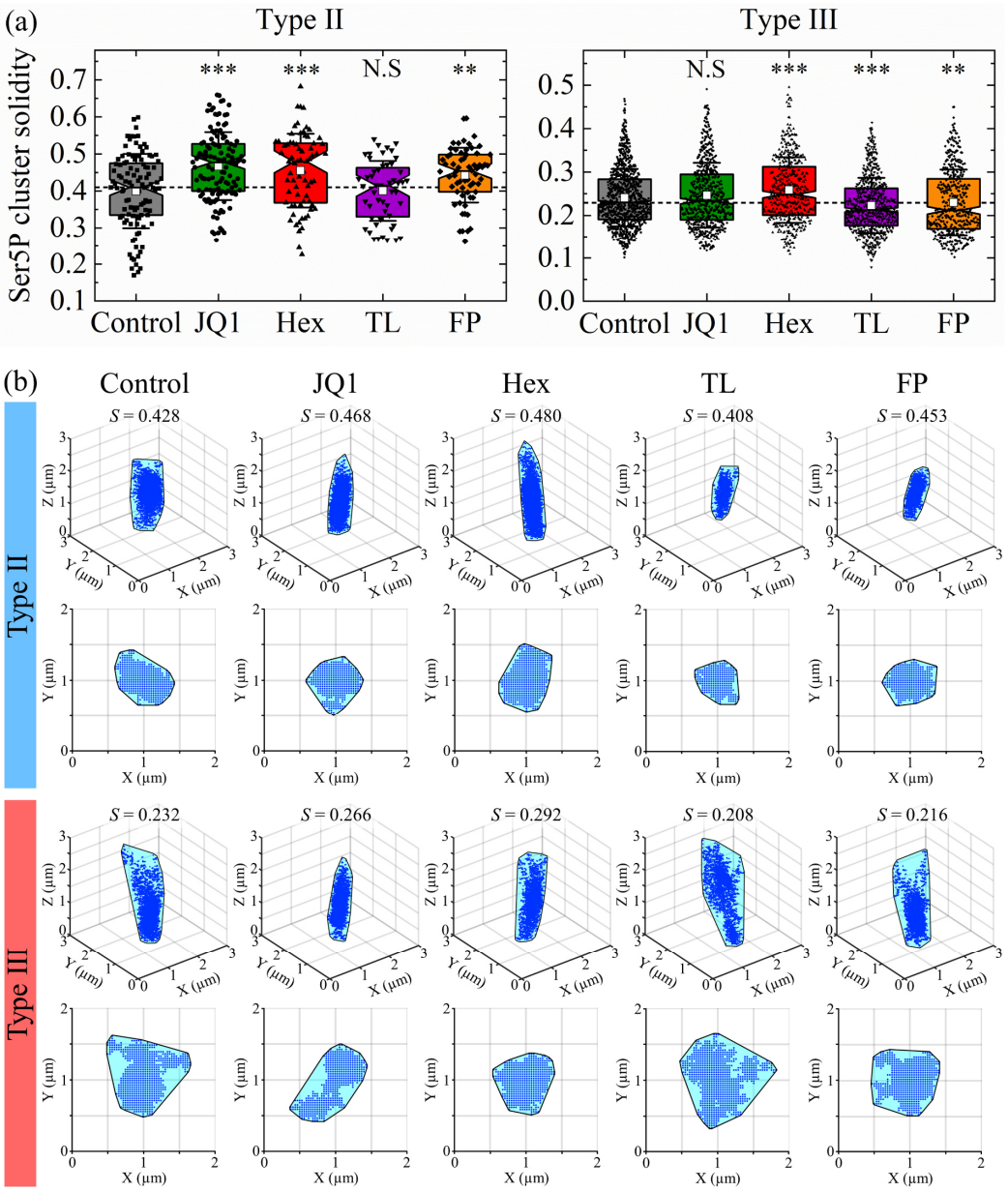

Figure 5.10: Effect of inhibitor treatment on solidity of Pol II Ser5P clusters. **(a)** Notched box plots of the solidity of type II and type III Pol II Ser5P clusters in both control and inhibitor-treated conditions. Notches indicate 95% confidence intervals around the median. The dashed line indicates the median value in the control sample. Significance levels (*, **, ***) correspond to $p < 0.05$, 0.01, and 0.001, respectively, by a two-tailed permutation test between each treatment and control. "N.S." indicates no statistically significant difference. The total numbers of type II clusters examined were 107 (control), 125 (JQ1), 71 (Hex), 52 (TL), and 64 (FP), and for type III clusters were 1037 (control), 681 (JQ1), 476 (Hex), 702 (TL), and 432 (FP). **(b)** Visualization of cluster solidity under varying conditions, as represented by binary maximum-intensity projections. Blue spheres represent the voxels making up each cluster, and the convex hull by the enclosing cyan area, the border in black. The solidity parameter (S) is represented as a ratio of the cluster volume and the convex hull volume. Taken from [173].

5.5.4 Gene Expression Regulation Through Transcriptional Condensate-Mediated Chromatin Organization

The ability of transcriptional condensates to modulate chromatin accessibility is necessary for gene regulation [35,160–163]. Studying chromatin partitioning processes and how transcription inhibitors affect them can provide additional understanding of gene regulation strategies. Figure 5.11 quantifies and visualizes the effects of transcription inhibitors on the spatial organization of transcriptional clusters, actively transcribed genes, and the neighboring bulk chromatin. This figure examines how chromatin is positioned relative to Pol II Ser5P and Pol II Ser2P clusters. Histograms in panels (a) and (b) illustrate this relationship by showing the average DNA intensity per cluster. The mean DNA pixel intensity overlapping each segmented cluster was calculated. Then, the resulting distributions were plotted as histograms to visualize the spatial relationship between chromatin and transcriptional clusters. It should be noted that to account for any probable labeling efficiency differences between nuclei, the intensity of all DNA pixels within each nucleus was normalized to the mean intensity value of that nucleus before further calculation. Based on this analysis, consistent with observations in Figure 5.2 to Figure 5.4 and the well-established models in stem cells, it can be observed that both Pol II Ser5P and Ser2P aggregates are lacking DNA relative to the nucleus-wide distribution of DNA intensities (Figure 5.11a and 5.9b). As can be seen, the maxima of histogram distributions, both in control and treated conditions, are smaller than the gray dashed line at 1.0, which shows the mean intensity of all DNA pixels within nuclei in each specific condition as a reference. The mean values of the distributions in Figure 5.11a are 0.92, 0.68, 0.86, 0.89, and 0.81 for the control, JQ1, Hex, TL, and FP conditions, respectively, all of which are lower than the ungated mean DNA intensity. Similarly, the mean values of the distributions in Figure 5.10b are 0.69, 0.53, 0.77, 0.58, and 0.56 for the same conditions, indicating that Ser2P foci are located in regions with low chromatin density. The comparison of DNA placement relative to Ser5P and Ser2P aggregates suggests that transcribed genes are positioned in less compact chromatin regions compared to Ser5P aggregates.

Furthermore, Figure 5.11 shows the influence of transcription inhibitors on the overlap between chromatin and Pol II clusters. A concise way to read these plots is that each inhibitor shifts where Pol II clusters tend to reside relative to chromatin density, and that effect depends on the step-in transcription that the inhibitor targets. In each histogram, a leftward shift (negative difference in mean DNA intensity) indicates that Pol II clusters are found in relatively less

dense chromatin, whereas a rightward shift (positive difference) indicates localization to denser chromatin.

Using JQ1, when BRD4-mediated interactions are blocked, the normal stabilization of transcription complexes at enhancer or promoter regions is disrupted. Figure 5.11a and b show that both Ser5P and Ser2P clusters end up more in lower-density (less compact) regions of chromatin (leftward shift). This suggests that under normal conditions, BRD4 might help Pol II remain in or be recruited to more compact or specialized compartments. In other words, because many highly active genes rely on BRD4, the global transcription level can decrease, and the remaining Pol II clusters are found in somewhat more open regions of the nucleus. Furthermore, upon treatment with the JQ1 inhibitor, the magenta Ser5P or Ser2P clusters in Figure 5.11c appear slightly smaller or shrunken and are often located in more open (darker green) regions, which is consistent with the quantitative analysis.

Using Hex, by disrupting LLPS, Pol II clusters, or transcription factories, may become less stable. The data suggest modest (though sometimes significant) movement of Ser5P clusters toward less-dense chromatin (Figure 5.11a) and a nonsignificant tendency of Ser2P in the opposite direction (Figure 5.11b). Because 1,6-hexanediol acts broadly on weak hydrophobic interactions, its effect on Pol II distribution is less specific than targeted kinase or bromodomain inhibitors, hence the smaller net shift. Based on qualitative observation, it can also be seen that the overall difference in where the clusters lie relative to the green DNA signal is comparatively modest (Figure 5.11c).

Furthermore, as was discussed, Triptolide inhibits the TFIIH complex, and without efficient promoter clearance, new Pol II complexes cannot start elongation. The figure shows little change in Ser5P overlap (N.S.), possibly reflecting that once Pol II is already engaged or paused at the promoter with Ser5 phosphorylation, it is not drastically re-localized even if the new initiation is blocked (Figure 5.11a). Moreover, Figure 5.11b illustrates a marked shift to lower-density chromatin, which implies that as fewer new polymerases transition from initiation to productive elongation, existing elongating Pol II might redistribute away from dense chromatin or fail to be maintained in denser regions. Based on the qualitative observation provided in Figure 5.11c, the TL-treated sample does not look drastically different from the control, in line with the non-significant change we saw in the histograms. In the case of Ser2P images, there is a more noticeable disruption, with the foci either more scattered or less tightly

juxtaposed to bright DNA areas. That reflects the clearer leftward shift in Ser2P density we measured (Figure 5.11c).

Lastly, Flavopiridol impedes transcription elongation, leading to the accumulation of Pol II in a paused or aborted state. The strong shift toward lower-density chromatin for both Ser5P and Ser2P suggests that, once elongation is inhibited, Pol II clusters no longer move into or remain in higher-density chromatin regions (often associated with actively transcribed genes). Instead, they might accumulate or stall in more open regions or near promoters (Figure 5.11a and 5.9b). Based on close-up views, it can be seen that clusters sometimes appear large but more punctate and sit in relatively open areas (dimmer green). It can be observed that the magenta foci often ring or avoid denser DNA patches (Figure 5.11c). This corresponds to the pronounced shift away from compact chromatin that Flavopiridol caused for both Ser5P and Ser2P.

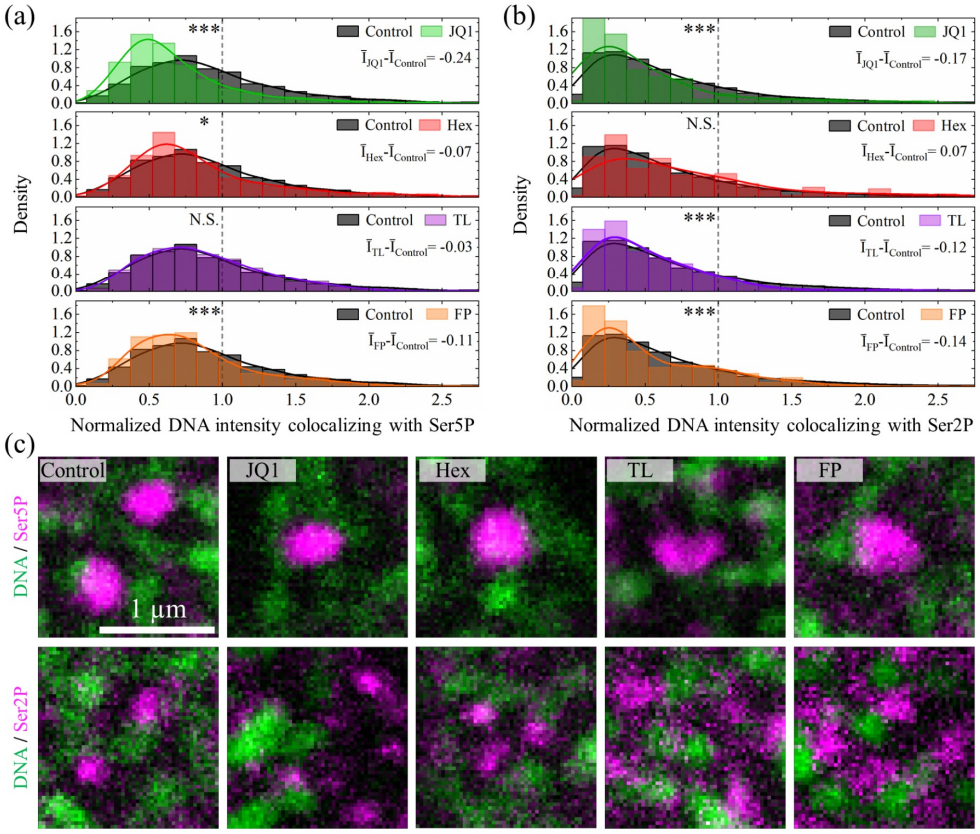

Figure 5.11: Influence of transcription inhibitors on the three-dimensional organization of transcriptional clusters, actively transcribed genes, and surrounding bulk chromatin. (a) With solid lines denoting kernel-smoothed fits for simpler distribution comparison, histograms show the average DNA intensity per cluster for Pol II Ser5P and Pol II Ser2P under the effect of various transcription inhibitors. The quantity $\bar{I}_{treatment} - \bar{I}_{control}$ shows how each treatment's mean intensity differs from that of the control. The gray dashed line at 1.0 represents the mean intensity of all DNA pixels in the nucleus (ungated) for each treatment, serving as a reference point. **(b)** Representative maximum-intensity projections, each covering a depth of 1 µm, are presented for a qualitative comparison between control and inhibitor-treated samples. Images are shown using the same contrast settings to allow direct visual evaluation of the changes in the spatial organization of transcriptional clusters, transcribed genes, and bulk chromatin. Taken from [173].

To better understand how chromatin is spatially arranged around large Ser5-phosphorylated RNA Polymerase II condensates, the radial DNA distribution relative to the weighted centers of both round (type II) and unfolded (type III) Ser5P clusters under normal and drug-treated conditions was analyzed (see Figure 5.12). To focus on clusters within a defined size range and to exclude rare and complex ones, the analysis was restricted to those with volumes below 0.2 μm^3.

For each radial bin, defined by edges at [0, 0.1, 0.2, 0.3, 0.4, 0.5, 0.6, 0.8, 1.0, 1.2, 1.5, 1.8] µm, concentric shells containing only voxels that fell within both the radial range and the nuclear mask were constructed, thereby limiting the analysis to nuclear regions. The density of DNA within each shell was determined by counting DNA-positive voxels (intensity > 0), denoted as n_{V_i}, and normalizing this by both the volume of the shell (V_i) and a reference nuclear density (D_{Ref}). This reference density was calculated as the total number of DNA-positive voxels in the entire nucleus divided by the nuclear volume. The resulting unitless normalized value, $(n_{V_i}) \,/\, (V_i \times D_{Ref})$, represents relative local chromatin concentration: a value of 1 indicates parity with the nuclear average, while deviations signal local depletion or enrichment.

This approach revealed that DNA is largely absent from the core of large Ser5P condensates and instead forms a concentrated shell around them. In untreated cells (Figure 5.12, Control), the normalized DNA signal at the center of both type II and type III clusters was significantly below average. The signal increased sharply within approximately 300–400 nm of the cluster center, peaking in a narrow zone before leveling off near the nuclear mean (≈1.0) at distances greater than 0.5 µm. These findings indicate a distinct two-zone architecture around Ser5P condensates: a chromatin-depleted interior and a sharply defined shell enriched in DNA. The similar DNA exclusion pattern observed for both morphologies suggests that chromatin exclusion is a shared characteristic of large Ser5P assemblies, independent of their structural form or transcriptional activity.

Moreover, columns 2–5 in Figure 5.12a show how different transcription inhibitors (JQ1, Hex, TL, FP) alter these spatial DNA density profiles. JQ1 is a BET bromodomain inhibitor that disrupts the binding of transcriptional coactivators at acetylated histones. It can be observed that treatment with the BET inhibitor JQ1 did not abolish the DNA shell, though its intensity was modestly reduced. Additionally, DNA accumulation around type II clusters was displaced outward, indicating a shift in radial distribution (Figure 5.12, JQ1). These two observations suggest that when coactivator binding is compromised, Pol II Ser5P assemblies do not maintain

the same dense chromatin environment they otherwise might, and chromatin is somewhat excluded at close proximity. A similar flattening effect was observed with 1,6-hexanediol, with the most pronounced impact seen in type III clusters (Figure 5.12, Hex). This suggests that weak hydrophobic interactions play a role in anchoring chromatin or chromatin-associated proteins to the condensate periphery. In contrast, blocking transcription initiation with triptolide had minimal effect on the spatial DNA pattern. The peak enrichment dropped only slightly, and the overall variability seemed more like random fluctuations than a meaningful shift (Figure 5.12, TL). This observation means that with Pol II initiation blocked, new cluster formation may be disrupted, and pre-existing clusters could disperse or remain in partial contact with chromatin. The net effect is a more variable local chromatin arrangement, reflected in the data. Interestingly, inhibition of pause release and elongation using flavopiridol produced differential effects. In type II clusters, the DNA enrichment ridge was flattened (~0.98) and shifted outward, while type III condensates retained a typical chromatin profile (Figure 5.12, FP).

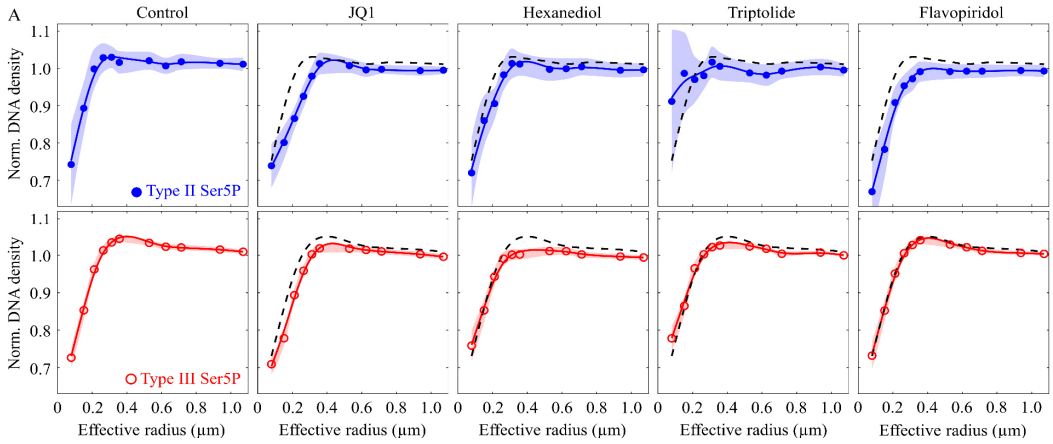

Figure 5.12: Radial chromatin organization around Pol II Ser5P condensates. DNA density profiles plotted as a function of radial distance from the centroids of type II (solid blue circles) and type III (open red circles) Pol II Ser5P clusters under control conditions and following treatment with JQ1, 1,6-hexanediol (Hex), triptolide (TL), and flavopiridol (FP). Each point represents the median DNA density across all clusters within a given radial shell. Shaded regions indicate 95% confidence intervals, calculated as ±1.58 × IQR / √n. Solid lines show smoothed trend curves to aid visualization. For comparison, dashed black lines in the treated-condition panels replicate the trend observed in control samples. Taken from [173].

Under both control and transcription-inhibited circumstances, the spatial distribution and intensity of Pol II Ser2P clusters are shown by the maximum intensity projections of background-free super-resolution STEDD images in Figure 5.13a. In the control nucleus, a considerable number of bright Pol II Ser2P aggregates occupy large portions of the nucleus, suggesting robust transcriptional activity. By contrast, nuclei treated with transcription inhibitors (JQ1, Hex, TL, and FP) contain fewer foci with notably reduced brightness, indicating a clear suppression of Pol II Ser2P enrichment. In addition, quantitative analysis of cluster intensity supports these observations (Figure 5.13b). Aggregates in this investigation were segmented in 2D frames to ensure a more thorough evaluation of cluster-based Pol II Ser2P levels. The control condition has a large number of high-intensity Pol II Ser2P foci, as seen in Figure 5.13b. In contrast, all treated samples lack this high-intensity subgroup, suggesting that treatments significantly lower active transcription. As was already discussed, each inhibitor targets a different aspect of transcription. JQ1 compound inhibits BET bromodomains, such as those on BRD4, which recognize acetylated histones and recruit transcriptional machinery. JQ1 causes transcriptional initiation and early elongation to be impeded by disrupting the interaction between BRD4 and chromatin, which in itself lowers Pol II Ser2P levels. The findings of this study indicate that JQ1 leads to a widespread reduction in Pol II Ser2P levels. This is reflected in the unimodal intensity distribution, which shifts toward lower values, pointing to a general inhibition of transcriptional activity. Moreover, Hex hinders the integrity of nuclear condensates important for forming transcription complexes. As a result, this alteration leads to reduced Pol II clustering and Ser2 phosphorylation. TL disrupts the activities of TFIIH, required for transcription initiation and promoter clearance, therefore preventing Pol II from entering effective elongation. FP acts as a direct inhibitor of CDK9. Inhibiting CDK9 prevents Pol II from transitioning to the elongation stage, causing a marked reduction in the Ser2P signal. Based on this study, Hex, TL, and FP produce bimodal intensity distributions, reflecting heterogeneous effects. This variability could arise from temporal effects, where some clusters are already engaged in elongation and retain Ser2P longer; spatial or chromatin context, where certain genomic loci resist drug effects more than others; variable drug sensitivity across cells; cell-to-cell variability in drug uptake or response; or differential kinetics of Ser2P dephosphorylation, all of which may contribute to the emergence of distinct cluster populations with high and low Ser2P signal intensities.

Furthermore, the box plot summarizes the mean Pol II Ser2P signal intensity across the whole nucleus for each condition in Figure 5.13c. Each dot on the plot corresponds to the average

pixel intensity from any given nuclear frame, giving a broad overview of transcriptional activity at the whole-nucleus level. Based on this analysis, nuclei treated with any of the four inhibitors showed a significant decrease in Ser2P compared with controls, consistent with the two previous panels.

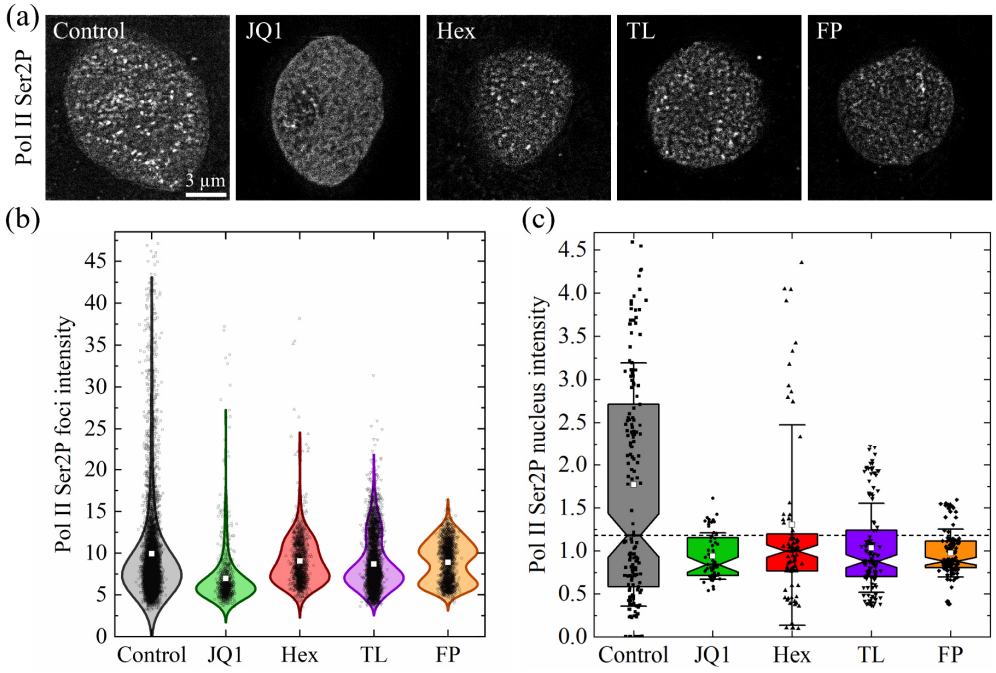

Figure 5.13: Influence of transcription inhibitors on the spatial arrangement of transcribed genes. (a) Volumetric image stacks (13.5 × 13.5 × 3.0 µm³) provide representative maximum-intensity projections that show nuclei in control conditions (no inhibitor) and conditions where transcription is inhibited. All images use a consistent contrast range, and the 3 µm scale bar applies to every panel. **(b)** Comparison of Pol II Ser2P foci intensity across treatment conditions using violin plot. Each data point represents the mean intensity of an individual Pol II Ser2P aggregate. Notably, to provide a more comprehensive calculation of cluster-based Pol II Ser2P levels, aggregates were segmented in 2D frames, yielding 8152 (control), 954 (JQ1), 1271 (Hex), 4033 (TL), and 1684 (FP) clusters, respectively. Violin plot widths are scaled to a uniform maximum across conditions, emphasizing the shape and spread of intensity distributions rather than group size. This approach highlights how different inhibitor treatments (JQ1, Hex, TL, FP) modulate the intensity profile of Pol II Ser2P foci relative to control. White squares mark the mean. Furthermore, the bandwidth of the kernel density estimation (KDE) that shapes the violin is determined using the Silverman's rule. Further details can be found in Table 5-1, which lists the number of segmented Pol II Ser2P clusters across various intensity ranges under each condition. **(c)** A box plot summarizes the average Pol II Ser2P signal intensity within entire nuclei (mean ± SD). Each point corresponds to the mean intensity of all pixels in a single nuclear frame for each treatment. Modified according to [173].

As mentioned in the Figure 5.13 caption, Table 5-1 provides detailed information on Pol II Ser2P cluster numbers across various intensity bins under various conditions. This table also clearly illustrates the unimodal and bimodal distribution patterns of Pol II Ser2P cluster intensities under different conditions. This table includes intensity bins up to 50 counts, matching the upper limit shown in Figure 5.13b. To avoid excessive empty or zero-count entries at higher intensities, which could clutter the data without providing meaningful insight, this upper threshold was chosen for the table. In the control column, numerous clusters appear

at mid to high-intensity bins (e.g., 7.0–10.0), indicating an active population of strongly phosphorylated Pol II molecules. By contrast, as is already discussed in the previous figure, in each inhibitor-treated sample, the overall number of detected clusters drops, and the counts in higher-intensity bins decrease sharply.

Table 5-1: Number of segmented Pol II Ser2P foci across intensity bins under different treatments.

Intensity bins' centers	Control	JQ1	Hex	TL	FP
0.0	0	0	0	0	0
0.5	0	0	0	0	0
1.0	2	0	0	0	0
1.5	0	0	0	0	0
2.0	0	0	0	0	0
2.5	0	0	0	0	0
3.0	4	0	1	0	0
3.5	23	3	3	9	0
4.0	85	23	1	62	4
4.5	190	64	10	121	10
5.0	319	141	21	139	40
5.5	469	167	44	221	122
6.0	622	145	97	330	141
6.5	770	110	103	339	139
7.0	830	67	121	411	100
7.5	764	51	110	373	95
8.0	684	32	95	298	68
8.5	553	28	85	254	72
9.0	410	18	66	188	72
9.5	348	14	80	141	120
10.0	288	9	62	113	138
10.5	197	6	48	95	134
11.0	192	11	79	93	101
11.5	130	4	55	82	103
12.0	105	9	50	104	72
12.5	110	5	40	98	68
13.0	105	3	29	109	38
13.5	67	4	14	90	26
14.0	65	1	11	90	11
14.5	47	7	9	55	2
15.0	43	6	7	49	2
15.5	39	3	3	39	4
16.0	35	2	3	24	1
16.5	46	2	2	30	1
17.0	45	2	4	20	0
17.5	25	0	1	15	0
18.0	33	0	0	5	0
18.5	18	0	1	4	0
19.0	24	1	0	6	0
19.5	24	0	0	8	0

20.0	16	0	0	2	0
20.5	15	0	0	1	0
21.0	12	2	1	5	0
21.5	12	1	0	1	0
22.0	11	1	4	2	0
22.5	13	0	2	0	0
23.0	21	0	1	1	0
23.5	11	1	0	1	0
24.0	12	0	1	1	0
24.5	11	0	1	0	0
25.0	13	1	0	1	0
25.5	12	0	0	1	0
26.0	13	0	0	1	0
26.5	11	2	1	0	0
27.0	12	1	0	0	0
27.5	6	0	1	0	0
28.0	8	0	0	0	0
28.5	10	1	0	0	0
29.0	10	0	0	0	0
29.5	6	0	0	0	0
30.0	7	1	0	0	0
30.5	8	0	0	0	0
31.0	11	0	0	0	0
31.5	5	0	0	1	0
32.0	14	0	0	0	0
32.5	1	0	0	0	0
33.0	5	1	0	0	0
33.5	7	1	0	0	0
34.0	5	1	0	0	0
34.5	10	0	0	0	0
35.0	4	0	1	0	0
35.5	5	0	1	0	0
36.0	5	0	0	0	0
36.5	3	0	0	0	0
37.0	7	2	0	0	0
37.5	4	0	0	0	0
38.0	6	0	1	0	0
38.5	2	0	0	0	0
39.0	4	0	0	0	0
39.5	5	0	0	0	0
40.0	2	0	0	0	0
40.5	3	0	0	0	0
41.0	6	0	0	0	0
41.5	7	0	0	0	0
42.0	2	0	0	0	0
42.5	3	0	0	0	0
43.0	3	0	0	0	0

43.5	2	0	0	0	0
44.0	0	0	0	0	0
44.5	1	0	0	0	0
45.0	2	0	0	0	0
45.5	2	0	0	0	0
46.0	2	0	0	0	0
46.5	0	0	0	0	0
47.0	2	0	0	0	0
47.5	0	0	0	0	0
48.0	0	0	0	0	0
48.5	0	0	0	0	0
49.0	1	0	0	0	0
49.5	0	0	0	0	0
50.0	1	0	0	0	0

The histograms in Figure 5.14a show how transcription inhibitors change the spatial interaction between elongating (Pol II Ser2P) polymerases inside the nucleus and promoter-proximal (Pol II Ser5P) polymerases. Each plot depicts the distribution of distances from each Ser5P cluster to up to four of its nearest Ser2P neighbors, within a 2.5 μm radius. Under control conditions, many Pol II Ser5P clusters (4015) are observed with closely spaced positions, with the decay extending almost to 2.0 μm. The dashed vertical line represents the average distance between Ser5P and Ser2P clusters. It shows that, under normal conditions, these clusters are usually located within a submicron range of each other, reflecting the typical coordination between transcription initiation and elongation. In contrast, all inhibitor treatments (JQ1, Hex, TL, and FP) lead to shifts in these distance distributions. First, the total number of Pol II Ser5P clusters detected decreases dramatically under each drug, consistent with a reduction in the formation or stability of initiation-competent polymerases. JQ1 blocks BET bromodomain proteins, which are crucial for promoter recruitment. As a result, it yields only 136 Ser2P clusters, which is a sharp reduction compared to the control. Hexanediol leads to 580 Ser2P clusters by disrupting phase-separated condensates that are essential for assembling transcription complexes. TL interferes with TFIIH activity, preventing promoter escape and resulting in 787 clusters. FP inhibits CDK9, the kinase responsible for Pol II Ser2 phosphorylation, which reduces the cluster count to just 226. In addition to reducing cluster counts, these agents also change the average distance between Ser5P and Ser2P clusters, generally shifting the mean distance to larger values. Reflecting the particular transcriptional block imposed by every inhibitor, this spatial gap suggests a breakdown in the typical coordination between initiation (Ser5P) and elongation (Ser2P). Representative 1 μm-thick maximum-intensity projections (Figure 5.14b) support this quantitative analysis. The control nucleus (top panel) displays

abundant, interspersed Ser5P (magenta) and Ser2P (green) foci, often appearing near one another. By contrast, each inhibitor-treated cell exhibits fewer and more diffusely arranged clusters, with Ser5P and Ser2P foci showing reduced adjacency. In a nutshell, these findings indicate that transcription inhibitors not only diminish the overall presence of Pol II Ser5P clusters but also increase the spatial separation between initiation and elongation foci, aligning with their known mechanisms of action in restraining Pol II activation, promoter engagement, and productive elongation.

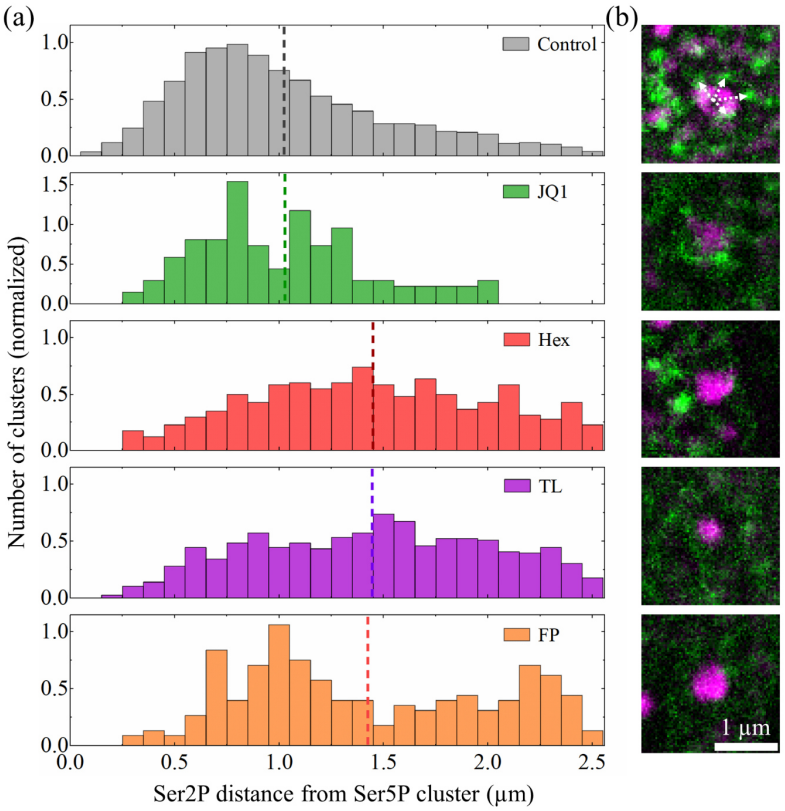

Figure 5.14: Impact of transcription inhibitors on the spatial arrangement of transcriptional clusters and transcribed genes. (a) Histograms of the distance between each Pol II Ser5P cluster and up to four nearest Pol II Ser2P clusters within a 2.5 µm radius. Histograms are normalized such that the area is equal to one. Vertical dashed lines indicate the mean distance for each treatment condition. Based on the provided criteria, 4015 (control), 136 (JQ1), 580 (Hex), 787 (TL), and 226 (FP) Pol II Ser2P clusters were detected. Further details, such as the number of segmented Pol II Ser2P clusters per distance range, are given in Table 5-2. **(b)** Representative maximum-intensity projections of 1 µm-thick sections compare control nucleus and inhibitor-treated nuclei. The contrast scale is the same for all images, and a 1 µm bar is provided for reference. Taken from [173].

Moreover, Table 5-2 summarizes the Pol II Ser2P cluster counts found in every distance bin when comparing inhibitor-treated and control cells, as the caption of Figure 5.14 notes. Many clusters spanning the 0–2.5 µm distance range abound in the control condition. This indicates rather high concentrations of elongating polymerases. Especially, there are peaks about 0.7–

1.0 µm where the control condition detects several hundred clusters per bin, therefore showing the frequent occurrence of Pol II Ser2P clusters at these submicron separations. By contrast, each inhibitor-treated sample shows consistently lower cluster counts across nearly all distance bins. For example, JQ1 highlights reduced Ser2P signals by resulting in very few clusters in the lower distance bins (e.g., 2 at 0.3µm, 11 at 0.6–0.7µm). Reduced counts in most bins by the other inhibitors (Hex, TL, FP) also point to fewer overall clusters and perhaps movement toward larger distances in the distribution of surviving foci.

Table 5-2: Count of Pol II Ser2P clusters across different distance bins under various treatments.

Distance bins' centers (µm)	Control	JQ1	Hex	TL	FP
0.0	0	0	0	0	0
0.1	15	0	0	0	0
0.2	48	0	0	2	0
0.3	99	2	10	8	2
0.4	194	4	7	11	3
0.5	264	8	13	22	2
0.6	366	11	17	35	6
0.7	382	11	20	27	19
0.8	395	21	29	38	9
0.9	356	10	25	45	16
1.0	303	6	34	35	24
1.1	268	16	35	38	17
1.2	212	10	32	34	13
1.3	183	13	35	42	9
1.4	159	4	43	45	9
1.5	114	4	34	58	4
1.6	114	3	28	53	8
1.7	110	3	37	36	7
1.8	87	3	29	41	9
1.9	84	3	21	41	10
2.0	78	4	25	40	7
2.1	45	0	34	32	9
2.2	48	0	18	31	16
2.3	42	0	16	35	14
2.4	32	0	25	24	10
2.5	17	0	13	14	3

5.6 Conclusions

In this chapter, the nanoscale architecture and activity profiles of chromatin and RNA Pol II have been studied. These investigations were carried out by applying the home-built three-dimensional, multi-color STEDD fluorescence microscopy to sphere-stage zebrafish embryonic cells. Combining this high-resolution, background-free imaging technique with a thorough cluster segmentation and classification approach allowed one to clearly identify particular Pol II Ser5P cluster types (type I, II, and III), each connected to various transcriptional states. The volume-dependent solidity measurements and the intensity-based criteria were applied to characterize these classes. The presented data demonstrate the existence of a finely tuned nuclear topology that supports gene expression by regulating the distribution and morphology of Pol II Ser5P, Pol II Ser2P, and DNA.

Further experiments using JQ1, Hex, FP, and TL as transcription inhibitors indicated that blocking various transcriptional processes can selectively affect cluster architecture and Pol II functions. Every inhibitor yielded different changes in the solidity, mean intensity, and volume of Pol II Ser5P aggregates. Of particular note is that the proportion of clusters of types II and III with respect to the total number of clusters was reduced most significantly by the FP treatment. Super-resolution imaging confirmed that JQ1, Hex, and FP induced a marked increase in the compactness of type II clusters, whereas TL did not produce a significant effect. By comparison, type III clusters showed more varied results in solidity, ranging from no change with JQ1 to improved compactness with Hex, and decreased solidity under TL and FP. Moreover, the average intensity of the Pol II Ser5P cluster decreased in all inhibitor-treated samples.

Collectively, the inhibitors diminished the effective transcription rate, which is evident from the reduced number and intensity of Pol II-Ser2P foci. Flavopiridol and JQ1 account for the direct component of this decline by arresting polymerases at the pause-release/elongation checkpoint, whereas Triptolide and 1,6-hexanediol contribute an indirect component by crippling transcription initiation and thereby limiting the supply of polymerases that can enter productive elongation.

In addition, the impact of transcription inhibitors on reducing the transcription rate was further supported by histogram analyses of the distances between each Pol II-Ser5P cluster and its four nearest Pol II-Ser2P clusters. Treatment with Hex, TL, or FP pushes Ser2P puncta away from their Ser5P counterparts, increasing the average gap to 1.3 μm or more while simultaneously

trimming the overall number of Ser2P sites. By comparison, in unperturbed cells, the majority of Ser2P puncta sit within roughly 1 μm of a Ser5P cluster. The combined enlargement of spacing and loss of signal implies a pronounced slowdown in elongation and a physical separation of actively transcribed genes from the clusters that seed them. JQ1 eliminates Ser2P signals even at short range, implying that this super-enhancer blockade shuts down elongation almost completely rather than simply spatially redistributing.

Two independent assays, namely DNA-intensity histograms and radial-density maps, paint the same picture of how RNA-Pol II condensates manage their chromatin environment. In untreated cells, Ser5- and Ser2-phosphorylated Pol II clusters are largely DNA-poor, yet a small high-intensity tail in the histogram betrays tight chromatin anchoring at sites of robust transcription. Disturbing different stages of the transcription cycle disrupts that arrangement in distinct ways. Suppressing super-enhancer activity with JQ1, altering the material state of condensates with hexanediol, or blocking pause-release with flavopiridol wipes out the high-intensity DNA fraction, implying that bulk chromatin is largely repelled. Hindering initiation with triptolide has the opposite effect: DNA floods into Ser5P assemblies, signalling a collapse of the normal partitioning barrier. Radial-density profiles sharpen the contrast. Compact, spherical (type II) clusters exclude DNA from their inner ~400 nm; this exclusion is accentuated by JQ1, hexanediol, or flavopiridol, but virtually disappears after triptolide treatment. More open (type III) clusters follow the same trends, however, less dramatically. The collective data indicate that chromatin anchoring at condensate surfaces relies on the integrated action of super-enhancers, phase-separation chemistry, and the kinetic state of Pol II; upsetting any one component rearranges the nanoscale architecture in a morphology-dependent fashion.

Lastly, as previously noted, the research presented in this chapter has been prepared as a manuscript for submission to a peer-reviewed scientific journal. The contributions of co-authors to this work are as follows: Andrei Kobitski participated in the scientific discussions and data analysis. G. Ulrich Nienhaus and Lennart Hilbert supervised the project, contributing to the conception, discussion, and interpretation of the results, as well as the drafting of the text.

Chapter 6: Sensorless Photon-Efficient Aberration Correction in 3D-STEDD Microscopy

6.1 Introduction

As discussed in previous chapters, STED microscopy, especially when combined with background correction at the single-pixel level, has greatly enhanced the field of optical imaging in biophysics by enabling nanoscale resolution and allowing for observation and quantification of structures and processes as close as possible to reality. Despite these advantages, this microscopy technique does not lack challenges. One of the critical difficulties in achieving optimal resolution and image quality is optical aberration, especially in deep cell measurements of thick samples ($\geq 30\mu m$), which can enormously degrade the performance of STED systems. Therefore, an efficient method in terms of sample exposure and measurement time is important for correction of dominant aberrations in STED microscopy. This chapter of the thesis discusses the causes of aberrations, their effects on imaging, and the methods used to tackle this problem.

It is worthwhile to clarify that this chapter builds upon collaborative work that resulted in a published paper [72]. In that study, the initial feasibility of the proposed approach was demonstrated by Dr. Siqing Dai, with whom I closely collaborated. My primary contributions to this paper involved the enhancement of the optical setup, the sample preparation, and daily discussions, which were crucial for the success of the initial experiments.

This chapter aimed to share this collaboration, remeasure the principle of the proposed technique, and introduce further experiments necessary to validate reproducibility, extend the scope of the original work, and form a component of my independent research for this doctoral dissertation.

6.2 Motivation and Significance of the Study

In theory, the STED imaging method is capable of achieving infinitely high resolution by an enormous increase in the intensity of the depletion beam. Nevertheless, the resolving power significantly deteriorates due to the quality of the intensity minimum of the donut and bottle depletion beam profiles in the presence of system- and sample-induced aberrations [72]. In other words, the high degree of optical property heterogeneity in biological tissues and inherent aberrations in optical systems can significantly reduce the quality of the depletion beam's intensity minimum, thereby worsening the resolving power of STED microscopy [75]. In fact, by causing extremely distorted wavefronts, these aberrations make it almost impossible to conduct STED imaging deeper than about 30µm into specimens. In the aberration-correction workflow developed here (Figure 6.1a), we created a sandwich structure to quantify how system- and sample-induced aberrations distort the depletion point-spread function (PSF). The structure was assembled by mounting the biological specimen, a zebrafish animal cap, between a coverslip and a microscope slide, both of which were pre-coated with 80 nm gold nanoparticles and 40 nm fluorescent nanobeads. Scattering from the gold beads provided the reference signal used to map and correct the aberrations. As can be seen in Figure 6.1b and c, the donut depletion PSF exhibits a certain degree of robustness against aberrations [72,75]. However, the bottle depletion beam PSF is exceedingly sensitive to aberrations [83], up to the point where the central intensity minimum vanishes entirely [72]. In other words, as measurement depth increases, the effective STED microscope PSF becomes more elongated in the axial direction, as the effect of z-STED depletion gradually disappears.

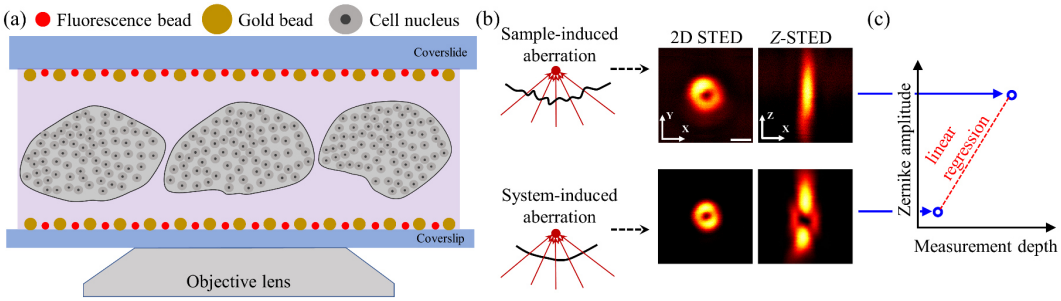

Figure 6.1: Schematic of STED imaging of zebrafish embryo samples mounted in a sandwich structure in the presence of depletion beam aberrations induced by the optical system and the sample. (a) The diagram shows a sandwich sample made up of layers of gold and/or fluorescent nanobeads immobilized to the microscope coverslide and coverslip. **(b)** Illustration of aberrations depth dependency using gold bead scattering: At the lower surface of the specimen, the wavefront experiences minor distortions primarily due to imperfections in the optical components or misalignment issues. As the measurement depth increases within the specimen, the sample-induced distortions become increasingly severe. Scale bar: 0.3 µm. **(c)** Exploiting linear regression to map the amplitudes of different aberration modes across the sample as a function of measurement depth.

Adaptive optics (AO) provides a powerful solution for achieving the highest resolution in STED microscopy by dynamically correcting for aberrations in real-time, utilizing spatial light modulators or deformable mirrors [72,164,165]. In the modal AO approach, a set of mutually independent (Zernike) modes conveniently models aberrations [72]. These modes are mathematical functions describing different types of optical distortions, such as tip, tilt, defocus, astigmatism, coma, and spherical. Using this method, the amplitude of each mode is systematically varied using an SLM during iterated image acquisition, allowing the specific impact of each single type of aberration to be analyzed with a fine granularity. After collecting a set of pre-distorted images, they are ranked using robust image quality metrics such as intensity [83,165–167], sharpness [83], and Fourier ring correlation (FRC) [164] to determine which amplitude of distortion is capable of system and sample aberration correction. Since aberrations must be corrected in both 2D- and z-STED beams for each primary aberration, including astigmatism (Z_2^2, Z_2^{-2}), coma (Z_3^1, Z_3^{-1}), and spherical (Z_4^0), a modal-based AO implementation becomes a time-consuming process, requiring hundreds of sample exposures. Therefore, this results in the signal-to-noise degradation of the final acquisition due to sample photobleaching. The first motivation behind the exploration of optical aberration correction in 3D-STED microscopy was to find a photon-efficient correction method that would substantially shorten exposure time and, accordingly, photobleaching and phototoxicity. This, therefore, allows high-quality 3D STEDD imaging of zebrafish embryo samples with a homogeneous image quality over varying depths. To implement this, the novel method avoids directly exposing the biological sample to the powerful STED beam, unlike conventional AO approaches. Instead, as seen in Figure 6.1a, the light scattered by gold beads is used both before and after it goes through the biological sample. In this schematic, the coverslip and coverslide are both immobilized with a mix of gold beads (Ø 80 nm, OD 1, Sigma-Aldrich) and fluorescent nanobeads (Ø 40 nm, FluoSpheres, dark red fluorescent (660/680 nm), ThermoFisher Scientific). Afterward, the biological samples with immersion medium are added between the coverslip and coverslide of the microscope. An analysis of the aberrated wavefront is made by measuring the scattered light and decomposing the wavefront into its constituent Zernike modes, whose amplitudes are varied systematically. In order to find the optimal parameters of wavefront pre-compensation, a comparative analysis of the structures of experimental PSFs and their ideal counterparts is made using cross-correlation (CC) as a quantitative indicator for the image quality assessment. To minimize the distortion of the microscope effective PSF, the depletion wavefronts are altered by applying Zernike modes for

primary aberrations such as astigmatism (Z_2^2, Z_2^{-2}), coma (Z_3^1, Z_3^{-1}), and spherical (Z_4^0) aberrations, which are primary modes in the context of aberration correction in STED microscopy [72,75,168]. This is further shown in Figure 6.1c, which shows that linear interpolation between coefficients at zero and maximum depths gives pre-compensation parameters that hold for a variety of sample depths [72].

6.3 Results and Discussions

6.3.1 Zernike Mode Decoupling in High NA Objective Lenses

In high-numerical-aperture objective lens systems, correction of the aberrations needs an understanding of the intrinsic strong correlation between primary aberrations and displacement modes. In these objective lenses, the displacement modes introduce or modify the aberrations, which ruin the orthogonality of Zernike modes. Designed for a wide angular light collection, these objective lenses are highly susceptible to wavefront distortions induced by axial, lateral, and angular displacements. Those can bring in defocus, coma, and higher-order aberrations, breaking the symmetry of the system and hence the orthogonality of Zernike modes. It is this coupling between the modes that complicates wavefront correction. Also, to counteract these influences and to save the performances, besides a very tight optical setup alignment, adaptive optics-based schemes are necessary [72,169]. As a result, the PSF relocation should be investigated as a function of the ratio between vertical coma (Z_3^{-1}) and tilt (Z_1^{-1}), horizontal coma (Z_3^1) and tip (Z_1^1), and between the primary spherical mode (Z_4^0) and defocus (Z_2^0) to restore their inherent orthogonality.

According to the mathematical definition of wavefront aberration provided in equation (2.25), this part of the study is designed to examine how the primary aberration modes change the focal volume displacement of the depletion laser by measuring the locations of the center minima of imaged gold nanobeads with 2D-STED and z-STED beams [72]. As an example, using the *z*-STED, the best coupling ratio (C_2^0/C_4^0) between Z_2^0 and Z_4^0, in order to identify the ratio at which the PSF reposition is minimized, was obtained by fixing this ratio to a specific value while adjusting C_4^0 within a reasonable range (-1.5 to 1.5 radian) and measuring system PSF consecutively at the aforementioned amplitudes. Afterward, the displacement between the central minimum at each amplitude was calculated with respect to the initial PSF position ($C_4^0 = 0$). This procedure was repeated over multiple gold beads to obtain more reliable statistics. Figure 6.2 shows the displacement as a function of C_4^0, while the coupling ratio was fixed at 1.60.

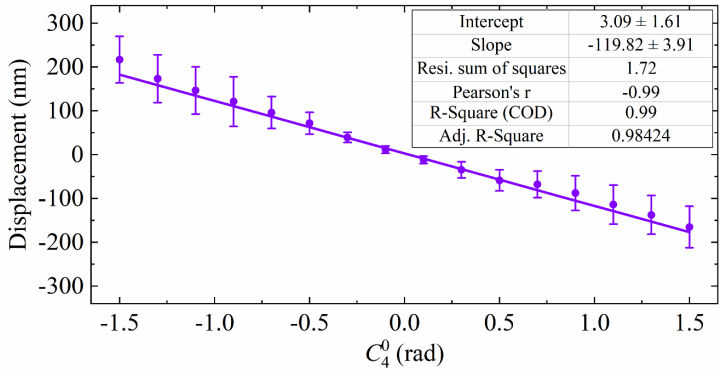

Figure 6.2: Displacement calculation as a function of C_4^0 at the fixed ratio of $C_2^0/C_4^0 = 1.60$ by acquiring reflection images of five gold beads.

The same procedure was repeated, changing the coupling ratio up to 2.40, to find the optimal ratio that minimizes the displacement, which occurs when the slope of the fit approaches zero. Figure 6.3(a) and (b) show the slope of z-STED and 2D-STED PSF displacements at different coupling ratios, respectively. As can be seen, the optimal ratios that restore the orthogonality feature of the Zernike modes are 2.00, 1.40, and 1.40 for C_2^0/C_4^0, C_1^1/C_3^1, and C_1^{-1}/C_3^{-1}, respectively. Utilizing this information, combinations of the coupled Zernike modes with amplitude ratios that minimize the shift were consistently applied.

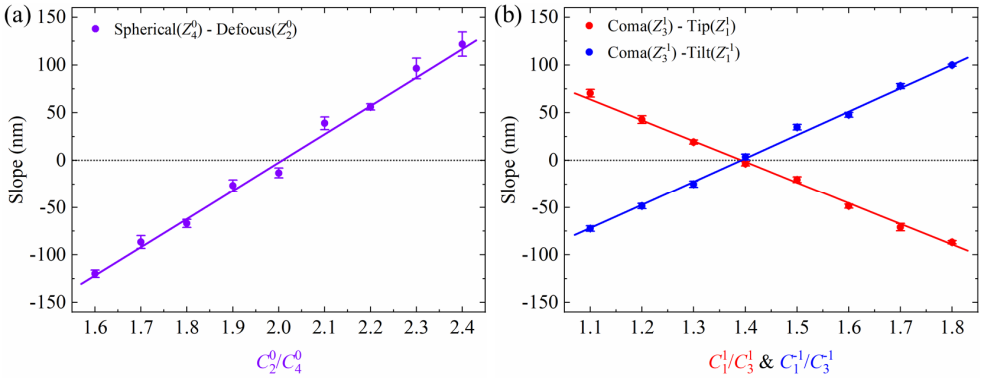

Figure 6.3: Quantification of coupling coefficients between Zernike modes. Displacement slopes were calculated for Zernike amplitude ratios between **(a)** defocus and primary spherical aberration (C_2^0/C_4^0) for the *z*-STED PSF and **(b)** tip and horizontal coma (C_1^1/C_3^1), and equivalently tilt and vertical coma (C_1^{-1}/C_3^{-1}) for the 2D-STED PSF, by acquiring reflection images of five gold beads.

6.3.2 Correction of STED Beam Aberrations Using a PSF-Based Technique

In this section, the aim is to explain the investigation protocol for determining the optimum amplitudes of Zernike polynomials required to compensate for system- and sample-induced aberrations. To find the finest amplitude for a given Zernike, the microscope PSF was captured using a gold nanobead sequentially as a frame stack with varying amplitude of the given aberration (Figure 6.4). To ensure a reliable estimation, this procedure was repeated on multiple

beads. Afterward, the acquired multiframe images including of pre-distorted PSFs, was compared to the simulated ideal PSF frame by frame using a cross-correlation metric:

$$CC = \frac{\sum_{m,n} (A_{mn} - \bar{A})(B_{mn} - \bar{B})}{\sqrt{\sum_{m,n} (A_{mn} - \bar{A})^2 \sum_{m,n} (B_{mn} - \bar{B})^2}}. \quad (6.1)$$

In this context, A_{mn} and B_{mn} represent the pixel intensities with m, and n indices for the simulated and measured PSFs, respectively, with the overlines indicating average values. It should be noted that the experimental PSF was firstly aligned with the calculated one and normalized to its maximum value, before computing the cross-correlation.

The optimal aberration correction amplitude was then derived from the maximum of a global parabola fit applied to the cross-correlation values calculated at different pre-distortion amplitudes for multiple beads.

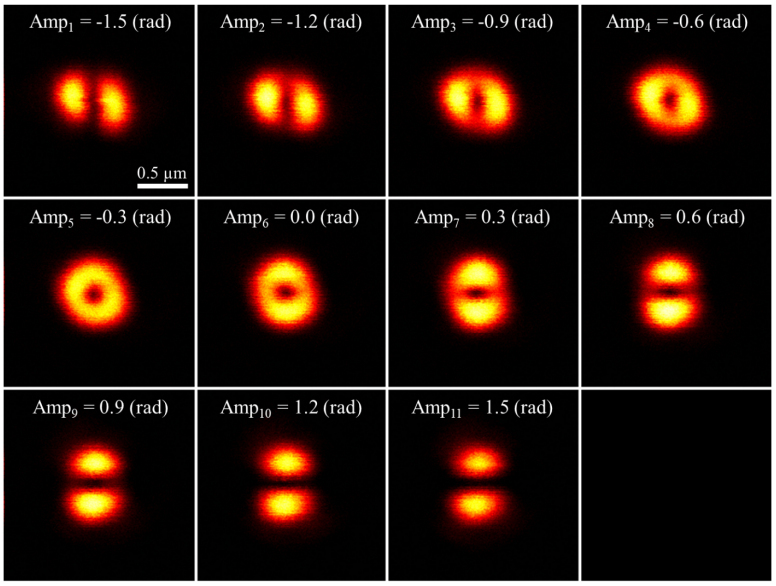

Figure 6.4: Visualization of 2D-STED PSF variation at different amplitudes of the astigmatism aberration (Z_2^{-2}). Here, "Amp$_i$" refers to the amplitude of the Zernike mode, which ranges from -1.5 to 1.5 radians across different frame numbers.

In Figure 6.5, the AO optimization protocol is exemplified with data for the 2D-STED PSF at the measurement depths of 0 µm (lower surface) and 110 µm (upper surface). To this aim, the contribution of the primary Zernike modes to the deformation of the 2D-STED PSF was studied one after the other (Figure 6.5a). It means that after each Zernike's complete correction at the given depth, the optimal amplitude of that specific mode was applied, and then the next Zernike was studied. As shown in the left column of Figure 6.5b, the STED PSF at a depth of 0 µm was measured for each Zernike mode using 10 gold nanobeads. A global parabolic global fit was

then applied to determine the optimal amplitude of each primary mode. Following this protocol, the system aberration at 0 µm was first measured and corrected. The same procedure was then repeated at 110 µm (right column of Figure 6.5b). After determining the optimal amplitudes and their standard errors from the parabolic fits, a linear regression was performed on the mean ± standard errors of these amplitudes at measurement depths of 0 and 110 µm for a given Zernike mode (Figure 6.5c). As was concluded in previous literature based on scattering imaging of gold beads and fluorescent imaging of dark red beads within different depths of a phantom sample, a simple linear interpolation of parameters taken at zero and maximum depth allows a correction for arbitrary depths within the sandwich sample [72]. Additionally, as shown in Figure 6.5c, the aberration amplitudes are set to zero at a depth of 0 µm, indicating that they were corrected before measuring the aberration amplitude at a depth of 110 µm.

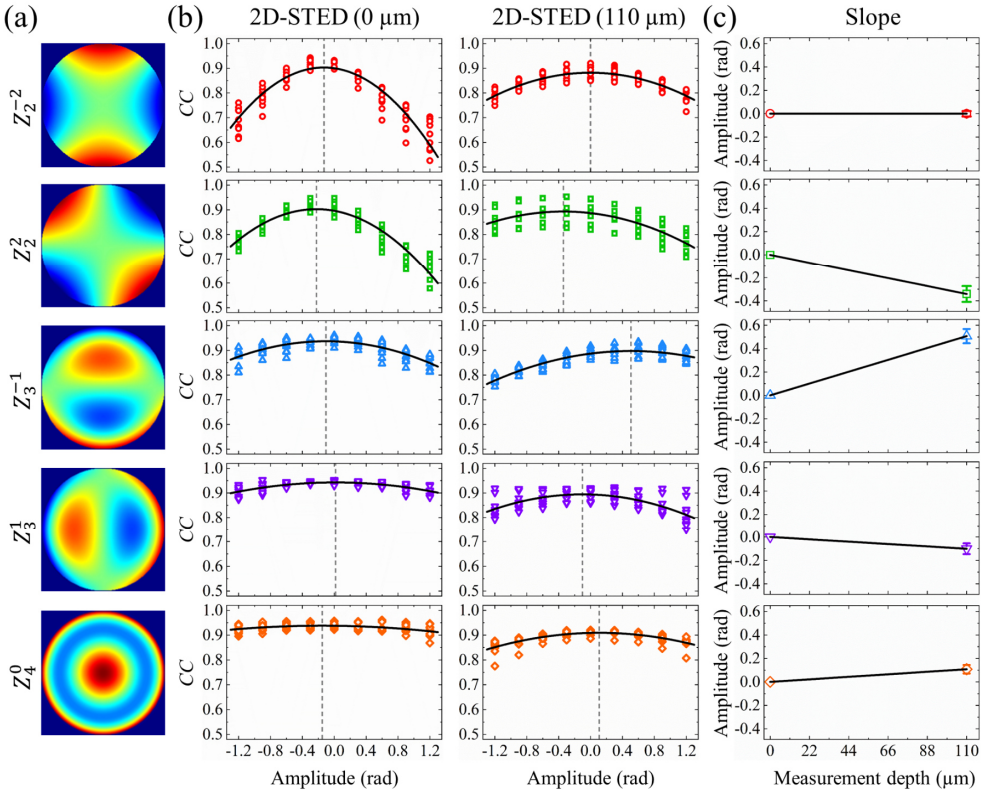

Figure 6.5: Quantitative assessment of system- and sample-induced aberrations demonstrated in 2D-STED beams at measurement depths of 0 µm and 110 µm. (a) Representation of Zernike polynomials associated with astigmatism (Z_2^{-2}, Z_2^2), coma (Z_3^{-1}, Z_3^1), and spherical (Z_4^0). **(b)** Sequential optimization of the Zernike mode amplitudes for the 2D-STED PSF at the coverslip (0 µm) and microscope cover slide (110 µm) using cross-correlation (*CC*) data, calculated for ten of individual gold nano beads (80 nm ⌀) as a function of the Zernike amplitude. The gray dashed line represents the maximum of a parabola fit (black solid line). **(c)** Based on the maximum of the parabolas and the standard errors derived from panel (b), a linear regression (solid line) was applied to model the variation of the optimal amplitudes of the given Zernike polynomial along the measurement depth.

Furthermore, it should be noted that when it comes to the aberration correction of the z-STED beam, in addition to the routine that was explained to obtain Zernike mode coefficients, the radius ratio, r_1/r_2, of the π- and 0-phase circular regions in the cylinder phase pattern should be investigated. This examination is crucial because this parameter controls the minimum intensity of the z-STED beam focus via interference. Since this radius ratio is the most decisive parameter for axial STED PSF, the correction procedure should be started by optimizing this parameter and then Zernike polynomials [72]. As was shown in Figure 6.1(b), this ratio varies with measurement depth. At the microscope cover slide (110 µm), the axial PSF was completely distorted, lacking any intensity minimum at the center. In other words, to achieve destructive interference and generate a proper z-STED PSF, the ratio r_1/r_2 must be adjusted according to the measurement depth, especially when imaging deep within a sample. Figure 6.6 (a) and (b) show the z-STED PSF at different radius ratios for the coverslip (0 µm) and the microscope cover slide (110 µm), respectively. As observed, the radius ratio plays a crucial role in determining the PSF shape, which is significantly influenced by measurement depth. At 110 µm, the range of radius ratios that produce a proper axial PSF differs substantially from the range at the coverslip. Similar to the routine to find the optimal amplitude of the Zernike polynomial, here, the experimentally measured PSFs were compared to the theoretical one using a cross-correlation metric. Based on measurements from multiple beads at these two heights, the optimal ratio was determined to be 0.40 and 0.27 for depths of 0 µm and 110 µm, respectively. Afterward, a linear interpolation was performed to compensate for the change of this parameter along with the measurement depth.

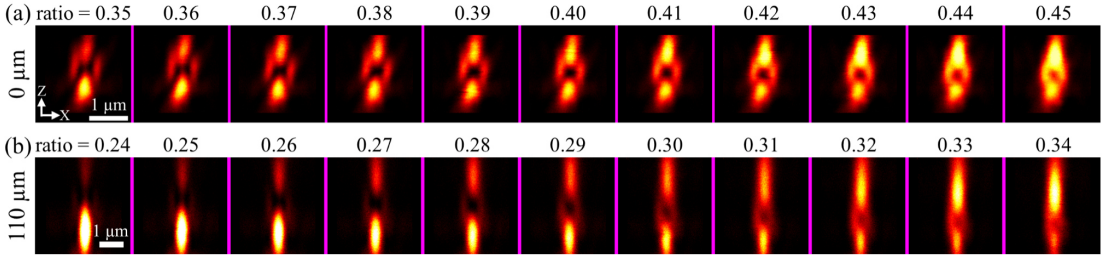

Figure 6.6: Investigation of the effect of radius ratio, r_π/r_0, on the cylindrical PSF. Z-STED PSF visualization at depths of **(a)** 0 µm and **(b)** 110 µm, using immobilized gold nanobeads on a microscope coverslip and coverslide, respectively. The region of interest in panel (a) is 2.5 × 2.5 µm², while in panel (b) it is 4.0 × 4.0 µm².

Additionally, Figure 6.7(a) and (b) show the efficiency of aberration correction at the microscope coverslip (0 µm) and 110 µm for 2D- and z-STED PSFs, respectively. The STED microscopy PSFs have a greatly enhanced intensity distribution that nearly matches the simulated PSFs, even in the highly distorted axial PSF at 110 µm measurement depth. This picture shows that the whole aberration correction calibration process has been precisely

carried out. Consequently, fluorescently tagged samples, including zebrafish embryonic cells and immobilized polystyrene beads, can be assessed deep within cells in the next stage.

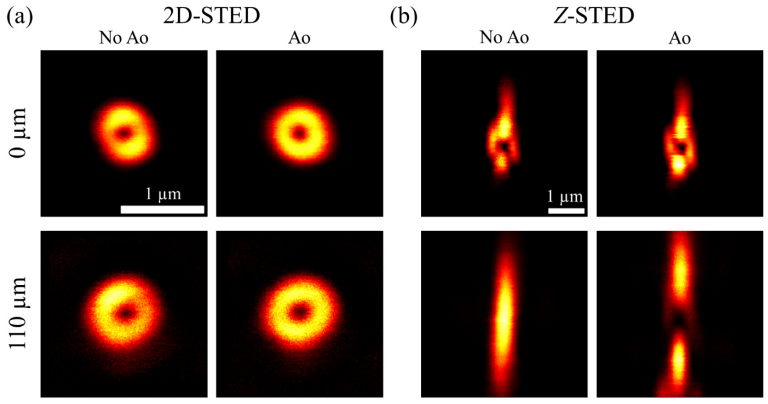

Figure 6.7: Illustration of representative (a) 2D-STED and (b) Z-STED PSFs at depths of 0 µm and 110 µm, shown before and after aberration correction.

6.3.3 Temporal Reproducibility in Aberration Correction

Investigating the reproducibility of the optimum amplitudes for aberration compensation in subsequent days is one of the most important questions to study. It is important to ascertain if the whole aberration correction process should start from the beginning, as a consistent investigation of biological problems usually needs the gathering of a large image data set of the same sample over several days. In other words, since the implementation of the entire aberration correction takes up to almost two hours, it is highly valuable to understand if this time can be saved when measuring the same sample on subsequent days. To this aim, exemplified using the 2D-STED beam, the optimum amplitudes for correcting astigmatism (Z_2^{-2}, Z_2^2), coma (Z_3^{-1}, Z_3^1), and spherical (Z_4^0) aberrations were investigated in three days in a row at measurement depths of 0 µm (microscope coverslip) and 110 µm (microscope slide). As shown in Figure 6.8, based on the optimal amplitudes derived from cross-correlation analysis between measured beads PSFs and a simulated one, it can be seen that 2D-STED PSF aberrations stay relatively constant within a few days, both at 0 µm and 110 µm. By this analysis, it can be observed that there is no need to repeat the aberration correction protocol every day, at least for a few of the next days, when it is optimized on the first day. This finding is in line with expectations since system-induced PSF aberrations originate from minor optical system misalignments, which are relatively constant in the custom-built setup. Also, sample-induced aberrations should stay pretty stable, especially if the same sample was studied. This is because sample-induced aberrations are mostly caused by a mismatch in the refractive indices of the glass and the mounting medium.

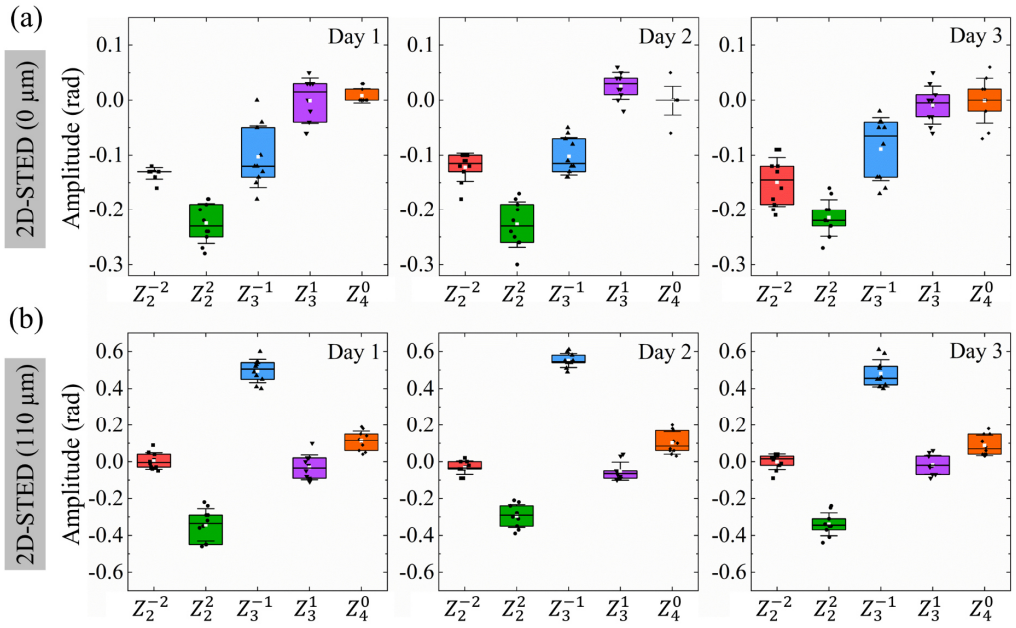

Figure 6.8: Temporal evaluation of the reproducibility of aberration correction parameters. Analysis of the variation in the optimal amplitudes of Zernike polynomials for correcting astigmatism and coma aberrations, demonstrated using a 2D-STED beam at depths of **(a)** 0 µm and **(b)** 110 µm over a consecutive 3-day period. Each box plot in this analysis, displaying the mean ± SD, represents 10 data points for each Zernike polynomial, indicating the optimum amplitude for aberration correction based on various beads.

6.3.4 Evaluation of Linear Interpolation Accuracy for Aberration Correction

Imaging of dark red fluorescent beads (DRBs, 40 nm ⌀) using both regular 3D-STED and AO 3D-STED modalities was done to evaluate the feasibility of using linear interpolation to compensate for aberrations in 2D- and *z*-STED PSFs at different depths. For this investigation, a phantom sample of 110 µm thickness was made up of DRBs that were evenly spread out in the volume by immobilization in a clear agarose gel [72]. The phantom sample was prepared to have the same refractive index as the sandwich structure, as thoroughly detailed in Dai et al.'s publication [72]. In this experiment, the beads were excited using the 640 nm laser beam at 3.8 µW at 0 µm depth and 7.6 µW at 110 µm depth. Indicating the minor susceptibility of the 2D-STED PSF to aberrations, as can be seen in Figure 6.9, at 110 µm depth and 100 mW STED beam power, adaptive optics compensation does not have a great impact on the lateral resolution (e.g., 105 ± 40 vs. 90 ± 21 nm for STED and AO STED, respectively) [72]. However, the lateral resolution at all depths is significantly improved by correcting for primary aberrations, which brings the FWHM values very close to the values at zero depth (69 ± 15 nm at 100 mW power) [72]. In contrast, by comparing the blue with green square symbols in this figure, indicating axial resolution at 110 µm without and with AO compensation, respectively, it can be observed that the wavefront correction significantly improves the axial resolution. It

is evident that, without correction, aberrations totally demolish the z-STED beam resolution enhancement throughout the whole spectrum of STED beam powers [72]. Furthermore, a qualitative comparison between traditional and wavefront-corrected STED imaging is presented in Figure 6.9b. Consistent with the findings in panel (a), wavefront correction significantly enhances the resolution and contrast of bead fluorescence images. This improvement is evident in the reduced axial extent of the corrected PSF (green frame) compared to the traditional STED PSF (blue frame). However, only a slight improvement in lateral resolution is observed with adaptive optics compared to standard STED imaging.

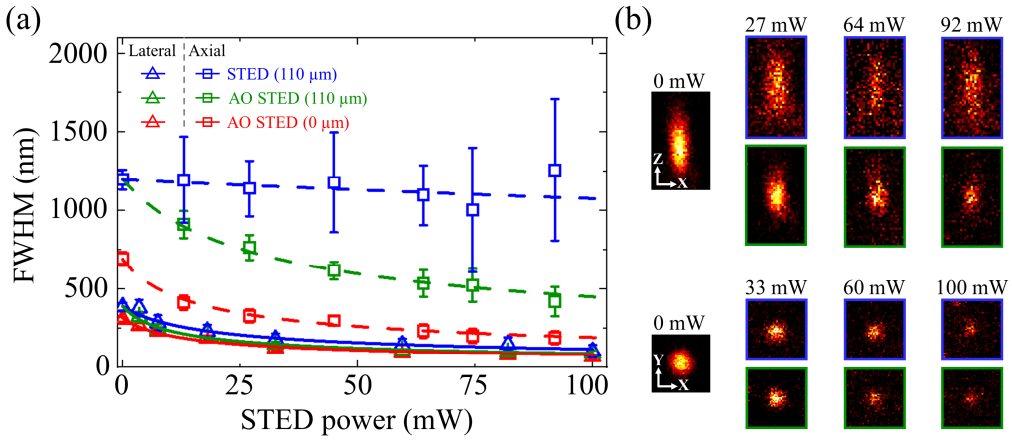

Figure 6.9: accuracy assessment of linear interpolation for aberration correction based on resolution measurements in STED and AO-STED. (a) The FWHMs of bead PSFs were measured at different depletion beam powers, both laterally and axially, at depths of 0 µm and 110 µm using 3.8 µW and 7.6 µW of the 640 nm excitation laser, respectively. Triangles with solid lines represent the lateral resolution, while squares with dashed lines indicate the axial resolution. Red and green colors correspond to AO-STED measurements at depths of 0 µm and 110 µm, respectively, whereas blue represents STED measurements at 110 µm. The lines are fits based on the STED resolution (see equation (2.22)). **(b)** Representative *XY* and *XZ* images taken with varying depletion powers, illustrating exemplary STED (blue frames) and AO-STED (green frames). Taken from [72].

6.3.5 Zebrafish Embryos Imaging with AO 3D-STEDD Nanoscopy

This section examines the effectiveness of the developed aberration correction protocol during 3D-STEDD nanoscopy of nuclei within zebrafish embryo animal caps. In this experiment, the 2D-STED and z-STED PSF correction parameters were optimized using linear interpolation from PSF analysis of gold beads in a sandwich structure. Figure 6.10a presents a maximum intensity projection of four nuclei at depths of 57, 90, 94, and 101 µm from the coverslip. As expected, due to the highly distorted axial depletion beam deep within the nucleus, Pol II Ser5P clusters are clearly discernible only with aberration-corrected STEDD, whereas conventional STEDD imaging without AO fails to resolve them. For a quantitative comparison, a representative cluster within each nucleus is marked with white squares, from which an intensity line profile is extracted in both the lateral (horizontally across the center of the square)

and axial directions. In other words, the cluster intensity fluctuations in a maximum intensity projected image highlight the differences between AO-corrected and non-AO-corrected approaches laterally, while the line profile parallel to the measurement acquisition captures these differences axially within 3D stack images. Figure 6.10b shows that the line profiles coincide with the qualitative results, therefore indicating that AO correction greatly increases measurement depth inside a cell. The major distortion of the *z*-STED beam totally depletes fluorescence signals without aberration correction, so it is difficult to get the spatial organization and morphological characteristics of the clusters.

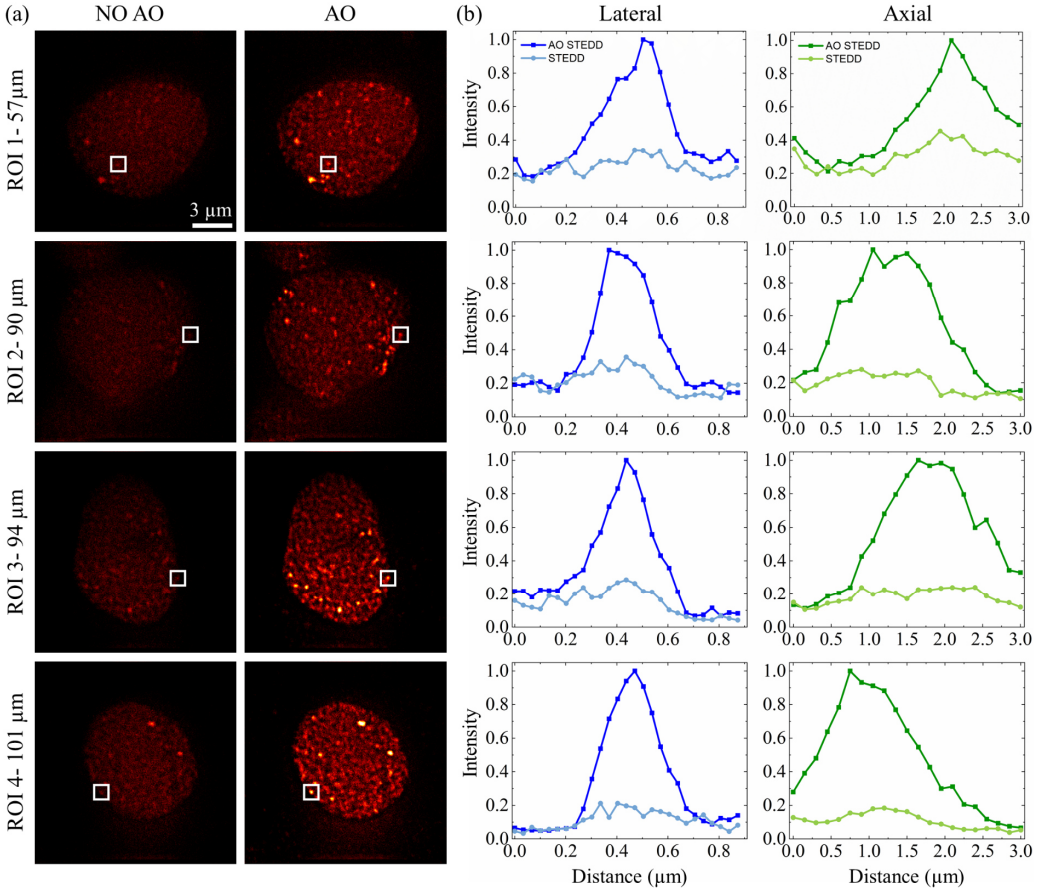

Figure 6.10: Qualitative (a) and quantitative (b) comparison of aberration-uncorrected and corrected 3D-STEDD imaging of cell nuclei in a zebrafish embryo. The nuclei were positioned at depths of 57, 90, 94, and 101 µm from the coverslip, covering a volume of 15×15×3 µm³ (450×450 pixels, 21 frames). All images are displayed using the same contrast settings. Lateral line profiles in panel (b) were extracted from MIP images, while axial profiles were derived from 3D stacks. For consistent comparison, line profiles were normalized to the maximum intensity along the lines in AO-STEDD images.

6.4 Conclusions

Despite being an essential method for super-resolution imaging of biological structures, STED microscopy's effectiveness decreases dramatically for deep-tissue imaging applications. Several modal-based wavefront corrections that rely on the prolonged, frequent illumination of biological samples have been proposed in recent years to address this. In spite of the overall acceptable outcome, the main drawback of these approaches is that the depletion procedure often causes considerable phototoxicity and photobleaching [72,170].

As a remedy to this challenge, in this chapter, which was already published [72], a newly developed photon-efficient approach was proposed that enables effective deep 3D-STED imaging in biological samples through modal wavefront sensing. Based on this aberration correction protocol, zebrafish embryonic cells as a biological structure were mounted between the microscope coverslip and cover slide, which were coated with gold and fluorescent nanobeads as fiducial markers. By scattering imaging of gold markers, aberrated wavefronts of 2D and *z*-STED beams at zero depth (microscope coverslip) and 110 μm away (microscope cover slide) were assessed. Aberration investigation at the coverslip surface unveils system-induced aberration; deeper measurements at the microscope cover slide, on the other hand, uncover sample-induced wavefront distortions since it captures the microscope PSF after laser light passes through the immersion medium and biological specimens. As was already proved in the previous publication, to map the variation of aberration amplitude, a linear interpolation between these two points can be performed [72]. Furthermore, in this chapter, the time-based reproducibility of aberration correction parameters in a given sample was investigated. It was shown that the wavefront correction parameters remained stable for at least three consecutive days. This indicates that for long-term measurements, there is no need to repeatedly recalculate these parameters. In addition, by performing resolution calibration experiments on immobilized fluorescent beads and zebrafish embryonic imaging, it was demonstrated that interpolating the aberration data precisely corrects STED beam wavefronts at any intermediary measurement depth between the two glass surfaces, which resulted in a significantly enhanced resolution and signal-to-noise ratio compared to the experiments within great depths without adaptive optics. In short, this photon-efficient modal-based aberration correction method would enable high-quality imaging at deeper depths and extend the use of STED imaging to a larger variety of biological specimens.

Chapter 7: Summary and Outlook

With a special focus on DNA and transcriptional cluster architectures and spatial organization in zebrafish embryonic cells, several methods were developed in this PhD thesis to optimize multi-color 3D-STEDD fluorescence nanoscopy for the exploration of nanoscale structural organization and molecular interactions in various biological systems.

In Chapter 4, the refined background correction technique was developed to properly subtract the background at the pixel level even within highly challenging biological environments such as tightly labeled cell nuclei. In this chapter, it was found that, for compact fluorescent-labeled samples, the weighted subtraction between the signal plus background image and mostly background image should be performed rather locally and not globally based on the entire ROI at once. A sliding window-based method was developed to balance the background at the single-pixel level appropriately. This algorithm's performance was assessed by experimental measurements, which reached the conclusion that the optimal window size lies in a range between 1.0 and 1.5 of the confocal PSF for weighting factor estimation and thus for background subtraction. The results obtained by calculating the gamma factor locally and globally for background subtraction underlined the need to develop a local estimation method to prevent distortion in the images of biological samples during background correction and to interpret the measured data correctly.

In addition, the homemade STEDD microscope was employed in Chapter 5 to investigate the impact of various transcription inhibitors on gene regulation within embryonic cells of zebrafish. In addition to acquiring high-quality 3-color 3D data using background-free super-resolution imaging in this chapter, an analysis pipeline was developed to accurately segment clusters and classify them into different types, enabling the investigation of the effects of various transcription inhibitors on their morphological characteristics. This investigation allowed the study of the inhibitors' impacts on the three-dimensional spatial arrangement and morphology characteristics of transcriptional clusters, transcribed genes, and the surrounding bulk chromatin. The studies performed in this chapter were among some of the most interesting biological questions that could potentially result in the advancement of biomedical procedures.

Ultimately, in Chapter 6, a photon-efficient aberration correction method was developed to compensate for depletion beam wavefront aberrations, therefore enabling super-resolution imaging deep into thick biological specimens (≥ 100 μm). Using gold nanobeads as fiducial markers for aberration measurement, the current technique prevents significant light exposure and thereby lowers photobleaching. Then, by linear interpolation of the aberration parameters, wavefront correction at various depths was realized. Automated correction, shown for zebrafish embryos, considerably enhances image quality, especially for those nuclei located deep within cells (≥ 30 μm), by rectifying 2D- and *z*-STED beam distortions.

With continuous advances, particularly in wavefront aberration correction and data processing, STED fluorescence microscopy has become a fascinating technique whose complete potential may be explored in the near future. Based on the framework developed in this work, the outlook can be focused on excitation and detection beam aberration correction to further improve 3D-STEDD imaging capabilities. Furthermore, the aberration-corrected multicolor 3D-STED can be integrated with fluorescence correlation spectroscopy. Because of the significant spatial resolution enhancement, the combined approach allows precise measurements of the dynamics and interactions of molecules in nanoscale domains. This method is ideal for studying heterogeneity, diffusion, and interactions in subcellular structures like membranes or synaptic vesicles. Employing these modifications, this technology should ideally be more widely used and applied to solve intriguing biological problems and further the development of biomedicines.

A. References

1. He, G. S., Qin, H.-Y. & Zheng, Q. Rayleigh, Mie, and Tyndall scatterings of polystyrene microspheres in water: Wavelength, size, and angle dependences. *J. Appl. Phys.* **105**, (2009).

2. Kraemer, E. O. & Dexter, S. T. The light-scattering capacity (tyndall effect) and colloidal behavior of gelatine sols and gels. *J. Phys. Chem.* **31**, 764–782 (2002).

3. Kubitscheck, U. *Fluorescence Microscopy: From Principles to Biological Applications*. (John Wiley & Sons, 2017).

4. Pluta, M. Phase contrast microscopy. *Adv. Light Microsc.* **2**, (1993).

5. Niu, K. & Tian, C. Zernike polynomials and their applications. *J. Opt.* **24**, 123001 (2022).

6. Casasanta, C. V. Pioneers in Optics: Georges (Jerzy) Nomarski (1919–1997). *Micros. Today* **32**, 44–45 (2024).

7. Pluta, M. Nomarski's DIC microscopy: a review. *Phase contrast and differential interference contrast imaging techniques and applications* **1846**, 10–25 (1994).

8. Lang, W. *Nomarski Differential Interference-Contrast Microscopy*. (1982).

9. Redmond, R. W. Introduction to fluorescence and photophysics. in *Handbook of biomedical fluorescence* 1–28 (CRC Press, 2003).

10. Sanderson, M. J., Smith, I., Parker, I., *et al.* Fluorescence microscopy. *Cold Spring Harb. Protoc.* (2014).

11. Hedde, P. N. Light Microscopy Beyond the Diffraction Barrier for Live Cell Studies. (Karlsruhe Institute of Technology, 2013).

12. Leeder, J. M., Bradshaw, D. S., Williams, M. D., *et al.* Developments in the Photonic Theory of Fluorescence. in *Reviews in Fluorescence 2015,* vol. 8 235–268 (Springer, 2016).

13. Rath, J. Charakterisierung von Interaktionen der Rezeptoren und Liganden im Wnt-Signalweg mittels Fluoreszenzmikroskopie. (Karlsruhe Institute of Technology, 2022).

14. Prunsche, B. Höchstaufgelöste optische Nanoskopie und Fluktuationsspektroskopie zur Untersuchung biophysikalischer Prozesse. (Karlsruhe Institute of Technology, 2018).

15. Limpouchová, Z. & Procházka, K. Theoretical principles of fluorescence spectroscopy. in *Fluorescence Studies of Polymer Containing Systems* 91–149 (Springer, 2016).

16. Condon, E. U. The Franck-Condon principle and related topics. *Am. J. Phys.* **15**, 365–374 (1947).

17. Lakowicz, J. R. *Principles of Fluorescence Spectroscopy*. (Springer, 2006).

18. Stokes, G. G. On the change of refrangibility of light. in *Abstracts of the Papers Communicated to the Royal Society of London* 195–200 (The Royal Society London, 1854).

19. Samanta, A. Dynamic stokes shift and excitation wavelength dependent fluorescence of dipolar molecules in room temperature ionic liquids. *J. Phys. Chem. B* **110**, 13704–13716 (2006).

20. Staudt, T. M. Strategies to Reduce Photobleaching, Dark State Transitions and Phototoxicity in Subdiffraction Optical Microscopy. (University of Heidelberg, 2009).

21. Eggeling, C., Widengren, J., Rigler, R., *et al.* Photobleaching of fluorescent dyes under conditions used for single-molecule detection: evidence of two-step photolysis. *Anal. Chem.* **70**, 2651–2659 (1998).

22. Wüstner, D., Christensen, T., Solanko, L. M., *et al.* Photobleaching kinetics and time-integrated emission of fluorescent probes in cellular membranes. *Molecules* **19**, 11096–11130 (2014).

23. Song, L., Varma, C. A., Verhoeven, J. W., *et al.* Influence of the triplet excited state on the photobleaching kinetics of fluorescein in microscopy. *Biophys. J.* **70**, 2959–2968 (1996).

24. Rao, J., Dragulescu-Andrasi, A. & Yao, H. Fluorescence imaging in vivo: recent advances. *Curr. Opin. Biotechnol.* **18**, 17–25 (2007).

25. Jeong, S., Widengren, J. & Lee, J.-C. Fluorescent probes for STED optical nanoscopy. *Nanomaterials* **12**, 21–38 (2021).

26. Xu, R., Xu, Y., Wang, Z., *et al.* Recent advances on organic fluorescent probes for stimulated emission depletion (STED) microscopy. *Comb. Chem. High Throughput Screen.* **24**, 1017–1030 (2021).

27. Wang, F., Tan, W. B., Zhang, Y., *et al.* Luminescent nanomaterials for biological labelling. *Nanotechnology* **17**, R1 (2005).

28. Alivisatos, A. P. Semiconductor clusters, nanocrystals, and quantum dots. *Science (1979)* **271**, 933–937 (1996).

29. Michalet, X., Pinaud, F. F., Bentolila, L. A., *et al.* Quantum dots for live cells, in vivo imaging, and diagnostics. *Science (1979)* **307**, 538–544 (2005).

30. Shimomura, O., Johnson, F. H. & Saiga, Y. Extraction, purification and properties of aequorin, a bioluminescent protein from the luminous hydromedusan, Aequorea. *J. Cell. Comp. Physiol.* **59**, 223–239 (1962).

31. Jendrossek, D. Fluorescence microscopical investigation of poly (3-hydroxybutyrate) granule formation in bacteria. *Biomacromolecules* **6**, 598–603 (2005).

32. Nishida, J., Masuko, T., Cui, Y., *et al.* Molecular design of organic dye toward retardation of charge recombination at semiconductor/dye/electrolyte interface: introduction of twisted π-linker. *J. Phys. Chem. C* **114**, 17920–17925 (2010).

33. Hoeben, F. J. M., Jonkheijm, P., Meijer, E. W., *et al.* About supramolecular assemblies of π-conjugated systems. *Chem. Rev.* **105**, 1491–1546 (2005).

34. Lakowicz, J. R. *Introduction to Fluorescence*. *Principles of fluorescence spectroscopy* (Springer, 1999).

35. Pancholi, A., Klingberg, T., Zhang, W., *et al.* RNA polymerase II clusters form in line with surface condensation on regulatory chromatin. *Mol. Syst. Biol.* **17**, e10272 (2021).

36. Wurm, C. A., Neumann, D., Schmidt, R., *et al.* Sample preparation for STED microscopy. *Live Cell Imaging: Methods and Protocols* 185–199 (2010).

37. Van de Linde, S., Löschberger, A., Klein, T., *et al.* Direct stochastic optical reconstruction microscopy with standard fluorescent probes. *Nat. Protoc.* **6**, 991–1009 (2011).

38. Se-yuen, M. A closer look at Fermat's principle. *Phys. Educ.* **21**, 365 (1986).

39. Golomb, M. Elementary proofs for the equivalence of Fermat's principle and Snell's law. *Am. Math. Mon.* **71**, 541–543 (1964).

40. Saleh, B. E. A. & Teich, M. C. *Fundamentals of Photonics*. (John Wiley & Sons, 2019).

41. Abbe, E. Beiträge zur Theorie des Mikroskops und der mikroskopischen Wahrnehmung. *Arch. Mikrosk. Anat.* **9**, 413–468 (1873).

42. White, J. G., Amos, W. B. & Fordham, M. An evaluation of confocal versus conventional imaging of biological structures by fluorescence light microscopy. *J. Cell Biol.* **105**, 41–48 (1987).

43. Conchello, J.-A. & Lichtman, J. W. Optical sectioning microscopy. *Nat. Methods* **2**, 920–931 (2005).

44. Minsky, M. Microscopy apparatus US patent 3013467. *USP Office, Ed. US* **658**, (1961).

45. Hell, S. W. & Wichmann, J. Breaking the diffraction resolution limit by stimulated emission: stimulated-emission-depletion fluorescence microscopy. *Opt. Lett.* **19**, 780–782 (1994).

46. Klar, T. A., Jakobs, S., Dyba, M., *et al.* Fluorescence microscopy with diffraction resolution barrier broken by stimulated emission. *Proc. Natl. Acad. Sci. U.S.A.* **97**, 8206–8210 (2000).

47. Pawley, J. *Handbook of Biological Confocal Microscopy*. (Springer Science & Business Media, 2006).

48. Wilhelm, S. *Zeiss Confocal Principles*. (2012).

49. Hopkins, H. H. The Airy disc formula for systems of high relative aperture. *Proc. Phys. Soc.* **55**, 116 (1943).

50. Richards, B. & Wolf, E. Electromagnetic diffraction in optical systems, II. Structure of the image field in an aplanatic system. *Proc. R. Soc. Lond. A Math. Phys. Sci.* **253**, 358–379 (1959).

51. Caprile, F., Masullo, L. A. & Stefani, F. D. PyFocus–a Python package for vectorial calculations of focused optical fields under realistic conditions. Application to toroidal foci. *Comput. Phys. Commun.* **275**, 108315 (2022).

52. Lin, J., Rodríguez-Herrera, O. G., Kenny, F., *et al.* Fast vectorial calculation of the volumetric focused field distribution by using a three-dimensional Fourier transform. *Opt. Express* **20**, 1060–1069 (2012).

53. Binnig, G., Quate, C. F. & Gerber, C. Atomic force microscope. *Phys. Rev. Lett.* **56**, 930 (1986).

54. Ruska, E. The development of the electron microscope and of electron microscopy. *Rev. Mod. Phys.* **59**, 627 (1987).

55. Graham, L. & Orenstein, J. M. Processing tissue and cells for transmission electron microscopy in diagnostic pathology and research. *Nat. Protoc.* **2**, 2439–2450 (2007).

56. Afanasyev, S. S., Kychkina, T. V & Savvinova, L. N. Scanning electron microscope (advantages and disadvantages). in *Colloquium-journal* 25–27 (Голопристанський міськрайонний центр зайнятості, 2019).

57. Vogelsang, J., Steinhauer, C., Forthmann, C., *et al.* Make them blink: Probes for super-resolution microscopy. *ChemPhysChem* **11**, 2475–2490 (2010).

58. Bates, M., Huang, B. & Zhuang, X. Super-resolution microscopy by nanoscale localization of photo-switchable fluorescent probes. *Curr. Opin. Chem. Biol.* **12**, 505–514 (2008).

59. Henriques, R., Griffiths, C., Hesper Rego, E., *et al.* PALM and STORM: unlocking live-cell super-resolution. *Biopolymers* **95**, 322–331 (2011).

60. Fang, Y., Kuang, C., Ma, Y., *et al.* Resolution and contrast enhancements of optical microscope based on point spread function engineering. *Front. Optoelectron.* **8**, 152–162 (2015).

61. Hell, S. W. Increasing the resolution of far-field fluorescence light microscopy by point-spread-function engineering. in *Topics in Fluorescence Spectroscopy: Volume 5: Nonlinear and Two-Photon-Induced Fluorescence* 361–426 (Springer, 2002).

62. Hell, S. W. & Wichmann, J. Breaking the diffraction resolution limit by stimulated emission: stimulated-emission-depletion fluorescence microscopy. *Opt. Lett.* **19**, 780–782 (1994).

63. Hell, S. W. Far-field optical nanoscopy. *Science (1979)* **316**, 1153–1158 (2007).

64. Horstmann, N. Light amplification by stimulated emission of radiation. *Phys. Inform. Technol.* 1–4 (2002).

65. Gao, P. & Nienhaus, G. U. Precise background subtraction in stimulated emission double depletion nanoscopy. *Opt. Lett.* **42**, 831–834 (2017).

66. Xie, H., Liu, Y., Jin, D., *et al.* Analytical description of high-aperture STED resolution with 0–2π vortex phase modulation. *JOSA A* **30**, 1640–1645 (2013).

67. Yang, H., Zhang, Y., Xiao, Y., *et al.* Generation and comparison of donut-shaped depletion beams in STED microscopy. *Optics* **127**, 3735–3739 (2016).

68. Chen, J., Chen, X., Yang, H., *et al.* Simulation of stimulated emission depletion intensity distribution by scalar integral. in *Optics in Health Care and Biomedical Optics VI* vol. 9268 291–297 (SPIE, 2014).

69. Wang, R. STED-Fluorescence Correlation Spectroscopy for Dynamic Observations in Cell Biology: from Theoretical to Practical Approaches. (Aix-Marseille University, 2018).

70. Harke, B. 3D STED Microscopy with Pulsed and Continuous Wave Lasers. (Georg-August-Universität Göttingen, 2008).

71. Barati Sedeh, A., Kobitski, A., Dai, S., *et al.* Stimulated emission double depletion nanoscopy with background correction at the single-pixel level. *Opt. Lett.* **48**, 5791–5794 (2023).

72. Dai, S., Kobitski, A., Barati Sedeh, A., *et al.* Photon-Efficient Aberration Correction for 3D-STED Imaging of Thick Biological Specimens Using Sensorless Adaptive Optics. *ACS Photonics* **11**, 310–320 (2024).

73. Gao, P., Prunsche, B., Zhou, L., *et al.* Background suppression in fluorescence nanoscopy with stimulated emission double depletion. *Nat. Photonics* **11**, 163–169 (2017).

74. Lee, J.-C., Ma, Y., Han, K. Y., *et al.* Accurate background subtraction in STED nanoscopy by polarization switching. *ACS Photonics* **6**, 1789–1797 (2019).

75. Deng, S., Liu, L., Cheng, Y., *et al.* Effects of primary aberrations on the fluorescence depletion patterns of STED microscopy. *Opt. Express* **18**, 1657–1666 (2010).

76. Ghosh, D. Automated Aberration Correction for STED Microscopy. (Georg-August University School of Science, 2023).

77. Schwiegerling, J. Review of Zernike polynomials and their use in describing the impact of misalignment in optical systems. in *Optical System Alignment, Tolerancing, and Verification XI* vol. 10377 74–81 (SPIE, 2017).

78. Antonello, J., Burke, D. & Booth, M. J. Aberrations in stimulated emission depletion (STED) microscopy. *Opt. Commun.* **404**, 203–209 (2017).

79. Hao, X., Kuang, C., Wang, T., *et al.* Effects of polarization on the de-excitation dark focal spot in STED microscopy. *J. Opt.* **12**, 115707 (2010).

80. Lazarev, G., Hermerschmidt, A., Krüger, S., *et al.* LCOS spatial light modulators: trends and applications. *Optical Imaging and Metrology: Advanced Technologies* 1–29 (2012).

81. Yang, Y., Forbes, A. & Cao, L. A review of liquid crystal spatial light modulators: devices and applications. *Opto-Electron. Sci.* **2**, 230021–230026 (2023).

82. Matsumoto, N., Ando, T., Inoue, T., *et al.* Generation of high-quality higher-order Laguerre-Gaussian beams using liquid-crystal-on-silicon spatial light modulators. *JOSA A* **25**, 1642–1651 (2008).

83. Gould, T. J., Burke, D., Bewersdorf, J., *et al.* Adaptive optics enables 3D STED microscopy in aberrating specimens. *Opt. Express* **20**, 20998–21009 (2012).

84. Yang Cui. Implementation of a Spatial Light Modulator to Enable Gaussian and Bessel Beam Illumination on a Digital Scanned Laser Light Sheet Microscope. (Karlsruhe Institute of Technology, 2017).

85. Li, R. & Cao, L. Progress in phase calibration for liquid crystal spatial light modulators. *Appl. Sci.* **9**, 2012 (2019).

86. Prunsche, B. Integration und Anwendung adaptiver Optiken in einem STED Mikroskop zur Untersuchung biophysikalischer Prozesse. (Karlsruhe Institute of Technology, 2015).

87. Harke, B., Keller, J., Ullal, C. K., *et al.* Resolution scaling in STED microscopy. *Opt. Express* **16**, 4154–4162 (2008).

88. Hanne, J., Falk, H. J., Görlitz, F., *et al.* STED nanoscopy with fluorescent quantum dots. *Nat. Commun.* **6**, 7127 (2015).

89. Ma, Y. & Ha, T. Fight against background noise in stimulated emission depletion nanoscopy. *Phys. Biol.* **16**, 051002 (2019).

90. Vicidomini, G., Moneron, G., Han, K. Y., *et al.* Sharper low-power STED nanoscopy by time gating. *Nat. Methods* **8**, 571–573 (2011).

91. Lanzanò, L., Coto Hernández, I., Castello, M., *et al.* Encoding and decoding spatio-temporal information for super-resolution microscopy. *Nat. Commun.* **6**, 6701 (2015).

92. Castello, M., Diaspro, A. & Vicidomini, G. Multi-images deconvolution improves signal-to-noise ratio on gated stimulated emission depletion microscopy. *Appl. Phys. Lett.* **105**, 234106 (2014).

93. Vicidomini, G., Moneron, G., Eggeling, C., *et al.* STED with wavelengths closer to the emission maximum. *Opt. Express* **20**, 5225–5236 (2012).

94. Vicidomini, G., Schönle, A., Ta, H., *et al.* STED nanoscopy with time-gated detection: theoretical and experimental aspects. *PLoS One* **8**, e54421 (2013).

95. Tu, S., Liu, X., Yuan, D., *et al.* Accurate Background Reduction in Adaptive Optical Three-Dimensional Stimulated Emission Depletion Nanoscopy by Dynamic Phase Switching. *ACS Photonics* **9**, 3863–3868 (2022).

96. Cai, F. & Verbeek, F. J. Dam-based rolling ball with fuzzy-rough constraints, a new background subtraction algorithm for image analysis in microscopy. in *2015 International Conference on Image Processing Theory, Tools and Applications (IPTA)* 298–303 (IEEE, 2015).

97. Han, G., Wang, J. & Cai, X. Background subtraction based on three-dimensional discrete wavelet transform. *Sensors* **16**, 456 (2016).

98. Galloway, C. M., Le Ru, E. C. & Etchegoin, P. G. An iterative algorithm for background removal in spectroscopy by wavelet transforms. *Appl. Spectrosc.* **63**, 1370–1376 (2009).

99. Hüpfel, M., Yu. Kobitski, A., Zhang, W., *et al.* Wavelet-based background and noise subtraction for fluorescence microscopy images. *Biomed. Opt. Express* **12**, 969–980 (2021).

100. Vermeulen, P., Zhan, H., Orieux, F., *et al.* Out-of-focus background subtraction for fast structured illumination super-resolution microscopy of optically thick samples. *J. Microsc.* **259**, 257–268 (2015).

101. Vicidomini, G., Moneron, G., Eggeling, C., *et al.* STED with wavelengths closer to the emission maximum. *Opt. Express* **20**, 5225–5236 (2012).

102. Kastrup, L., Blom, H., Eggeling, C., *et al.* Fluorescence fluctuation spectroscopy in subdiffraction focal volumes. *Phys. Rev. Lett.* **94**, 178104 (2005).

103. You, S., Kuang, C., Rong, Z., *et al.* Eliminating deformations in fluorescence emission difference microscopy. *Opt. Express* **22**, 26375–26385 (2014).

104. Leray, A., Lillis, K. & Mertz, J. Enhanced background rejection in thick tissue with differential-aberration two-photon microscopy. *Biophys. J.* **94**, 1449–1458 (2008).

105. Dehez, H., Piché, M. & De Koninck, Y. Resolution and contrast enhancement in laser scanning microscopy using dark beam imaging. *Opt. Express* **21**, 15912–15925 (2013).

106. Martell, D. J., Merens, H. E., Caulier, A., *et al.* RNA polymerase II pausing temporally coordinates cell cycle progression and erythroid differentiation. *Dev. Cell* **58**, 2112–2127 (2023).

107. Richter, W. F., Nayak, S., Iwasa, J., *et al.* The Mediator complex as a master regulator of transcription by RNA polymerase II. *Nat Rev Mol Cell Biol* **23**, 732–749 (2022).

108. Liu, X., Kraus, W. L. & Bai, X. Ready, pause, go: regulation of RNA polymerase II pausing and release by cellular signaling pathways. *Trends Biochem. Sci.* **40**, 516–525 (2015).

109. Martell, D. J., Merens, H. E., Caulier, A., *et al.* RNA polymerase II pausing temporally coordinates cell cycle progression and erythroid differentiation. *Dev. Cell* **58**, 2112–2127 (2023).

110. Castells-Garcia, A., Ed-Daoui, I., González-Almela, E., *et al.* Super resolution microscopy reveals how elongating RNA polymerase II and nascent RNA interact with nucleosome clutches. *Nucleic Acids Res.* **50**, 175–190 (2022).

111. Nienhaus, K. & Nienhaus, G. U. Where do we stand with super-resolution optical microscopy? *J. Mol. Biol.* **428**, 308–322 (2016).

112. Li, J., Dong, A., Saydaminova, K., *et al.* Single-molecule nanoscopy elucidates RNA polymerase II transcription at single genes in live cells. *Cell* **178**, 491–506 (2019).

113. Li, J., Hsu, A., Hua, Y., *et al.* Single-gene imaging links genome topology, promoter–enhancer communication and transcription control. *Nat. Struct. Mol. Biol.* **27**, 1032–1040 (2020).

114. Forero-Quintero, L. S., Raymond, W., Handa, T., *et al.* Live-cell imaging reveals the spatiotemporal organization of endogenous RNA polymerase II phosphorylation at a single gene. *Nat. Commun.* **12**, 3158 (2021).

115. Ohishi, H., Shimada, S., Uchino, S., *et al.* STREAMING-tag system reveals spatiotemporal relationships between transcriptional regulatory factors and transcriptional activity. *Nat. Commun.* **13**, 7672 (2022).

116. Pownall, M. E., Miao, L., Vejnar, C. E., *et al.* Chromatin expansion microscopy reveals nanoscale organization of transcription and chromatin. *Science (1979)* **381**, 92–100 (2023).

117. Du, M., Stitzinger, S. H., Spille, J.-H., *et al.* Direct observation of a condensate effect on super-enhancer controlled gene bursting. *Cell* **187**, 331–344 (2024).

118. Aleström, P., D'Angelo, L., Midtlyng, P. J., *et al.* Zebrafish: Housing and husbandry recommendations. *Lab. Anim.* **54**, 213–224 (2020).

119. Lawrence, C. Advances in zebrafish husbandry and management. *Methods Cell Biol.* **104**, 429–451 (2011).

120. MATLAB (Version R2023a). Preprint at https://www.mathworks.com/products/matlab.html.

121. Schindelin, J., Arganda-Carreras, I., Frise, E., *et al.* Fiji: an open-source platform for biological-image analysis. *Nat. Methods* **9**, 676–682 (2012).

122. Pieper, S., Halle, M. & Kikinis, R. 3D Slicer. in *2004 2nd IEEE international symposium on biomedical imaging: nano to macro (IEEE Cat No. 04EX821)* 632–635 (IEEE, 2004).

123. Ester, M., Kriegel, H.-P., Sander, J., *et al.* A density-based algorithm for discovering clusters in large spatial databases with noise. in *KDD* vol. 96 226–231 (1996).

124. Veldman, M. B. & Lin, S. Zebrafish as a developmental model organism for pediatric research. *Pediatr. Res.* **64**, 470–476 (2008).

125. Zon, L. I. & Peterson, R. T. In vivo drug discovery in the zebrafish. *Nat. Rev. Drug Discov.* **4**, 35–44 (2005).

126. Howe, K., Clark, M. D., Torroja, C. F., *et al.* The zebrafish reference genome sequence and its relationship to the human genome. *Nature* **496**, 498–503 (2013).

127. Eick, D. & Geyer, M. The RNA polymerase II carboxy-terminal domain (CTD) code. *Chem. Rev.* **113**, 8456–8490 (2013).

128. Cramer, P. Organization and regulation of gene transcription. *Nature* **573**, 45–54 (2019).

129. Fuda, N. J., Ardehali, M. B. & Lis, J. T. Defining mechanisms that regulate RNA polymerase II transcription in vivo. *Nature* **461**, 186–192 (2009).

130. Pei, G., Lyons, H., Li, P., *et al.* Transcription regulation by biomolecular condensates. *Nat. Rev. Mol. Cell Biol.* 1–24 (2024).

131. Adelman, K. & Lis, J. T. Promoter-proximal pausing of RNA polymerase II: emerging roles in metazoans. *Nat. Rev. Genet.* **13**, 720–731 (2012).

132. Efroni, S., Duttagupta, R., Cheng, J., *et al.* Global transcription in pluripotent embryonic stem cells. *Cell Stem Cell* **2**, 437–447 (2008).

133. Klingberg, T., Wachter, I., Pancholi, A., *et al.* Transcriptional clusters follow a conserved condensation-dispersal sequence during stem cell differentiation. *bioRxiv* 2023–2027 (2023).

134. Boija, A., Klein, I. A., Sabari, B. R., *et al.* Transcription factors activate genes through the phase-separation capacity of their activation domains. *Cell* **175**, 1842–1855 (2018).

135. Shao, W., Bi, X., Pan, Y., *et al.* Phase separation of RNA-binding protein promotes polymerase binding and transcription. *Nat. Chem. Biol.* **18**, 70–80 (2022).

136. Kimura, H., Sugaya, K. & Cook, P. R. The transcription cycle of RNA polymerase II in living cells. *J. Cell Biol.* **159**, 777–782 (2002).

137. Stasevich, T. J., Hayashi-Takanaka, Y., Sato, Y., *et al.* Regulation of RNA polymerase II activation by histone acetylation in single living cells. *Nature* **516**, 272–275 (2014).

138. Steurer, B., Janssens, R. C., Geverts, B., *et al.* Live-cell analysis of endogenous GFP-RPB1 uncovers rapid turnover of initiating and promoter-paused RNA Polymerase II. *Proc. Natl. Acad. Sci. U.S.A.* **115**, 4368–4376 (2018).

139. Maston, G. A., Zhu, L. J., Chamberlain, L., *et al.* Non-canonical TAF complexes regulate active promoters in human embryonic stem cells. *Elife* **1**, 68–87 (2012).

140. Heng, J.-C. D. & Ng, H.-H. Transcriptional regulation in embryonic stem cells. in *Cell Biol. Stem Cells* vol. 695 76–91 (Springer, 2010).

141. Le, D. J., Hafner, A., Gaddam, S., *et al.* Super-enhancer interactomes from single cells link clustering and transcription. *bioRxiv* (2024).

142. Bosnali, M., Münst, B., Thier, M., *et al.* Deciphering the stem cell machinery as a basis for understanding the molecular mechanism underlying reprogramming. *Cell. Mol. Life Sci.* **66**, 3403–3420 (2009).

143. Julian, L. M. & Blais, A. Transcriptional control of stem cell fate by E2Fs and pocket proteins. *Front Genet* **6**, 161 (2015).

144. Wang, X., Fan, Y. & Wu, Q. The regulation of transcription elongation in embryonic stem cells. *Front. Cell Dev. Biol.* **11**, 1145611 (2023).

145. Zhao, Z. W., Roy, R., Gebhardt, J. C. M., *et al.* Spatial organization of RNA polymerase II inside a mammalian cell nucleus revealed by reflected light-sheet superresolution microscopy. *Proc. Natl. Acad. Sci. U.S.A.* **111**, 681–686 (2014).

146. Hnisz, D., Abraham, B. J., Lee, T. I., *et al.* Super-enhancers in the control of cell identity and disease. *Cell* **155**, 934–947 (2013).

147. Filippakopoulos, P., Qi, J., Picaud, S., *et al.* Selective inhibition of BET bromodomains. *Nature* **468**, 1067–1073 (2010).

148. Chapuy, B., McKeown, M. R., Lin, C. Y., *et al.* Discovery and characterization of super-enhancer-associated dependencies in diffuse large B cell lymphoma. *Cancer Cell* **24**, 777–790 (2013).

149. Zaware, N. & Zhou, M.-M. Chemical modulators for epigenome reader domains as emerging epigenetic therapies for cancer and inflammation. *Curr. Opin. Chem. Biol.* **39**, 116–125 (2017).

150. Düster, R., Kaltheuner, I. H., Schmitz, M., *et al.* 1, 6-Hexanediol, commonly used to dissolve liquid–liquid phase separated condensates, directly impairs kinase and phosphatase activities. *J. Biol. Chem.* **296**, (2021).

151. Elbaum-Garfinkle, S. Matter over mind: Liquid phase separation and neurodegeneration. *J. Biol. Chem.* **294**, 7160–7168 (2019).

152. Alberti, S., Gladfelter, A. & Mittag, T. Considerations and challenges in studying liquid-liquid phase separation and biomolecular condensates. *Cell* **176**, 419–434 (2019).

153. Shulga, N. & Goldfarb, D. S. Binding dynamics of structural nucleoporins govern nuclear pore complex permeability and may mediate channel gating. *Mol. Cell. Biol.* **23**, 534–542 (2003).

154. Chen, F., Gao, X. & Shilatifard, A. Stably paused genes revealed through inhibition of transcription initiation by the TFIIH inhibitor triptolide. *Genes Dev.* **29**, 39–47 (2015).

155. Chen, R., Keating, M. J., Gandhi, V., *et al.* Transcription inhibition by flavopiridol: mechanism of chronic lymphocytic leukemia cell death. *Blood* **106**, 2513–2519 (2005).

156. Chao, S.-H., Fujinaga, K., Marion, J. E., *et al.* Flavopiridol inhibits P-TEFb and blocks HIV-1 replication. *J. Biol. Chem.* **275**, 28345–28348 (2000).

157. Lam, L. T., Pickeral, O. K., Peng, A. C., *et al.* Genomic-scale measurement of mRNA turnover and the mechanisms of action of the anti-cancer drug flavopiridol. *Genome Biol.* **2**, 1–11 (2001).

158. Carlson, B., Pearlstein, R., Naik, R., *et al.* Inhibition of CDK2, CDK4 and CDK7 by flavopiridol and structural analogs. in *Proc Am Assoc Cancer Res* vol. 37 424 (1996).

159. Jiang, G., Deng, W., Liu, Y., *et al.* General mechanism of JQ1 in inhibiting various types of cancer. *Mol. Med. Rep.* **21**, 1021–1034 (2020).

160. Shin, Y., Chang, Y.-C., Lee, D. S. W., *et al.* Liquid nuclear condensates mechanically sense and restructure the genome. *Cell* **175**, 1481–1491 (2018).

161. Quail, T., Golfier, S., Elsner, M., *et al.* Force generation by protein–DNA co-condensation. *Nat. Phys.* **17**, 1007–1012 (2021).

162. Gouveia, B., Kim, Y., Shaevitz, J. W., *et al.* Capillary forces generated by biomolecular condensates. *Nature* **609**, 255–264 (2022).

163. Strom, A. R., Kim, Y., Zhao, H., *et al.* Condensate interfacial forces reposition DNA loci and probe chromatin viscoelasticity. *Cell* **187**, 5282–5297 (2024).

164. Patton, B. R., Burke, D., Owald, D., *et al.* Three-dimensional STED microscopy of aberrating tissue using dual adaptive optics. *Opt. Express* **24**, 8862–8876 (2016).

165. Zdankowski, P., McGloin, D. & Swedlow, J. R. Full volume super-resolution imaging of thick mitotic spindle using 3D AO STED microscope. *Biomed. Opt. Express* **10**, 1999–2009 (2019).

166. Zdankowski, P., Trusiak, M., McGloin, D., *et al.* Numerically enhanced stimulated emission depletion microscopy with adaptive optics for deep-tissue super-resolved imaging. *ACS Nano* **14**, 394–405 (2019).

167. Hao, X., Allgeyer, E. S., Lee, D.-R., *et al.* Three-dimensional adaptive optical nanoscopy for thick specimen imaging at sub-50-nm resolution. *Nat. Methods* **18**, 688–693 (2021).

168. Barbotin, A., Galiani, S., Urbančič, I., *et al.* Adaptive optics allows STED-FCS measurements in the cytoplasm of living cells. *Opt. Express* **27**, 23378–23395 (2019).

169. Facomprez, A., Beaurepaire, E. & Débarre, D. Accuracy of correction in modal sensorless adaptive optics. *Opt. Express* **20**, 2598–2612 (2012).

170. Donnert, G., Keller, J., Medda, R., *et al.* Macromolecular-scale resolution in biological fluorescence microscopy. *Proc. Natl. Acad. Sci. U.S.A.* **103**, 11440–11445 (2006).

171. Richards, B. & Wolf, E. Electromagnetic diffraction in optical systems, II. Structure of the image field in an aplanatic system. *Proc. R. Soc. Lond. A Math. Phys. Sci.* **253**, 358–379 (1959).

172. Wolf, E. Electromagnetic diffraction in optical systems-I. An integral representation of the image field. *Proc. R. Soc. Lond. A Math. Phys. Sci.* **253**, 349–357 (1959).

173. Barati Sedeh, A., Kobitski, A., Nienhaus, K., *et al.* 3-color STEDD nanoscopy reveals transcriptional cluster nano-architectures that manage chromatin access for transcription control. *In the submission process* (2025).

During the writing process, large language models (Grammarly and ChatGPT) were used to enhance grammar and clarity. These tools were used solely to assist in polishing the author's original writing and did not contribute to generating material. The final version has been thoroughly reviewed and edited, and full responsibility for its content rests with the doctoral candidate.

B. Appendix

B.1. Detailed Explanation of the Spatial System Alignment Procedure

The alignment of 3-color STEDD microscopy is laborious and precise work since all excitation and depletion beams have to overlay with almost 50 nm precision both laterally and axially. First, one overlays the excitation beams at the center of the microscope entrance and nosepiece. This means that two checkpoints are chosen, one at the entrance of the body microscope and one at the back aperture of the objective lens, to ensure that the excitation beams align on top of each other and illuminate the objective back aperture perpendicularly. Two pinholes (DG10-1500-H1-MD - Ø1" SM1-Mounted Frosted Glass, Thorlabs, Germany) are installed at the aforementioned checkpoints in order to observe the position of the beam. When all beams show the same misalignment, shared excitation mirrors correct it. If beams misalign independently, their individual mirrors correct the misalignment without compromising the shared path. After an alignment by sight, two cameras (Zelux 1.6 MP monochrome CMOS camera, Thorlabs, Germany) are used: one at the objective back aperture and the other before the galvanometer scanner, to more precisely coalesce the beams. Finer alignments are performed using these two reference points. Following these steps, one ensures that all the excitation beams co-align to illuminate the back aperture of the objective lens perpendicularly at the center. It is mentioned that if shared excitation mirrors are used in the excitation laser alignment, appropriate alignments of mirrors exclusively placed in the detection path must be performed. This is due to the fact that the emitted photons from the sample propagate toward the detection path by being reflected from the mirrors in the excitation-shared path.

Afterward, the STEDD beam, along with the modulated beams from both SLMs, which form donut and cylinder PSFs, aligns on the depletion cage system. To achieve this, two pinhole targets (CPA1- Ø0.9 mm hole, Thorlabs, Germany) are placed at the beginning and ending points of the cage system in each depletion beam path (see Figure 3.1). Using SLM mounts and mirrors, the modulated beams from the SLMs align at the center of the targets. This step ensures that the depletion beams align on top of each other, propagating parallel to the optical axis. Consequently, all three depletion beams align with the excitation beams using shared depletion mirrors (see Figure 3.2). This alignment is monitored with cameras, one placed before the galvanometric scanner and the other at the objective nosepiece.

Correcting the donut and cylinder beam intensity profiles on the camera at the sample plane comes next, once all beams are co-aligned at the center of the objective nosepiece. This step

guarantees that the rebuilt profiles show homogeneous intensity all around the center zeros. Computationally shifting the pattern on the SLM helps to get as close as possible to the ideal intensity distribution by overlapping the laser beam and pattern on top of each other.

Another manipulation related to this, therefore, is polarization alignment in the path of the donut beam. The donut profile achieves nearly zero intensity at the center when the beam and the physical vortex plate has the same helicity. Thus, in the home-built system, a circularly polarized beam with a right-hand orientation develops by the use of a combination of half- and quarter-wave plates.

Following these steps results in the accurate co-alignment of all beams, which is guided by the scattering imaging of gold nanobeads. If necessary, one of the excitation beam point spread functions (PSFs) serves as a reference, while all other beams are carefully co-aligned laterally and axially. In case axial realignment is required, this is performed by changing the lens positions in the Keplerian expander system in front of the fiber coupler for every laser beam (see Figure 3.2).

B.2. Detailed Description of the Immunofluorescence Staining of Zebrafish Embryo Whole Animal Cap Procedure for 3 Color-3D STEDD Microscopy

Modified according to the protocol provided by Prof. Dr. Lennart Hilbert in May 2021 [35].

Attention: When removing liquid during each stage, use a P1000 or P200 pipette while working under the stereoscope. It is possible to observe the unintentional extraction of embryos (or animal caps) and subsequently reinsert them into the tube.

Hint: For all subsequent procedures following formaldehyde fixation (except Triton X-100 treatment), the embryos can be refrigerated for a few days or even over the weekend. This provides a certain degree of adaptability when it comes to organizing and managing the schedule.

Step 1: Zebrafish husbandry and embryo collection

1-1) Retrieve fertilized embryos following the mating process.

1-2) To eliminate the chorion, use a pronase treatment. Afterwards, use only glass pipettes and agarose-coated plastic plates.

1-3) Place the embryos in 0.3X Danieau's medium at a temperature of 28.5°C until the fixation step. Monitor any injured embryos closely and remove them.

Step 2: Fixation and preparation of embryonic animal caps

2-1) Fix embryos by transferring them into 2 ml round-bottom microcentrifuge tubes that contain 0.3X Danieau's medium with 2% formaldehyde and 0.2% Tween-20.

2-2) Allow to rest for 30–60 minutes at room temperature (if this is inconvenient, consider refrigerating overnight as an alternative).

2-3) Apply 200–300 µl of 0.5% Triton X-100 in Dulbecco's PBS to increase permeability (for 15 minutes at room temperature).

2-4) After 15 minutes, precisely add one milliliter of PBST (Dulbecco's PBS with 0.1% Tween-20) into the Triton X-100 mixture.

2-5) Transfer the embryos from the microcentrifuge tube into a glass petri dish with PBST.

2-6) Remove the yolk using fine forceps.

2-7) Transfer the remaining animal caps back into fresh, empty microcentrifuge tubes.

2-8) Wash once more with PBST and wait at least 10 minutes with samples at room temperature.

2-9) Block with 4% BSA in PBST for 30 minutes or longer at room temperature.

2-10) After 30 minutes, remove 4% BSA down to ~100 µl left in the tube and ensure the volume left over is more or less the same in all tubes.

Step 3: **Primary antibody staining:**

3-1) Sum up all the 100 µl volumes of all samples that should get the antibody, then calculate how much antibody stock needs to be added to that volume to reach the desired concentration. Spike these amounts of antibody in a tube with a volume of 5 µl 4% BSA-PBST per sample to stain, mix well, and add 5 µl of this mix to every tube that should be stained. A 1:300 dilution of primary antibodies was used, namely EPR18855 (Rabbit IgG, Abcam, Cat. No. ab193468) and 3E8 (Rat IgG, Active Motif, Cat. No. 61986), to target the Pol II Ser2P and Pol II Ser5P structures, respectively. In other words, 3.3 µl of each primary antibody was added to 1000 µl of 4% BSA-PBST. Afterward, 150 µl of this mixture was added to each tube containing animal caps.

3-2) Incubate in the fridge overnight.

3-3) Wash three times with PBST; each time, wait at least 10 minutes with samples at room temperature.

3-4) Wash one time with 4% BSA-PBST and remove precisely down to 100 µl left in every sample.

Step 4: **Secondary antibody staining:**

4-1) Sum up the 100 µl volumes of all samples that should get the secondary antibody, then calculate how much antibody stock needs to be added to reach the desired concentration. Spike these amounts of antibody in a tube with a volume of 5 µl 4% BSA-PBST per sample to stain, mix well, and add 5 µl of this mix to every tube that should be stained. In this instance, anti-rabbit IgG was used with STAR 460L (Abberior) and anti-rat IgG with STAR RED (Abberior) as fluorophores, each at a dilution factor of 1:300. This means that 3.3 µl of each secondary antibody was mixed with 1000 µl of 4% BSA-PBST. Afterwards, 150 µl of this mixture was added to each tube containing animal caps.

4-2) Incubate in the fridge overnight.

4-3) Wash three times with PBST; each time, wait at least 10 minutes with samples at room temperature.

4-4) For the post-fixation step, which is required for some antibody and mounting media combinations, apply 2% formaldehyde in PBST for 30 minutes at room temperature.

4-5) Wash three times in PBST.

Step 5: Preparation for mounting

5-1) Attempt to remove as much liquid as possible using P200, but even with P20, the animal caps may dry out during this step for a few minutes. This is not a big problem since they contain some liquid themselves; just do not let them dry out.

5-2) For mounting, each sample needs ~50 µl of mounting media, such glycerol or TDE. So, sum up all the volume for all samples. Then put this volume into a microcentrifuge tube.

5-3) If DNA staining is required, add to this volume the required volume of DNA stain (in experimental measurements, 5-TMR-Hoechst) to reach the final concentration (you might have to use the P10 or P2 to do this; do not pipet smaller volumes than 0.2 µl) and mix it well.

5-4) Apply ~50 µl to every tube with embryo samples.

Step 6: Mounting of animal caps for microscopy

Attention: To pick up the animal caps, you may need to cut off the front of the pipette tip with scissors; otherwise, it might be too small. Also, using glass pipettes for this transfer step has worked very well.

6-1) Put two long strips of double-sided adhesive tape on a microscope slide to make a channel.

6-2) Remove the brown paper cover, the stripes must be bare.

6-3) Take up the mounting medium with a glass pipette, taking care that all animal caps are picked up.

6-4) Carefully spot this liquid with animal caps onto the microscope slide, into the center of the tape channel.

6-5) Clean (isopropanol) a square #1.5 selected glass coverslip.

6-6) Carefully place the coverslip on top of the liquid in between the adhesive strips to avoid the formation of bubbles.

6-7) After the medium has settled, press down the cover slip on the tape strips and remove the extra medium with proper tissue.

6-8) Seal with clear nail polish at the open ends between the tape and let dry for 10 minutes or longer at room temperature.

Hint: Store samples at 4 °C; typically, they do not show any noticeable degradation over several months.

C. List of Publications

C.1. Sedeh, A. B., Kobitski, A., Dai, S., Eroğlu-Kayıkçı, S., Nienhaus, K., Hilbert, L., & Nienhaus, G. U. (2023). Stimulated emission double depletion nanoscopy with background correction at the single-pixel level. Optics Letters, 48(21), 5791-5794.

"This paper was highlighted as an Editor's Pick, which serves to highlight articles with excellent scientific quality and are representative of the work taking place in a specific field."

C.2. Barati Sedeh, A., Kobitski, A., Nienhaus, K., et al. 3-color 3D-STEDD microscopy reveals the nano-architecture of transcriptional clusters in embryonic cells.

"This paper is currently in the submission process."

C.3. Dai, S., Kobitski, A., **Barati Sedeh, A.**, Eroğlu-Kayıkçı, S., Hilbert, L., & Nienhaus, G. U. (2024). Photon-Efficient Aberration Correction for 3D-STED Imaging of Thick Biological Specimens Using Sensorless Adaptive Optics. ACS Photonics, 11(1), 310-320.

D. Summary of Individual Contributions to Thesis Work

Chapter 4: Pixel-Level Background Correction in STEDD Nanoscopy Using Local Weight Factor Calculations

- *Sample preparation and staining*: Performed by me, with initial training and guidance from Süheyla Eroğlu-Kayıkçı (co-author of the paper).
- *Data acquisition*: Carried out entirely by me.
- *Identification of limitations in the global STEDD approach and conceptualization of a local background correction strategy*: Independently conducted by me.
- *Development and implementation of the local STEDD algorithm in MATLAB*: Done independently by me.
- *Validation and testing of details presented in the new approach*: Designed and executed by me.
- *Manuscript preparation*: I wrote the initial draft of the manuscript.

Chapter 5: Multi-Color 3D STEDD Nanoscopy of Transcriptional Cluster Architectures and Inhibitor-Induced Chromatin Access Modulation in Zebrafish Embryonic Cells

- *Sample staining and mounting*: Performed independently by me.
- *Data acquisition*: Conducted by me.
- *Development of image correction pipeline in MATLAB*: Designed and implemented by me, with technical feedback from Dr. Andrei Kobitski.
- *Cluster segmentation and classification in MATLAB*: Developed by me, with technical feedback from Dr. Andrei Kobitski.
- *Quantitative analysis: Done by me.*
- *Manuscript preparation*: I have been writing the first draft.
- Prof. Dr. G. Ulrich Nienhaus and Prof. Dr. Lennart Hilbert supervised the project, contributing to the conception, discussion, and interpretation of the results.

Chapter 6: Sensorless Photon-Efficient Aberration Correction in 3D-STEDD Microscopy

This chapter is based on collaborative work published with Dr. Siqing Dai, who initially demonstrated the feasibility of the sensorless adaptive optics approach. My main contributions to this paper included:

- *Microscopy training and technical support for Dr. Siqing Dai*: I provided instruction and assistance, as she joined the lab after me.
- *Enhancement of the optical setup*: we (*Dr. Dai and I*) modified the system together to rebuilt the depletion beams paths in order to integrate spatial light modulators necessary for the adaptive optics procedure.
- *Sample staining and mounting*: Performed by me.
- *Daily discussions*: I was actively involved in daily discussions over results.

For the results presented in this chapter of my thesis, I was solely responsible for:

- *Sample staining and mounting*
- *Data acquisition*
- *Quantitative data analysis*

Collaborative Input

Throughout the development of all scientific papers, we routinely discussed ongoing work during weekly lab meetings. In these sessions, general suggestions and critical feedback were offered by Prof. G.U. Nienhaus and Dr. Andrei Kobitski, particularly in cases where data analysis procedures, or technical implementations could be optimized. These discussions were part of the collaborative environment in the lab and contributed to the refinement of the work.

E. Acknowledgements

I consider the opportunity to develop professionally and personally during the course of completing my doctorate thesis to be a tremendous privilege. The support, guidance, and encouragement many people have given me along my path makes me extremely grateful. Their contributions have been long-lasting for me and, hence, for my work.

Prof. Dr. Gerd Ulrich Nienhaus. Let me begin with a special thanks to you, dear Prof. Dr. Nienhaus. This dissertation stands on the basis of your guidance and expertise. The facilities, support, and spirit of collaboration you so openly have given to our research group were fundamental to the success of the work underlying this thesis. I am very grateful for the relentless enthusiasm that you continued to express about my research efforts, for valued advice, and for the open and approachable atmosphere. As I value all you have done to get me to this point, your mentoring sticks out in my mind as priceless.

Prof. Dr. Lennart Hilbert. Firstly, I would like to thank you for all the scientific discussions, guidance, and support, especially on the biology aspect of this work. I also appreciate you providing the lab equipment I required to prepare the biological specimens. Lastly, thank you for taking on the role of second reviewer for this thesis.

Dr. Andrei Yu Kobitski. I want to express my sincere gratitude for our frequent discussions about the analysis and interpretation of data. Many thanks for your help with technical problems and for supporting us with great microscope control software. I also appreciate your comments throughout the proofreading of my thesis.

Dr. Manuel Hüpfel. I would like to thank you, dear Manuel, for your constant willingness to support me by responding to my questions and the friendly conversation we have had. Your encouragement has always motivated me. Additionally, I would like to extend my appreciation for the careful proofreading of my thesis.

AG Nienhaus and APH. I would like to extend my special thanks to all our group members, especially Dr. Karin Nienhaus, Dr. Siqing Dai, soon-to-be Dr. Jasmijn Rath, and Dr. Hamed Qazvini, who have been constantly supportive and collaborative. Working with this committed and friendly team made even the most challenging tasks enjoyable. I value very much the sharing of ideas, teamwork, and mutual encouragement we shared. Indeed, your contribution meant much to the quality of our work and the good, motivating atmosphere throughout the process.

Karlsruhe School of Optics & Photonics (KSOP). My heartfelt thanks also go to the KSOP for their outstanding scientific and technical modules, which greatly contributed to my development as a professional researcher, and to my supportive mentor, Dr. Franco Weth, for his invaluable guidance throughout the ups and downs of my PhD journey.

Hamidreza Barati and Shekoufeh Motamedi. I am infinitely grateful to you, my wonderful parents. All I can say is that it was your efforts and support that brought me to this point. Your indescribable sacrifices, guidance, and trust in me have opened and smoothed this road. I shall always value your efforts for me. I appreciate you consistently being there at every stage.

تا آخرین لحظه عمرم مدیون تمام زحمات شما خواهم بود.

Alireza Barati. An immense thanks to you, my brother, for always having my back and being a constant source of support. Your lovely presence and encouragement have made this migration to pursue my academic dreams possible. I have always tried to follow in your footsteps during school time, which was the foundation of where I am today.

مرسی که با تلاش و حضورت، راه را به من نشان دادی تا وارد این م□یر شوم.

Mahta Moazzenzadeh. My sincere thanks to you, my wonderful love; grateful is not the word that comes close to describing how much I appreciate your constant support, and belief in me when I doubted myself. It is amazing to be so lucky to have an incredible companion like you.

خیلی ازت ممنونم، عشق من، برای انگیزه و امیدی که تو هر لحظه به من میبخشی.